



UNIVERSITY OF MESSINA
DEPARTMENT OF MATHEMATICAL AND COMPUTER SCIENCES,
PHYSICAL SCIENCES AND EARTH SCIENCES

DOCTORAL PROGRAMME IN PHYSICS (CYCLE XXXII)

Branched Polyethyleneimine/TEMPO-Oxidized Cellulose Nanofibers Xerogels for
Water Remediation: A Structural and Dynamical Study by Small Angle Neutron
Scattering (SANS) and Fourier-Transform Infrared Spectroscopy (FTIR)

Doctoral Dissertation of:

Giuseppe Paladini

S.S.D. FIS/01 - FIS/07

SUPERVISOR:

Prof. **Valentina Venuti**

CO-SUPERVISOR:

Prof. **Vincenza Crupi**

COORDINATOR:

Prof. **Lorenzo Torrisi**

Academic Year 2018/2019

Contents

Abstract	1
Introduction	3
1 Water decontamination solutions: an overview	7
1.1 The chemical-physical solution for water decontamination	9
1.1.1 Chemical precipitation	9
1.1.2 Ion exchange	9
1.1.3 Liquid-liquid extraction	12
1.1.4 Electrodialysis	13
1.1.5 Solid-phase extraction	13
1.2 The bio-solution for water decontamination	15
1.2.1 Phytoremediation	15
1.2.2 Bioremediation	15
1.3 Nanomaterials for water decontamination	17
1.3.1 Carbon nanotubes	18
1.3.2 Nanocrystalline zeolites	19
1.3.3 Dendrimers and nanomembranes	20
2 BPEI/TEMPO-oxidized cellulose nanofibers sponges	24
2.1 Cellulose	24
2.2 Water-cellulose interaction	27
2.3 Nanocellulose	28
2.4 BPEI/TOUS-CNFs sponges synthesis	30

3	Experimental	33
3.1	Neutron scattering	33
3.1.1	Introduction	33
3.1.2	Fission sources	33
3.1.3	Spallation sources	36
3.2	Small Angle Neutron Scattering (SANS)	36
3.2.1	Porod approximation	47
3.2.2	Guinier approximation	47
3.3	SANS diffractometer "Yellow Submarine"	49
3.4	SANS experiment	52
3.5	Fourier-Transform Infrared (FTIR) spectroscopy	54
3.5.1	Theoretical background	56
3.5.2	Harmonic oscillator model	62
3.5.3	Vibrational normal modes	63
3.5.4	IR absorption band features	64
3.6	BOMEM DA8 spectrometer	69
3.7	FTIR experiment	75
4	SANS analysis on bPEI/TOUS-CNFs sponges	77
5	Vibrational dynamics in bPEI/TOUS-CNFs sponges	92
	Conclusions	102
	Bibliography	104

Abstract

In the present thesis, cellulose sponges prepared using 2,2,6,6-tetramethyl-1-piperidin-1-yl (TEMPO) oxidized and ultra-sonicated cellulose nanofibers (TOUS-CNFs) as three-dimensional scaffolds, and branched polyethyleneimine (bPEI) as cross-linking agent, underwent to a systematic Small Angle Neutron Scattering (SANS) and Fourier-Transform Infrared Spectroscopy (FTIR) investigation, by varying the amount of cross-linker, water content and temperature. The aim was to provide an experimental evidence of nano-porosity in the TOUS-CNFs network of these nanosponges (CNS) by investigating the water nano-confinement geometries in the adsorbent material. Moreover, we also verified how the breaking/reformation of specific intermolecular hydrogen bond interactions between water and the chemical groups present in the architecture of the CNS can contribute to regulate the water adsorption process observed at macroscopic level.

Concerning SANS measurements, the analysis of the experimental data, performed in terms of a Correlation Length Model (CLM), allowed us to extract the short-range correlation length ξ , interpreted as a very first indirect estimation of the effective nano-dimension of the cavities produced by the cross-linking of the reticulated cellulose nanofibers. From the model, a power-law (n) and Lorentzian (m) exponents have been also obtained, respectively associated to the density of TOUS-CNFs at high (larger than hundreds of Å) and low ($\sim 10 - 100$ Å) spatial scale. These parameters turned out to be all sensitive to the structural variations induced by the progressive uptake of water on the bPEI/TOUS-CNFs sponges with different ratios. Finally, the effect of the addition of citric acid in the CNS formulation was investigated, confirming its role in increasing cross-linking density and sponge rigidity.

In addition, a preliminary investigation of the molecular connectivity and the extent of hydrogen-bond patterns of water molecules confined in the bPEI/TOUS-

CNFs sponges was also performed by FTIR spectroscopy. The proposed spectroscopic method exploits the combined analysis of the vibrational spectra of polymers hydrated with water and deuterated water, which allows us to separate and selectively investigate the temperature-evolution of the HOH bending mode of engaged water molecules. As main results, we find a strong experimental evidence of a liquid-like behaviour of water molecules confined in the sponge nano-cavities and we observe a characteristic destructuring effect on the hydrogen-bonds network of confined water induced by thermal motion.

The obtained results appear crucial in order to rationalize the design of these sponges and to track the changes in the ability of the final products as efficient nano-confinement systems for water decontamination.

Introduction

Water decontamination issues represent a real risk to human health as well as to all other forms of life on the planet. Whether from the ocean, lake or river, water has always been fundamental to the human beings and it is an essential requirement for its survival. The increase in the concentration of pollutants has reduced, over time, the quality of water with a consequent impact on different aspects such as health and environment. Innovation in water purification, in order to supply clean water for drinking, food preparation, processing and sanitation, represents a worldwide crucial concern caused by the increase in population, industrial activity and widespread urbanization. In this context, different physical-chemical methods have been taken into account in order to reduce the amount of pollutants (dyes, heavy metals, pharmaceutical agents, pesticides) from water and to prevent further contamination. Catalytic processes [1], electrochemical reactions [2–5], membrane processes [6, 7], and photodegradation [8] are some of the approaches which can be used in order to monitor and reduce the amount of contaminants in water, even though the performance of water-cleaner systems based on adsorption processes still remains the most efficient solution [7, 9–13]. Among the proposed solutions, activated carbon (AC) is one of the most used materials for water decontamination, although it has high production and regeneration costs. However, the increase in restrictions associated with the maximum limits of contaminant concentrations requires, to date, the development of technologically advanced materials with high absorption efficiencies while remaining of low economic and environmental impact. Based on these considerations, the use of cellulose as the main component represents a good starting point for the design of the latest generation materials for water treatment. In this context, it is clear that research aimed at engineering systems that are increasingly efficient in eliminating harmful agents from water represents, nowadays, an emerging field of great interest both in terms of technology and application.

Recently, cellulose nanofibers with high absorption efficiency in the removal of organic and inorganic wastes are gaining a considerable interest by the international scientific community [14–20]. Specifically, the oxidation of hydroxyl cellulose groups represents an efficient approach to the formation of nano-structured cellulose with highly reactive functional groups including aldehyde groups and carboxylic acid parts. In the latter case, the most commonly used approach is based on the NaClO oxidation process mediated by the 2,2,6,6-tetramethyl-1-piperidinyloxy (TEMPO) radical; using NaBr as a co-catalyst.

However, the direct use of TEMPO-oxidized cellulose nanofibers (TOCNFs) is limited by the fact that they are easily dispersible in water, which is why the corresponding hydrogels and aerogels lack of sufficient mechanical stability when immersed in aqueous solvents. To overcome this problem, substrates with amino groups, including branched polyethyleneimine (bPEI), which acts as a cross-linking agent for this type of system, are used. This procedure leads to the formation of systems with a "sponge" structure having high mechanical stability, good affinity with aqueous solvents and high absorption efficiency [21–23].

Branched polyethyleneimine/TEMPO-oxidized and ultra-sonicated cellulose nanofibers (bPEI/TOUS-CNFs) systems are proved to exhibit a sponge-like porous structure with a two-dimensional sheet morphology. Cellulose nanosponges (CNSs) resulted to be valuable adsorbent solutions for water remediation from both organic (including emerging contaminants) and inorganic (Cd^{2+} , Zn^{2+} , Pb^{2+} , Cr^{2+} , Cu^{2+}) pollutants, with an absorption efficiency higher than 200 mg/g [21].

Moreover, the cross-linking of nanofibers allows to move from nano-sized particles to nano-structured, macro-dimensioned sorbent systems, preventing all the eco-safety issues related to the use of nanotechnology for environmental remediation [22]. Micro-porosity of CNSs has been well documented by Scanning Electron Microscopy (SEM), and has been associated to the freeze-drying process followed for their preparation. On the contrary, nano-porosity has been only hypothesized, according to the enhanced adsorption performances of the material, without furnishing any experimental evidence. Thus, while the covalent cross-linking between the carboxylic groups of CNFs and the primary amino units of bPEI, with consequent formation of amide groups, has been disclosed by ^{13}C CP-MAS solid-state Nuclear Magnetic Resonance (NMR) spectroscopy and Fourier-Transform Infrared (FTIR)

investigation, it appears now of fundamental importance giving an experimental evidence of the nano-porosity and clarifying its role in regulating the mechanism of water adsorption observed at macroscopic scale.

On the basis of these considerations, the present thesis is aimed at the study of nanocellulose-based systems with particular interest in understanding how the presence of nano-confinement geometries (i.e. nano-pores formed by cellulose fibers) regulates the mechanism of water absorption observed at the macroscopic level and at clarifying the link between the mechanisms of formation/breakage of hydrogen bonds within the bPEI/TOUS-CNFs system and the absorption efficiency. These information could be used to define a high-efficiency synthesis protocol for the optimization of this system in the field of water decontamination.

Structural features related to the size and arrangement of nano- and micropores within the bPEI/TOUS-CNFs polymeric network, which are directly responsible for the efficiency associated with the water absorption mechanism, were revealed through Small Angle Neutron Scattering (SANS) measurements varying the hydration levels and bPEI content [24–27].

Furthermore, Fourier-Transform Infrared Spectroscopy (FTIR) in Attenuated Total Reflectance (ATR) geometry, allowed us to get insight the water molecules confinement mechanism inside the polymeric bubbles formed during the hydration process. FTIR-ATR experimental data revealed a clear dependence of the hydrogen-bonded network involving the OH groups of the polymers on the temperature and on the molar ratio between the cross-linking agent (bPEI) and cellulose nanofibers.

In the first chapter of this thesis, the general issues related to the proposed topic will be addressed, with particular attention to the role that water plays in different framework and how important it is in a global context. In addition, a brief description of the state-of-the-art about technologies used to remove organic and inorganic components potentially harmful to aqueous systems will be provided.

In the second chapter, the bPEI/TOUS-CNFs sponges will be presented in detail with particular emphasis on the synthesis procedures and the chemical-physical characteristics. The adsorption properties will also be outlined as a function of the dimensions of nano-pores and the amount of crosslinker with the purpose of emphasizing the advantage that these types of systems provide in the field of waters remediation.

In the third chapter a description of the experimental techniques used will be provided, together with the instrumental specifications and parameters adopted during the measurements.

The last two chapters of this thesis will be entirely devoted to the obtained experimental results and their interpretation. Specifically, in chapter 4, the SANS measurements will be discussed in detail revealing structural changes as the amount of bPEI and water content increase. Formation of polymeric "bubbles" and the onset of a macroscopic phase transition for high h values are some significant results obtained through this technique.

In the fifth chapter, the temperature-evolution of the vibrational spectra of bPEI/TOUS-CNFs sponges hydrated, in a combined way, with water and deuterated water will be discussed. In particular, the behaviour of the HOH bending mode of water molecules engaged in the polymeric system will be analyzed, in order to probe their molecular connectivity and dynamics. Interestingly, the spectroscopic data give evidence of the presence in the nano-cavities of the sponges of water molecules that appear in liquid state even below the temperature of 270 K where usually the bulk water tends to crystallize.

Finally, the last part of this thesis is devoted to conclusions, with a summary of the main results and recommendations for future work in this field of research.

Chapter 1

Water decontamination solutions: an overview

As is well known, although the planet is mostly made up of water, only the 2 % of it can be used as an active source, being the remaining 98 % at high content of saline of oceanic provenance [28]. Furthermore, of the 2 % mentioned above, only the 0.036 % is available while the remaining 1.964 % is made up of water in the form of ice caps and not accessible groundwater from aquifers. Nowadays, one of the main issue related to water quality concerns the contamination of sources by pathogenic microorganisms and anthropogenic harmful agents of various origins. The latter includes all types of chemicals, pesticides, dyes and heavy metals as well as all domestic, agricultural and industrial waste materials (Fig. 1.1).

In addition, even in small concentrations, the presence of both synthetic and natural pollutants can lead to devastating harmful effects when present in form of mixtures. It is worth of note that also pathogenic micro-organisms [29] can lead to pollution of natural water sources, which is why in recent years there has been a growing interest towards the development of new technologies for water treatment. Another problem is the presence of water polluted by radioactive sources. The decontamination of radioactive water is also a real issue for human health and the environment. In this regards, a research group recently engineered a new method for the decontamination of radioactive waters using graphene-based materials [30]. In particular, graphene oxide in aqueous solvent leads the radionuclides (cause of pollution) to aggregate forming "lumps".

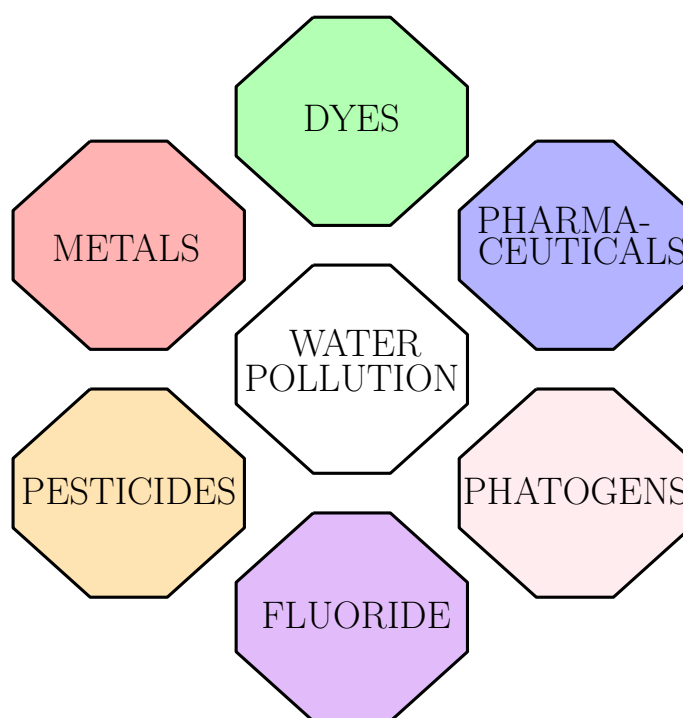


Figure 1.1: Overview of the main natural and anthropogenic pollution factors.

The high efficiency of absorption is due to the large external surface of the graphene "flakes", capable of absorbing high quantity of toxins and heavy elements. The research in this field is focused, nowadays, in identifying the most advantageous material capable to selectively absorb a specific type of pollutant dispersed in solution. This involves not only a concrete challenge from a technological point of view, but also economical to political issues. For this reason, the development of efficient systems capable of reducing the content of toxic agents through the activation of "molecular absorption" processes is a fundamental aspect, especially in those countries where the rapid industrial growth is not adequately supported by an associated environmental adjustment program [31–33]. Over the years, several approaches based on different processes such as electrochemical precipitation, membrane separation and photodegradation have been considered for the engineering of efficient systems capable of selectively encapsulating external pollutants. At present, activated carbon (AC) represents the most used for water decontamination, although it has high production and regeneration costs. However, the increase in restrictions associated with the maximum limits of contaminant concentrations requires the development of technologically advanced materials with high absorption

efficiencies while remaining of low economic and environmental impact.

Any decontamination mechanism, defined as that process capable of eliminate, partially or completely, both natural and synthetic pollutants, can be included in two large macro-categories know as chemical-physical processes and biological processes.

1.1 The chemical-physical solution for water decontamination

In the following, a series of chemical-physical mechanisms that allow, using different principles, to remove both organic and inorganic pollutants from water, are reported.

1.1.1 Chemical precipitation

Chemical precipitation is a simple and commonly accepted approach used for removal of metal ions from aqueous solutions. It involves the progressive reduction of the metal content until a concentration considered not dangerous is reached, through the formation of insoluble solid precipitates (hydroxides, carbonates or sulphates). Afterwards, the obtained precipitate is pulled out from the solution by filtration or centrifugation. This phenomenon is strictly dependent on the solubility constant of metals involved, their concentration and pH. Another process of adsorption is represented by the co-precipitation, in which the metallic component is co-precipitated through the use of secondary minerals. In fact, if added in solution, they are oxidized by the water by participating in the precipitation of the metal contents. Chemical precipitation has been widely used over the past years for water treatment (mainly of industrial provenance) although it has different side effects and high costs. Moreover, this mechanism is not "selective", and requires the use of corrosive chemicals for its operation, which is why it is no longer used [34, 35].

1.1.2 Ion exchange

Ion exchange represents a versatile and reversible separation process with high efficiency in the removal of unwanted impurities from wastewaters. It is based on the transfer of ionic species from a liquid phase to another, which are forced to pass

through a solid resin. The latter can be both synthetic or natural with high tendency to absorb metal elements on its surface (Fig. 1.2).

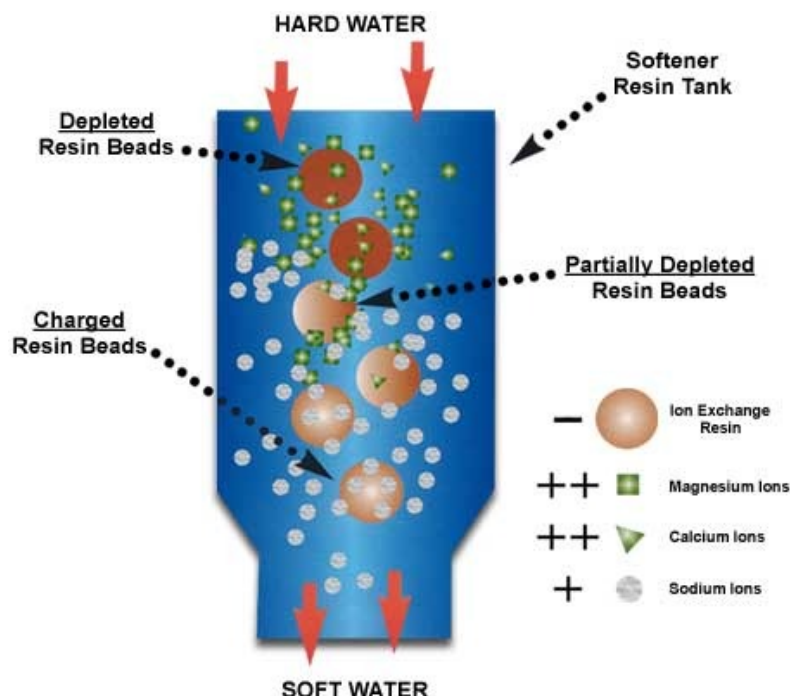


Figure 1.2: Representation of the ion exchange process for water purification.

In particular, synthetic ion exchange resins are typically made up of organic compounds polymerized in such a way to form a three-dimensional porous matrix, with structure and dimensions determined by the polymerization conditions. The most commonly used ion exchangers are resins containing groups of sulphonic acid ($-\text{SO}_3\text{H}$) or resins containing groups of carboxylic acid ($-\text{COOH}$), being both full of "exchangeable" hydrogen ions. Although the use of polymer-based synthetic resins is a cutting-edge method in the field of water remediation, this process shows several practical limitations due to the pre-treatment that wastewater needs to avoid contamination of the resin itself. In addition to this, the synthesis of ion-exchange resins requires the intensive use of chemical reagents whose employment is causes of 'secondary' pollution. To overcome this problem, natural zeolites are adopted (Fig. 1.3) with high efficiency in the removal of metallic cations. These systems are extremely advantageous compared to the previous ones thanks to their high abundance in nature and to the their relative low cost.

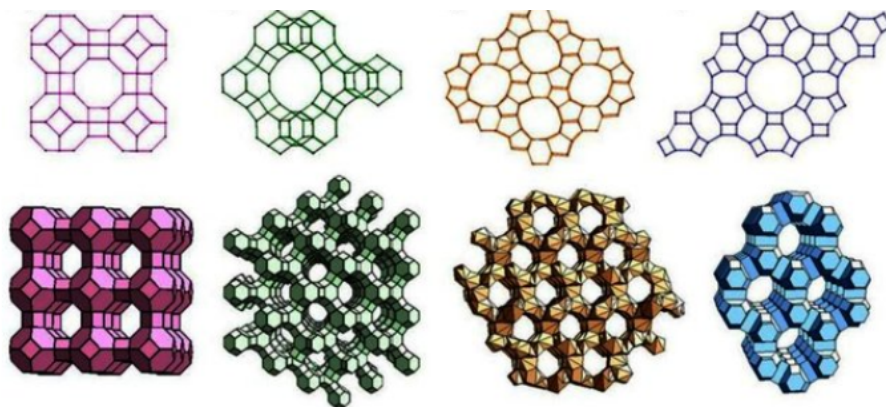


Figure 1.3: Typical 3D and 2D structures of zeolites.

Zeolites are minerals belonging to the group of hydrated aluminium silicates, having a three-dimensional network composed of SiO_4 and AlO_4 tetrahedra [36]. For their efficiency in terms of cation *exchangers* they have been widely used for decontamination of natural waters, as catalysts in oil refining processes and as acidic correctives for the soil.

The presence of a total negative charge in the network of such systems (due to the presence of Si^+ and Al^{3+} ions) is balanced by the exchangeable cation (sodium, potassium, etc.) or calcium). The presence of metal ions is confined within the micro-porosity of the three-dimensional structure [37] (Fig. 1.4). Natural zeolites have a higher thermal stability and a better mechanical resistance in acidic environments, compared to absorbent materials commercially available [38].

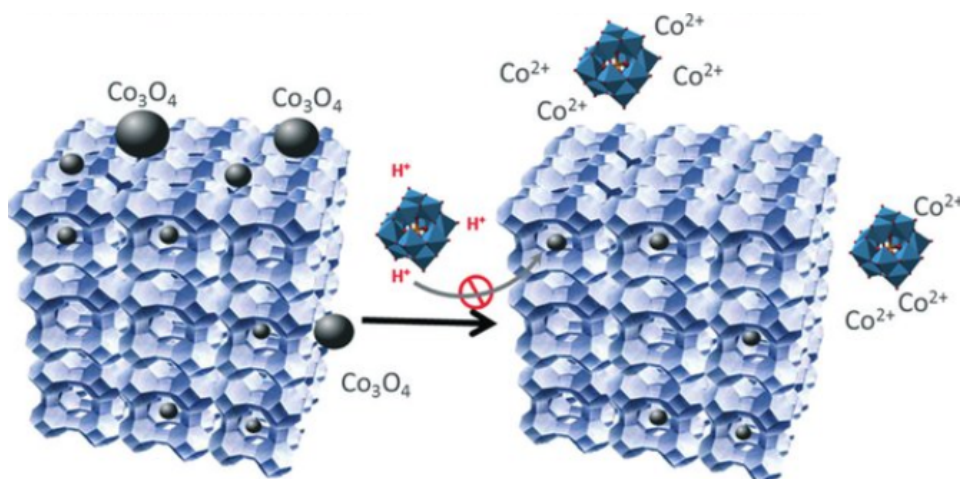


Figure 1.4: Representation of the synthesis of a metal-zeolite composite.

1.1.3 Liquid-liquid extraction

The liquid-liquid extraction is a widely accepted method for the removal of polluting metal ions, in which absorption takes place by putting in contact a aqueous medium with an organic phase containing a chelator [37]. Specifically, the removal of pollutants is carried out by placing the solution in contact with a solvent. The solute is generally soluble and produces two liquid phases which, once separated, will form the *extract* (phase containing pollutants) and the *refined* (water free of impurities), respectively (Fig. 1.5).

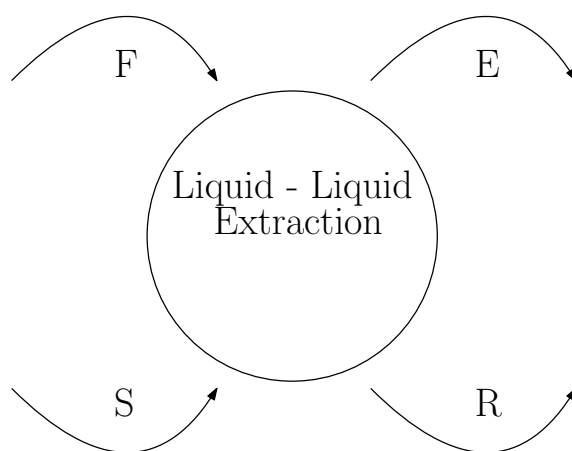


Figure 1.5: Schematic representation of the liquid-liquid extraction procedure. On the left there is the contaminated phase (F) and the extraction solvent (S). On the right (as outputs) we have the extract (E) and the refined (R), respectively.

A first drawback associated with the use of this technique concerns the organic phases used. Typically, highly flammable and volatile compounds (VOCs) are used making this approach a significant source of secondary pollution. Today, traditional organic solvents have been replaced by "green" alternatives including ionic liquids (ILs). ILs are systems generally made up of two components: an ion and a cation dispersed in solution. Generally, the cation is chosen with a low degree of symmetry so that it considerably reduces the energy of the associated crystalline lattice. Their unique characteristics, such as their low volatility, non-flammability and the ability to dissolve both organic and inorganic compounds, are important advantages over conventional synthetic organic solvents. Thanks to this range of properties, the study of ionic liquids is assisting to a remarkable development as alternative to traditional organic solvents in the separation of metals from water sources.

1.1.4 Electrodialysis

Electrodialysis is a process that allows the removal of ionic components by means of semi-permeable ionic-selective membranes. It involves the application of a potential difference between two electrodes, which produces a flow of cations and anions to the corresponding terminals (Fig. 1.6).

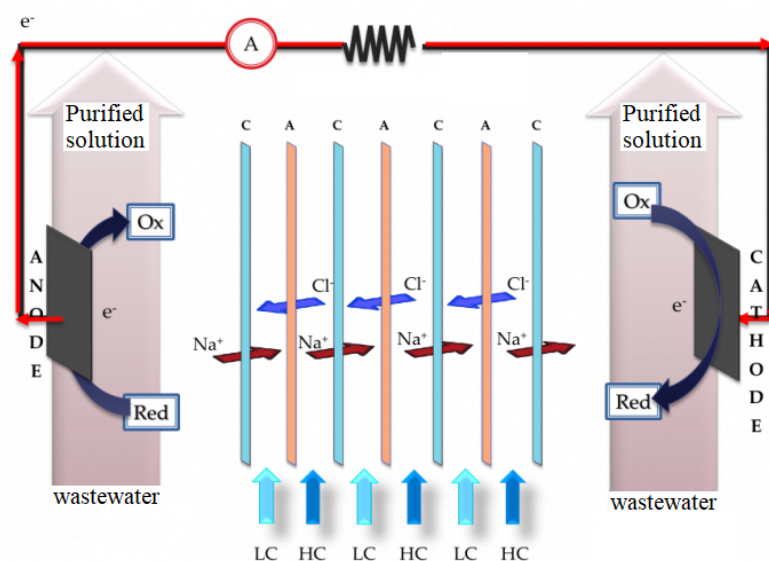


Figure 1.6: Schematic representation of the electrodialysis process used for water decontamination.

Advantages of this technique include the almost total absence of potentially dangerous waste products, the low voltage required for operation and the possibility to operate at constant temperature and pressure. However, it does not appear to be commercially competitive due to the high cost of the electrodes and the short time of life of membranes [39].

1.1.5 Solid-phase extraction

Solid phase extraction (SPE) represents one of the most used and adopted technique for the removal of solid analytes from water. It is used for extraction and purification of organic and inorganic pollutants in solution, with higher efficiency and recovery as compared to the liquid-liquid extraction previously discussed. This technique exploits the affinity difference between the analyte dissolved in liquid phase (pollutant, metal ion, etc.) with a specific solid phase (adsorbent). In addition, high

enrichment factors and elevated recoveries are feasible with SPE using short times. In many cases the process leads to high quality treated effluents and also offers flexibility in design and operation. The most common adsorbent used for metal and organic trace removal are, currently, silica-based materials [37]. The use of silica as a support material has valuable mechanical and "swelling" properties, as well as an advantageous low cost. In addition, these materials can be functionalized with organic groups resulting in the formation of silica gel. The latter exhibits better absorption capacity than the polymer-based organic resins mentioned above. This is typically due to the presence of organic functional groups in the matrix, which increase the binding capacity.

Another largely used system in the field of water treatment is the activated carbon (AC) [40]. The high porosity and the high surface area ensure an extremely advantageous solution for the removal of pollutants, both organic and inorganic, in wastewater. Fig. 1.7 shows a SEM image of the AC, which highlights the porous structure of the material.

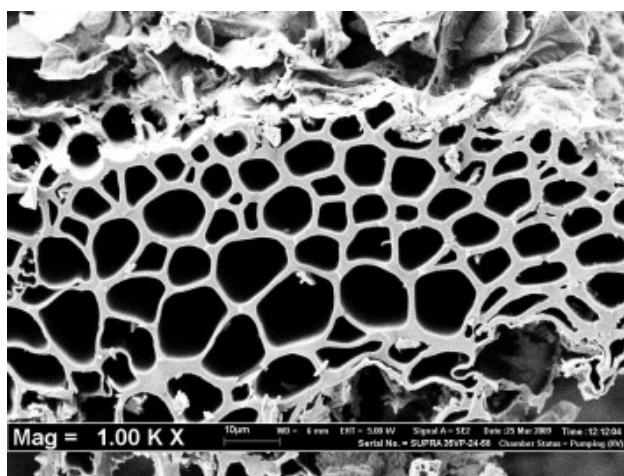


Figure 1.7: SEM image of activated carbon with a 1000x magnification factor.

Despite its many advantages, the high cost of activated carbon limits its diffusion and large-scale application. In order to reduce production costs, alternative sources of AC have been considered including waste materials. Currently, ACs are produced starting from agricultural waste products, which can be obtained with low economic impact [41]. Several studies [42, 43] have demonstrated how the absorption efficiency of AC strictly depends on several factors including particle-size distribution, exposure time and surface/volume ratio.

1.2 The bio-solution for water decontamination

1.2.1 Phytoremediation

Nature activates decontamination processes through plants to restore the ecological balance and clean up the environment. Their main role is to promote the formation of bacterial flora which is the main responsible of the decontamination processes. The phenomenon of absorption, accumulation and decontamination of metals (and/or anthropogenic chemicals) by plants is called *phytoremediation*. Phytoremediation is a class made up of a large variety of bio-mechanisms, including phytoextraction, phytostabilization, phytovolatilization and rezoiltration, which operate under different conditions, although their use represents, at present, an alternative solution in the field of decontamination of pollutants from water [44–48].

1.2.2 Bioremediation

Bioremediation is defined as the process of removing contaminants through the use of microorganisms (MO). Their use for environmental purposes is possible thanks to the advanced adaptability that these systems offer in any type of environment. As is well known, in fact, they can grow and develop to sub-zero or extreme temperatures, in the presence or absence of oxygen and under anaerobic conditions. Such micro-organisms may be used to degrade external contaminants including organic and inorganic compounds [49]. Although MO cannot completely eliminate metallic traces in aqueous solvents, they can interact with them, in both natural and synthetic environment, affecting their chemical properties. The mechanisms by which MO remove metallic agents from water are:

- Complexation
- Intracellular storage
- Extra cellular accumulation/precipitation

Fig. 1.8 shows the most significant interaction processes that take place in a MOs/metallic element system.

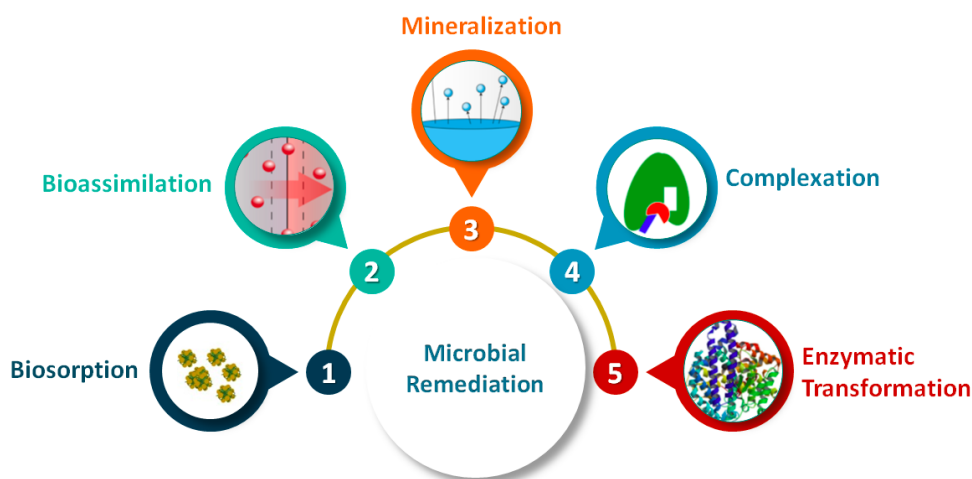


Figure 1.8: Scheme of the principal interaction processes between microorganism and metallic elements.

In most cases, biodepuration processes involve the occurrence of oxidation-reduction reactions in which either an acceptor electron (typically oxygen) is added to the metal stimulating oxidation, or a donor electron is acquired to reduce the oxidized pollutant. In both cases, natural constituents, such as vitamins and minerals, are included into the liquid environment, in order to promote and optimize the reaction conditions. Recent studies have shown that easily removable metals through biodepuration processes are Ag, Al, Au, Cd, Co, Cr, Cu, Fe, Hg, Mn, Mo, Ni, Pb, Pt, Se, U, V and Zn [50].

The most used microbial system in the field of water decontamination is the *bacterium*. Bacteria are the most versatile and proficient microorganism on earth. They represent about the totality of the biomass on earth, and posses excellent bio-absorption properties due to their small size and ability to grow in controlled environments [49]. The absorption mechanism takes place through a two-step process that involves a first interaction between the metal ion and the groups reagents of the bacterium, followed by inorganic deposition of metal excess. This process is called *chelation* (Fig. 1.9). Generally, the carboxylic groups of acids glutamines of peptidoglycans (main substance of the cell walls of bacteria) are used as deposition sites for metal ions.

A *chelate* is a molecular assembly in which organic molecules are entrapped by a chelating agent. Generally, the formation of such structure is possible thanks to the activation of *coordination bonds*.

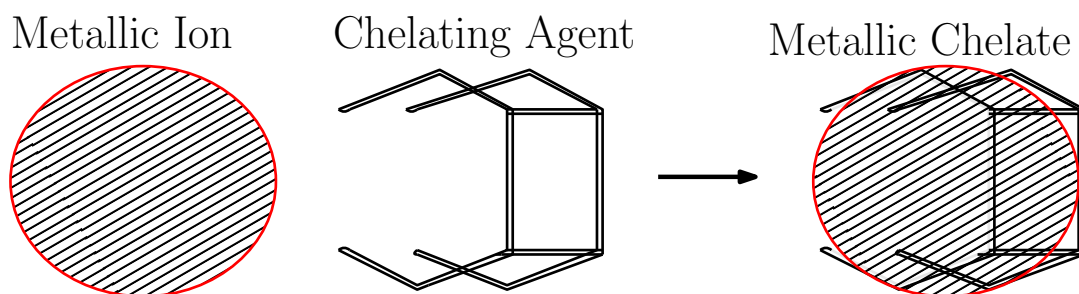


Figure 1.9: Chelation process.

The 3D structure of the resulting compound is a very stable complex where a central atom (i.e. metallic ion) is "grabbed" by a chelator, as it was caught between the claws of a crab (hence the term chelation).

Chelates are found to be extremely important in oxygen transport and in many biological catalysis processes as well as for entrapping metallic impurities from water mediums.

However, another highly absorbent system is represented by *algae*, a fundamental biological agent found in the seas and oceans. Recent studies [51–53] have shown that such systems are capable of encapsulating metallic agents in solution without producing, as secondary products, toxic substances. The basic principle of selective absorption, which leads to the total or partial removal of metal traces in solution, is similar to that adopted by bacteria. The cell walls of these systems consist of metal-receptor sites including proteins, polysaccharides and cellulose. Brinza et. al. [54] studied the absorption capacities of about 17 different microalgae and 39 macroalgae; reporting how they can be categorised according to the metallic element absorption characteristics.

1.3 Nanomaterials for water decontamination

In the field of water remediation, nanotechnology has played in recent years a fundamental role in the development of new "smart" materials with high absorption efficiency. If compared to most meso/macroscopic adsorbent materials, nanoparticles (NPs) show a number of advantages mainly related to their size and high surface-to-mass ratio. In addition, they exhibit remarkable structural and electronic properties that make them the top in the field of applied physics [55].

In the following sections, different types of nanoscopic systems as adsorbents for water decontamination will be briefly described, including carbon nanotubes, nanocrystalline zeolites, dendrimers and cellulose-based nanomaterials.

1.3.1 Carbon nanotubes

Carbon nanotubes (CNTs) are hollow cylinders made up of carbon atoms with diameter of the order of nanometres (Fig. 1.10). They are produced by using various thermal processes that extract "sheets" of hexagonal shape and then "wound" to form a cylinder.

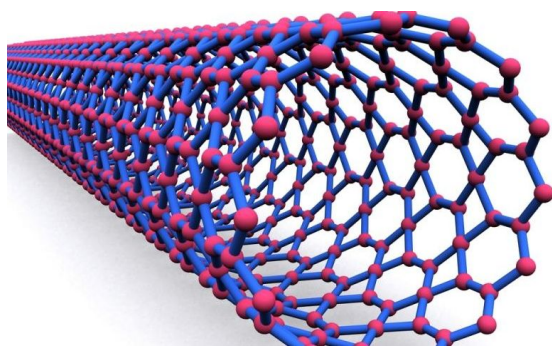


Figure 1.10: Representation of a single-walled carbon nanotube (SWCNT).

Carbon nanotubes are 300 times mechanically more stable and 6 times lighter than steel. They have a very large surface area that allows the system to be an excellent thermal conductor as well as capable to sustain high voltages.

In water treatment, carbon nanotubes are used for adsorbing a wide range of organic compounds dissolved in solution. This is mainly due to the high affinity that metallic elements show with respect to CNTs, allowing the removal of contaminants from the water through the use of synthetic filters consisting of nanotubes. More specifically, they allow the passage of water molecules within the cylindrical nano-cavities preventing the passage of chemical contaminants and microbials. This process is favoured by the application of an external pressure on the system so as to "force" the passage of water through the inner carbon-based cavities. As a result, high selectivity can be achieved if compared to the current membrane technologies [56]. Recent experimental results have shown that CNTs have the ability to absorb specific chemicals including dioxin [57], fluorides [57], lead [58] and alcohols [56]. The adsorption of dioxin, a carcinogenic material obtained as a waste product from

industrial processes, provides an excellent example of how CNTs can be used in the field of water decontamination. Specifically, it has been demonstrated that the absorption efficiency of such systems is actually accounted by the number of layers that made up the nanotube itself. According to this, we can distinguish between single-layer carbon nanotubes (SWCNTs) and multi-layer carbon nanotubes (Fig. 1.11).

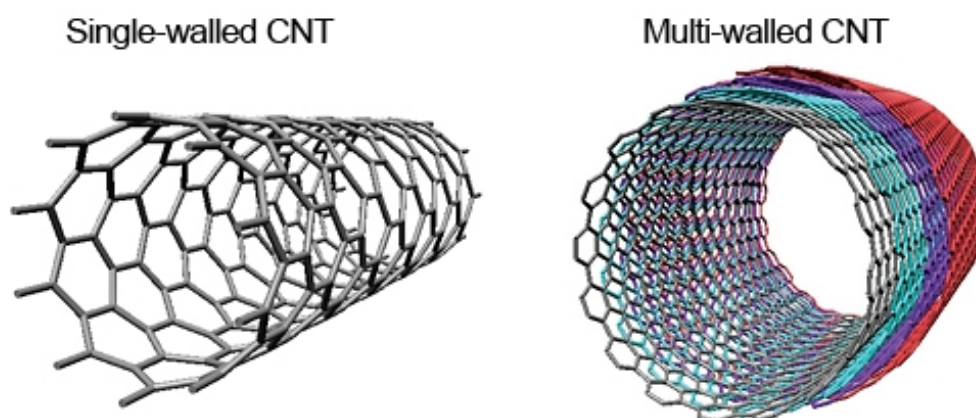


Figure 1.11: Single-walled carbon nanotube (SWCNTs, left); multi-walled carbon nanotube (MWCNTs, right).

C. Park et. al. [58] demonstrated that the absorption capacity of carbon nanofibers in removing metals from water is greater than that obtained through the use of the AC. In addition, MWCNTs show high dichlorobenzene removal efficiency over a wide pH range and work as molecular sponges against the CCl_4 . These experimental results, finally, show how CNTs can be used as high-efficiency "green" selective absorption materials for the removal of pollutants from water.

1.3.2 Nanocrystalline zeolites

Nanocrystalline zeolites (NZ) are materials characterized by tetrahedral arrangements mostly made up of silicon, aluminium and oxygen atoms. The basic unit of the zeolitic framework consists of Si^{4+} and Al^{3+} ions bonded to 4 atoms of oxygen. Tetrahedra are bonded together through the sharing of an oxygen atom to form polymeric chains. The formation of a three-dimensional structure is possible because each tetrahedron are shared with other surrounding tetrahedra such that

to form a fully-connected network. The three-dimensional structure of NZs provides the formation of channels and cavities, which allow the introduction of a given amount of molecules inside depending on their size and charge. Over the last 10 years, the study of such systems has grown exponentially thanks to their peculiar properties as molecular "sieves", high capacity for cation exchange and their high affinity against metal ions. Nowadays, zeolites with dimensions of 1 - 10 nm can be produced with relatively simple processes.

The outer surface area and the small diffusion length make NZs a technologically advanced product compared to traditional zeolites with a microscopic dimension. In fact, as it is well reported in literature, NaY nanocrystalline zeolites are capable of absorbing toluene (organic solvent) with an efficiency exceeding by 10 % the value obtained by commercial NaYs. Likewise, ZSM-5 zeolites with particle sizes of about 15 nm, absorb more than 50 % of toluene compared to microscopic ZSM-5 [31]. These materials can be chemically-functionalized in order to increase their adsorption performances which, together with their relative low cost and high abundance, makes these systems an advantageous and alternative solution for water treatment.

1.3.3 Dendrimers and nanomembranes

Dendrimers are polymeric macromolecules with a hyper-branched structure extended from a central nucleus to a terminal section that defines its dimensions (Fig. 1.12). The structure of a dendrimer can be classified into three topologically different regions. From the central part, called *core*, dendrons (monomeric units) branch out in the three spatial orientations until they reach the so-called "periphery", consisting of the end sections of dendrons themselves. The non-linear expansion of this systems is achieved by polymerization of a branched monomer, which is responsible of irregularities and defects. As a result, dendrimers are particularly appealing both in terms of basic research and for their applications in several fields of applied nanotechnology. In particular, their applications range from medicine to drug delivery, from sensor technology to decontamination of the water sources.

Similarly to linear polymers, they show a very large number of monomers linked together to form spherical, conical or discoidal structures of 2 - 20 nm in size [59]. A recent study has shown how poly-(starchamine) dendrimers exhibit high metal ion removal capabilities from aqueous solutions especially towards copper(II) [60].

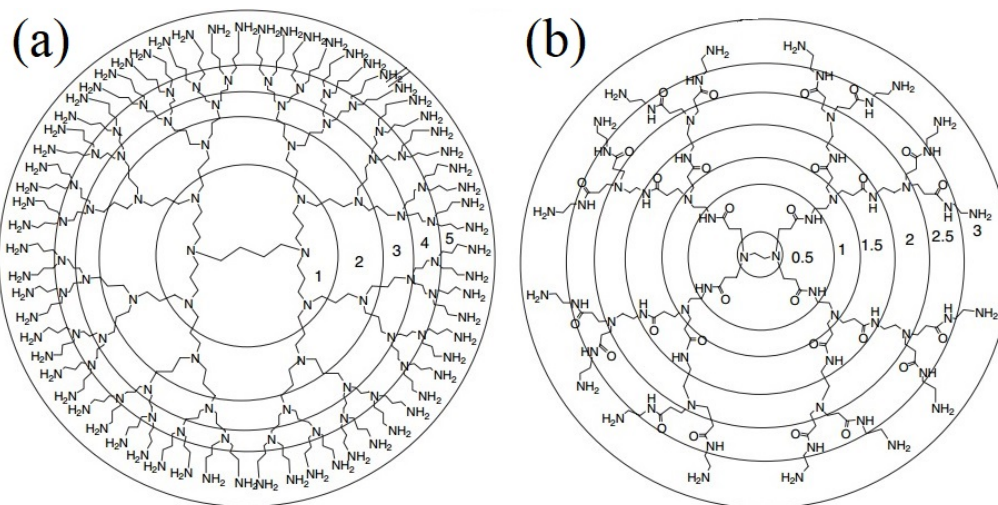


Figure 1.12: Representation of two dendrimers: (a) Poly(Propylene Imine) (PPI) and (b) Poly(Amido-Amine) (PAMAM) dendrimers with generation of shell depiction, as example.

Specifically, the high concentration of nitrogen ligands makes these systems useful as chelating agents against copper ions in solution. The removal is achieved by means of a two-step process. First, uptake of dendrimers into the wastewater is carried out. The latter, once bounded with the metal ions present in solution through chelation reactions, is driven through an ultrafiltration membrane that prevents the passage of the polymer/ion complex dendrimer - metal. Then, metal ions are detached from the dendrimer, which can be further reused. In addition, dendrimers containing bactericidal vectors can be also used for the removal of bacteria from water sources, through the activation of reversible processes.

Nano-reactive materials have been used in recent years for the engineering of synthetic membranes for water treatment. In particular, water-filtration membranes are gaining considerable interest for their versatility, cost and durability. The absorption of these systems is extremely selective thanks to the possibility of varying the size of the pores and the permeability. In contrast to sedimentation, flocculation and activated carbon processes, which remove a limited portion of pollutants, nanomembranes (NMs) operate over a wider range of dangerous chemical classes, producing pure water of the highest quality (Fig. 1.13).

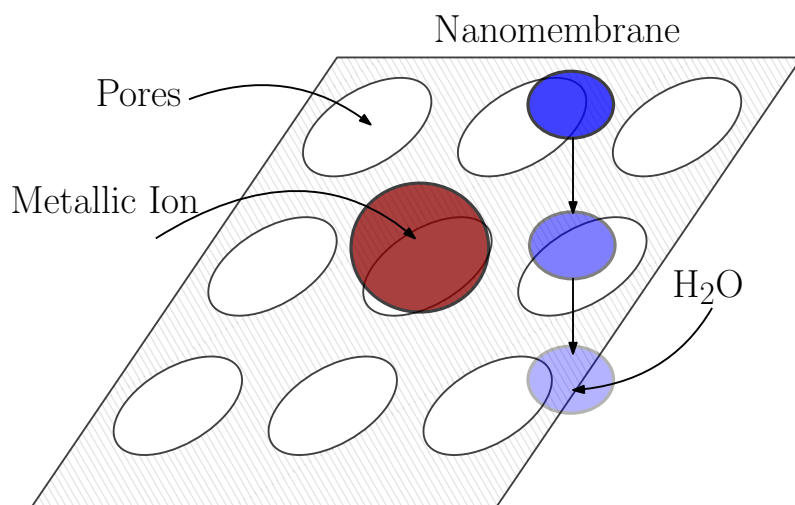


Figure 1.13: Nanomembrane operating as molecular "sieve" against metallic ions. The red particle, due to its shape and chemical properties is prevented to pass through the membrane nano-cavities. On the contrary, thanks to their dimensions, water molecules are allowed to pass through. As a result, if placed in contaminated wastewaters, NMs provide pure water for water treatment applications.

This structure has been demonstrated to be able to decompose pollutants such as 4-nitrophenol and to extends linkages with metallic ions in aqueous solution [61]. In addition to this, polysulphonate membranes coated with silver particles show interesting anti-bacterial properties and hence a remarkable solution in the removal of viruses from aqueous solutions [62]. They also exhibit significant resistance to the organic contamination, typically caused by the presence of bacteria on the surface of the membrane itself. This because Ag^+ prevents the aggregation process, keeping the material in working conditions with very long life times.

In conclusion, the role of nanotechnology in the development of water treatment systems has grown significantly, especially in recent years, due to technological and applicative interests. In this respect, therefore, the synthesization of nano-structures, nanocomposites and nanomembranes for environmental applications (and, in particular, associated with the purification of water sources) will undergo to massive development associated with the ever-increasing collective need for cleaning drinking water. The decontamination technologies described here provided a brief overview of the modern procedures currently used for this purpose, which operate on the basis of different chemical-physical processes.

The major contribution to removal efficiency has always to be attributed to the size of the effective surface area of the active material used. For this reason, nanoparticles are the most effective system in this context, and are therefore preferred over conventional alternatives. Future objectives in this field mainly concern the development of systems that allow the complete removal of all types of large-scale pollutants. Currently, researches are focused on the development of "environmental friendly" systems based on *cellulose nanofibers*, which have high removal efficiencies of organic compounds and metal ions due to their unique properties. In the next chapter, the characteristics of these systems will be described in detail together with their use in the field of water decontamination.

Chapter 2

BPEI/TEMPO-oxidized cellulose nanofibers sponges

2.1 Cellulose

Cellulose (CS; chemical formula: $(C_6H_{10}O_5)_n$) is one of the most abundant natural organic polymers on earth. It is a linear complex carbohydrate consisting of more than 3000 units of D-glucose linked together by β -(1,4) glucosidic linkages (Fig. 2.1).

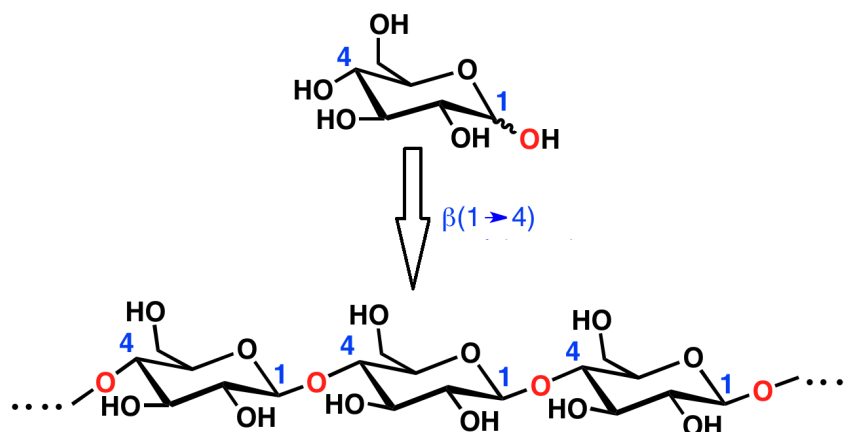


Figure 2.1: D-glucose unit (top) and cellulose linear chain (bottom).

The equatorial conformation of glucopyranose residues stabilizes the structure of the polymer by minimizing its flexibility. CS can be found in nature in fiber-based plants or inside the wood pulp [63], with a diameter ranging from from 2 to 20 nm

and with a length that goes from 100 to 40.000 nm (Fig. 2.2) [64].

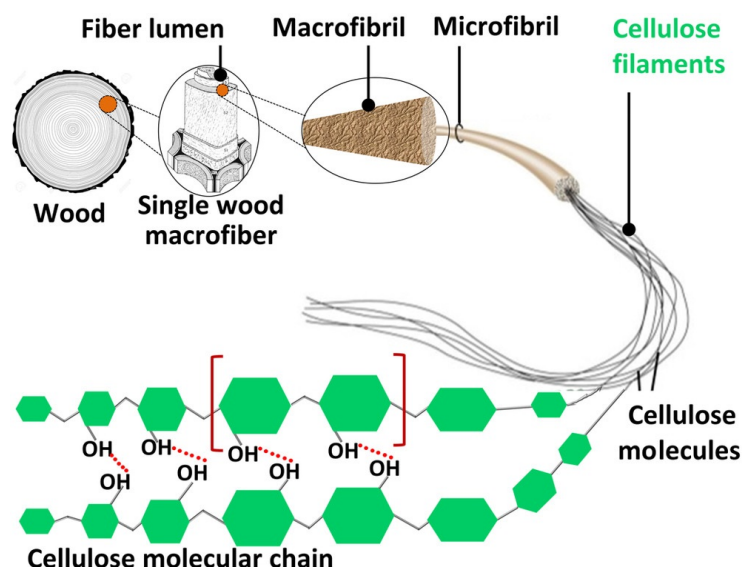


Figure 2.2: Schematic representation of the cellulose present in fibrous form inside wood pulp.

Cellulose is also produced, in a hydrated form, by several types of bacteria such as the *Acetobacter xylinum*.

The molecular structure can be found under different crystalline configurations including configuration I, which in turn is divided into $I\alpha$ and $I\beta$, configuration II and III. These structures differ from each other according to the number of residues (defined as number of glucose units) and to the water content involved (moles of water/moles of glucose).

When the hydroxyl groups of the first and last anomeric carbon (in the cyclic form of a carbohydrate, the anomeric carbon is the carbon that was part of the carbonyl group in the straight-chain structure; typically C1 and C4 of the D-glucose unit, see Fig. 2.1) are located on opposite sides of the glucosidic ring, the formation of an oxygen "bridge" between the two carbon atoms results in the typical linear and stable structure of cellulose (Fig. 2.3(a)). Conversely, when the groups are on the same side of the ring (α configuration), the resulting polysaccharide will assume a curved structure forming the so-called *amylose starch* (Fig. 2.3(b)). It is noteworthy that even though they share the same empirical formula, and exactly the same number of monomeric units, the significant differences in shape and size give them completely different properties.

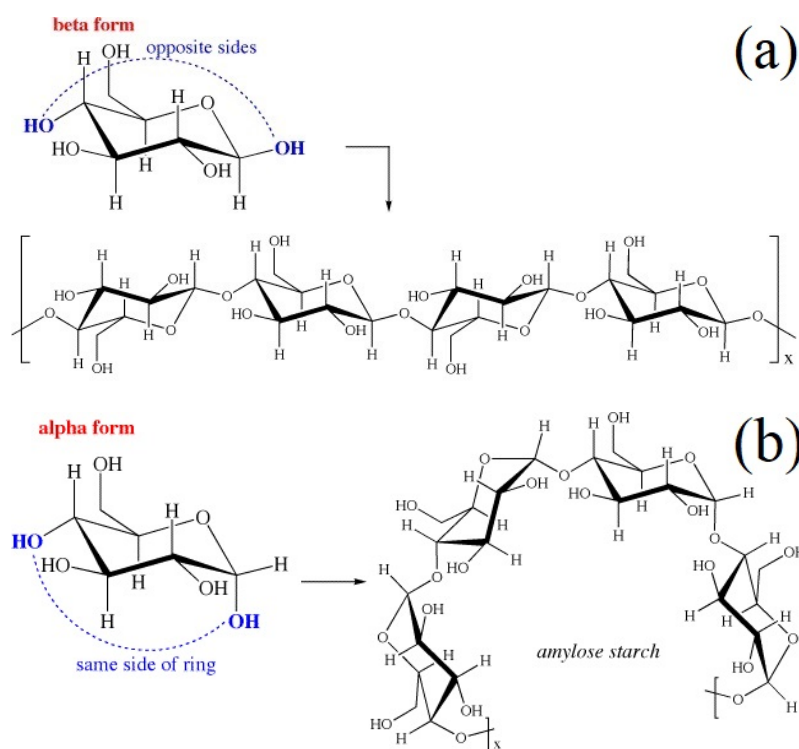


Figure 2.3: (a) Structure of cellulose and (b) amylose starch.

The crystalline state of natural cellulose is formed when the intramolecular and inter-fiber hydrogen bonds keep the polymeric network flat, allowing more hydrophobic polymeric planes to pile up with each other. Cellulose I contains two coexisting phases called $I\alpha$ (tricline form) and $I\beta$ (monocline form) in a ratio that strongly depends on the synthesis procedure. However, CS $I\alpha$ and CS $I\beta$ share the same inter-fiber distance (1,043 nm) but differ in the orientation of the crystalline planes [65].

While in CS $I\alpha$ adjacent planes are regularly arranged in the same direction with respect to each other, in CS $I\beta$ the planes, although always made up of D-glucose units that are crystallographically identical, are staggered (Fig. 2.4) [66].

Studies of density functional theory have shown that the energies associated with such configurations in CS $I\beta$ are of ~ 40 kJ/moles and 30 kJ/moles for intra- and inter-layers bonds, respectively [67–71]. A remarkable difference between the two crystallographic forms is related to the collective direction of the polymeric chains. In fact, while in the form I they are disposed parallel to each other, in CS II the latter are arranged with an anti-parallel pattern.

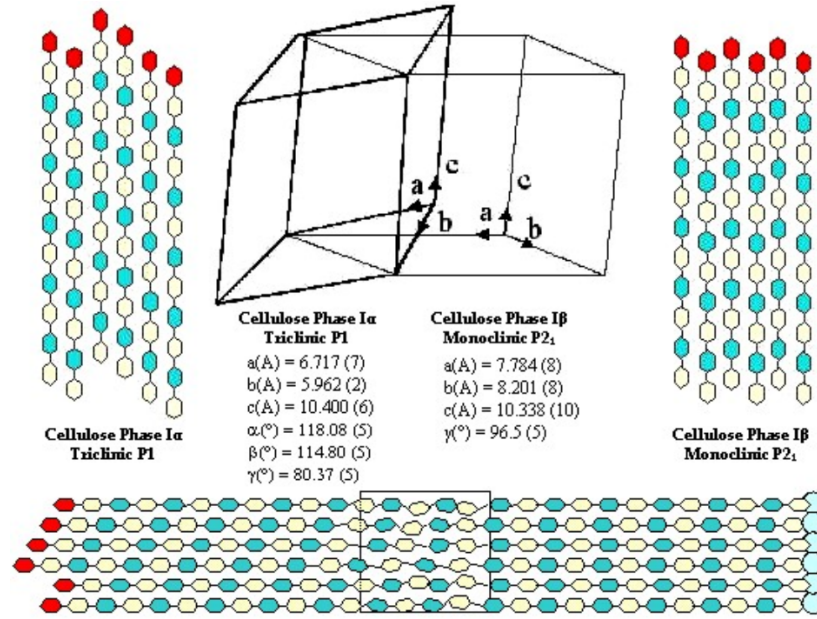


Figure 2.4: Relationship between unitary cells and difference between inter-chain conformations in tricline CS I α and monocline CS I β .

The antiparallel layout is thermodynamically more favoured than the parallel one. Finally, CS III, with a structure similar to CS II, shows the presence of needle-shaped nanocrystals with uniform dimensions of about 90 nm in length and 10 nm in width [72].

2.2 Water-cellulose interaction

According to recent experimental results [73], there are two distinct classes of water molecules that can be related to cellulose: the first concerns "bounded" water while the second refers to the water molecules contained within the cavities formed by the interlacing of CS fibers. In the first case, water molecules are closely attached to the cellulose surface and may diffuse within it for temperatures above 220 K. Below this temperature we assist to the formation of a glass. Water inside the polymeric vessels, on the other hand, acquires mobility at ~ 260 K.

In addition, the presence of water molecules seems to catalyze the CS crystals formation. This occurrence can be explained taking into account the contribution that water exerts in aligning the polymeric chains as a result of the activation of additional hydrogen bonds.

2.3 Nanocellulose

The technological and industrial development of cellulose nanofibers (CNFs) has represented, especially in the last few years, a challenging task in the field of the applied nanotechnologies. CNFs, together with crystalline nanocellulose (CNC), bacterial nanocellulose (BNC) and nanofibrillated cellulose (NFC), can be considered as part of a large class of materials which use nano-structured cellulose as main component.

CNFs are advanced materials composed of cellulose fibers of nanometre size with a high length/width ratio. Specifically, they exhibit width ranging from 5 to 20 nm and lengths up to few microns. They also show thixotropic properties, i.e. the ability to change their viscosity over time. In normal conditions, these systems show a viscosity that significantly differs from that observed under mechanical or thermal stress. In addition, the CNFs exhibit remarkable thermomechanical properties including high surface/volume ratio, high Young modulus and low thermal expansion coefficient [74–76]. The CNFs chemical-physical properties have been exploited over the last few years for the development of electronic and optoelectronic materials [77, 78], in the food science and in catalytic processes [79]. These nanofibers represent also an attractive solution for the development of energy-storage devices, in the preparation of carbon-sensitive membranes, and contribute to the improvement of the mechanical properties of building materials.

The CNFs are produced in many different ways depending on the characteristics and functions required.

Typically, cellulose nanofibers can be extracted from normal wood-based fibers present in plants, through mechanical techniques that involve the application of extremely intense shear stresses. The mechanical action reduces the mesoscopic fibers to increasingly smaller sizes, resulting in the formation of fibers of nanometric dimensions. Microfluidizers, ultrasonic homogenizers and high pressure homogenizers are commonly used for this purpose, although they require very high energy per tonne. To overcome this problem, enzymatic/mechanical pre-treatments are employed, as well as the introduction of charged groups through carboxymethylation or TEMPO-mediated oxidation. These pretreatments significantly reduce the energy consumption needed for producing CNFs below 1 MWh/tonne. Oxidation of the cellulose hydroxyl groups represents an efficient approach for the formation of

CNFs with highly reactive functional groups. Depending on the oxidising agent used, it is possible to synthesize CNFs containing aldehyde groups (through the use of NaClO_4) [80] or carboxylic acid moieties. In the latter case, the most used approach is based on the oxidation of NaClO (used as an oxidizing agent) mediated by the 2,2,6,6-tetramethyl-1-piperidinyloxy (TEMPO) radical and using NaBr as a co-catalyst [81, 82]. The so-obtained cellulose nanofibers (TEMPO-oxidized cellulose nanofibers, TOCNFs) exhibit a slightly smaller diameter if compared to those produced by acid treatments (typically from 2 to 5 nm), although they exhibit a significantly longer extension. This process, if conducted under basic conditions (pH 10 - 11), selectively converts the hydroxyl group C6 into the corresponding carboxylate, facilitating the formation of nanofibers after sonication (TEMPO-oxidized and ultra-sonicated cellulose nanofibers, TOUS-CNFs).

In the field of biotechnology CNFs can be considered an advanced material capable of fully replace the petrochemical-based solutions currently available. Use of green systems not only reduces the environmental impact but offers many advantages including the increase of the biodegradability, low cost and advantageous physical-mechanical-chemical properties. Although cellulose fibers can be extracted from algae, tunicates and bacterial cellulose, the greatest resource remains the plant cell. In this context it is clear how cellulose-based materials represent an emerging field for the development of the latest generation of materials for water treatment.

As already mentioned, the direct use of TOCNFs is limited because they are easily dispersible in water. This is why the corresponding hydrogels and aerogels lack of sufficient mechanical stability when immersed in aqueous solvents. Because of this, the introduction of amino groups in the cellulose network is needed to increase both the absorption capacity and the mechanical stability of the product itself. A convenient substrate with amino groups is represented by branched polyethyleneimine (bPEI), which acts as a cross-linking agent.

Branched polyethyleneimine (bPEI) is a non-linear poly-amine not soluble in water. It exhibits a high cation density, strong hydrophobicity and the presence of primary, secondary and tertiary amino groups in the 25/50/25 ratio (Fig. 2.5).

Branched polyethyleneimine is a latest-generation material with a wide range of applications such as water purification or as carrier for non-viral chemicals.

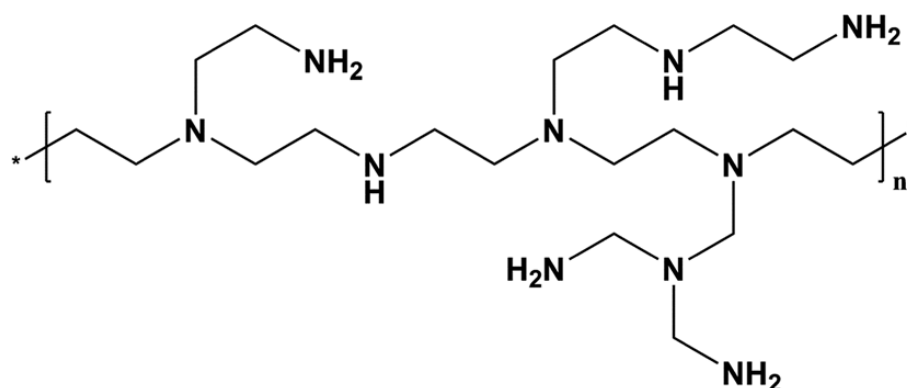


Figure 2.5: Chemical structure of branched polyethyleneimine.

The introduction of bPEI ($\text{H}(\text{NHCH}_2\text{CH}_2)_n\text{NH}_2$) into the cellulose polymer chain leads to a stabilization of the system in terms of structural rigidity, also improving the efficiency of absorption due to the presence of amino groups. bPEI/TOUS-CNFs systems are proved to exhibit a sponge-like porous structure with a two-dimensional sheet morphology (CNS).

On the basis of these considerations, in this work, the mechanisms of water confinement in bPEI/TOUS-CNFs sponges as a function of the hydration level and temperature was carried out.

2.4 BPEI/TOUS-CNFs sponges synthesis

Cotton linters cellulose was oxidized with TEMPO/NaClO/KBr as previously reported [83, 84]. Briefly, potassium bromide (1.54 g, 12.9 mmol) and 2,2,6,6-tetramethyl-1-piperidinyloxy (TEMPO) (215 mg, 1.38 mmol) were dissolved in water (0.57 L). After complete dissolution of TEMPO, cotton linters cellulose (10 g) was added to the solution under mechanical stirring, then a sodium hypochlorite solution (10% w/w, 44 mL, 74 mmol) was added dropwise in 1 h. The suspension was left react for 18 h. The pH was maintained around 11 by addition of NaOH 4M. After 18 h, the TEMPO oxidized cellulose was recovered by filtration using a Büchner funnel equipped with a sintered glass disc (nominal max. pore size: 16-40 mm) and further washed on the filter with HCl (aq, 1M) (3 x 250 mL) and deionized water (3 x 150 mL). After drying, a white solid (9.5 g, $Y = 95\%$) was collected.

The obtained white solid was vigorously dispersed in pure water (2.5-3.5% w/v) and the pH of the mixture was then regulated to 11 by addition of NaOH. The homogenous suspension was then sonicated at 0 °C for 30 min (Branson Sonifier 250 equipped with a 6.5 mm probe tip working at 20 kHz in continuous mode, with an output power 50% the nominal value (200 W)) in order to achieve TEMPO oxidized and ultra-sonicated cellulose nanofibers (TOUS-CNFs) gel-like dispersion.

We performed the preparation of CNS following the procedure already described in literature [21, 23, 85] with a process sequence summarized in Fig. 2.6.

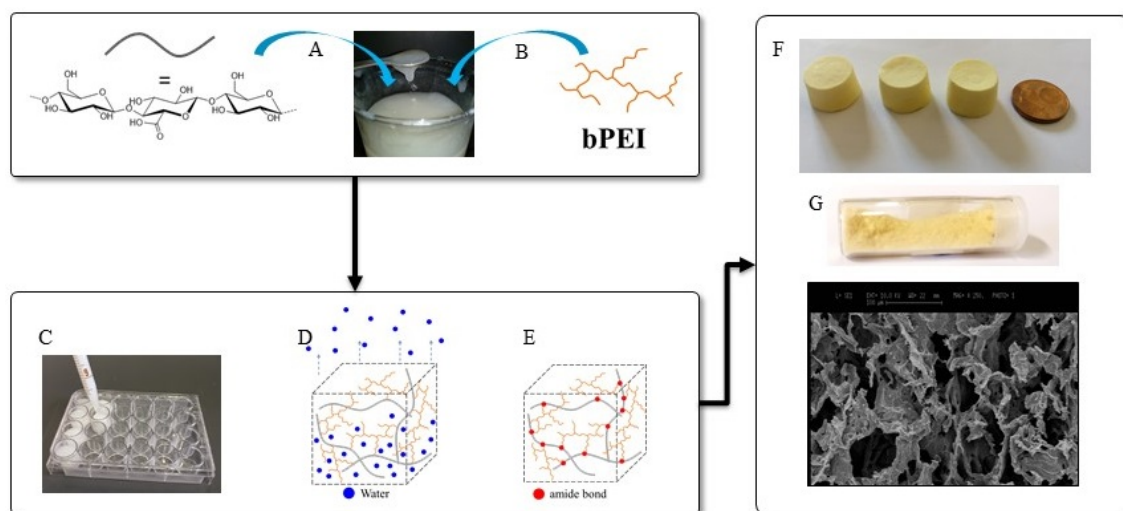


Figure 2.6: Cellulose nanosponge (CNS) preparation sequence: TOUS-CNFs are dispersed in water at 2.5% w/v concentration and sonicated obtaining an homogeneous dispersion (A), then a bPEI solution is added to the TOUS-CNFs dispersion (B). The mixture is placed in molds and frozen (C). Water is then removed by freeze-drying (D), after that thermal treatment leads to the formation of amide bonds and reticulation (E). The material is finally washed in order to remove non-reticulated components. The obtained cellulose nanosponge (CNS) (F) can be grinded in order to obtain a homogeneous powder (G).

The TOUS-CNF gel-like dispersion was acidified with HCl 2 M until pH about 3, the residue was recovered with a Büchner funnel and washed with abundant pure water until the filtrate reached pH 6/7. The obtained TOUS-CNFs were dispersed again in pure water (3% w/v), where branched polyethyleneimine (bPEI, 25 kDa) and, in one formulation, citric acid (CA) were added in the ratios according to Table 1. The mixture was sonicated again at 0 °C for 10 min. The obtained viscous gels were transferred into a 24-well plate, frozen at -80 °C and freeze-dried for 48 h,

affording the corresponding sponge which, in turn, were treated in oven (103 °C, 16 h). The resulting sponge-like materials were removed from the molds. Then, they were washed with methanol in a Soxhlet apparatus for 24 h under reflux. After that, they were dried and stored in dry environment. The dry CNSs were finally grinded in a mortar achieving a homogeneous fine powder (Fig. 2.6(G)).

In the following table the investigated samples are reported, together with the bPEI and TOUS-CNFs weight fractions.

Sample	bPEI (g)	TOUS-CNFs (g)	CA (g)
CNS (0.2:1)	0.2	1	-
CNS (0.5:1)	0.5	1	-
CNS (1:1)	1	1	-
CNS (2:1)	2	1	-
CNS (2:1)-CA	2	1	0.52

Table 1. List of CNS samples under investigation.

Chapter 3

Experimental

3.1 Neutron scattering

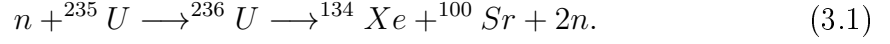
3.1.1 Introduction

Neutrons (Ns) are sub-nuclear particles (mass = 1.675×10^{-27} Kg) made up of two quark down and one quark up linked together by strong nuclear interactions. Being electrically neutral, they are able to deeply penetrate into materials and couple with atomic nuclei by means of an extremely strong short-range interaction ($\sim 10^{-15}$ m). As a consequence, neutrons can travel for long distances through most materials without being scattered or absorbed. Neutrons have also a non-zero spin momentum which allow the study of the magnetic structure and its fluctuation down to microscopic levels by interactions with the unpaired electrons. It is worth noting that neutrons are naturally unstable (mean-life time of about 893 s); they spontaneously tend to decay in a proton, an electron and an anti-neutrino and that is the reason why neutrons must be produced in nuclear reactors.

3.1.2 Fission sources

Neutron flux can be provided by means of two different processes: *nuclear fission* and *spallation*. In nuclear fission, a heavy nucleus (generally ^{235}U or ^{239}Pu) splits into two lighter ones releasing γ -rays, neutrons and other residuals. During the process, a heavy nucleus absorbs a rambling neutron coming from a spontaneous fission or by the environment, giving rise to a strongly unstable ^{236}U atom. The

latter can split in a large variety of different ways, such as:



The surplus of neutrons coming from this initial reaction is able to self-sustain an avalanche process which yields, at least, to a continuous neutron flux of about $\sim 10^{15} \text{ s}^{-1} \text{ cm}^{-2}$. However, Neutrons produced from the reactor core are too fast (highly energetic) to be used in scattering experiments, which means that they must be *moderated* slowing down their velocity (and hence their energy). This purpose is achieved by interposing *moderators* (Ms) between the reactor core and the sample. Ms are generally materials with a neutron cross section capable to interact with fast neutrons in such a way to reduce their energy without being absorbed. Accordingly, it is possible to obtain an out-coming neutron speed spectrum which can be approximated to a Maxwell-Boltzmann function like that displayed in Fig. 3.1.

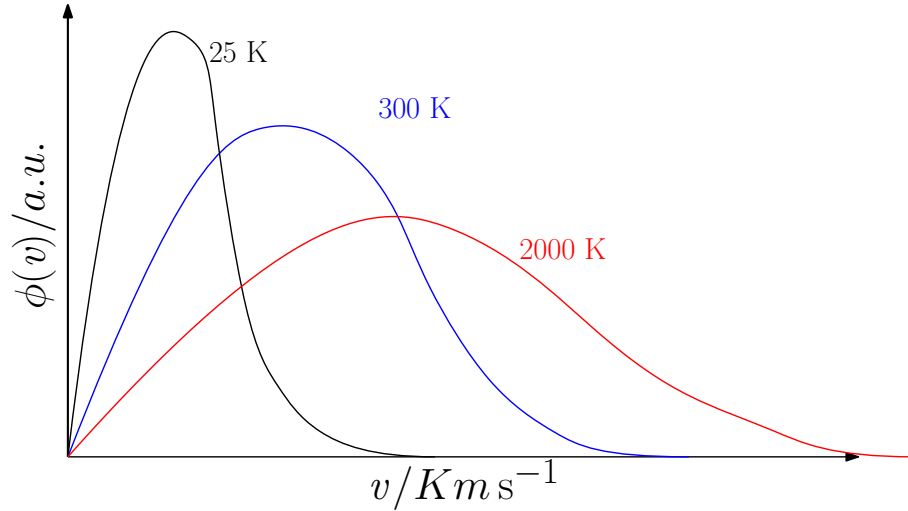


Figure 3.1: Maxwellian flux distribution for three temperatures of moderators.

Nowadays there are three kinds of moderators: light water (H_2O), heavy water (D_2O) and graphite. The moderation process deals with elastic collisions between fast neutrons coming from the reactor core and the slow nuclei of the moderator medium.

Changes in velocity can be calculated by applying the principles of conservation of momentum and kinetic energy. If M_i is the mass of the i -st moderator nucleus and m_i that of the i -st coming neutron, according to the principle of conservation

of momentum we have:

$$m_i v = m_i v' + M_i v'' , \quad (3.2)$$

where v is the velocity of the incoming neutron, v' the velocity after the collision and v'' the velocity acquired by the moderator nucleus. On the other side, from the conservation of the kinetic energy we have:

$$\frac{1}{2} m_i v^2 = \frac{1}{2} m_i v'^2 + \frac{1}{2} M_i v''^2 . \quad (3.3)$$

After a simple mathematical arrangement, combining Eqn. 3.2 and Eqn. 3.3 we obtain

$$v'/v = \frac{m_i - M_i}{m_i + M_i} . \quad (3.4)$$

The ratio of v'/v is negative if $m_i < M_i$, meaning that m_i bounces backwards, while both particles move forward when $m_i > M_i$. The speed of the incident particle is smallest after the encounter, in fact zero, when $m_i = M_i$. Hence, Eqn. 3.4 supports the assertion that the energy exchange in collisions is greatest for particles of similar mass, and explains why neutron moderators consist of light materials.

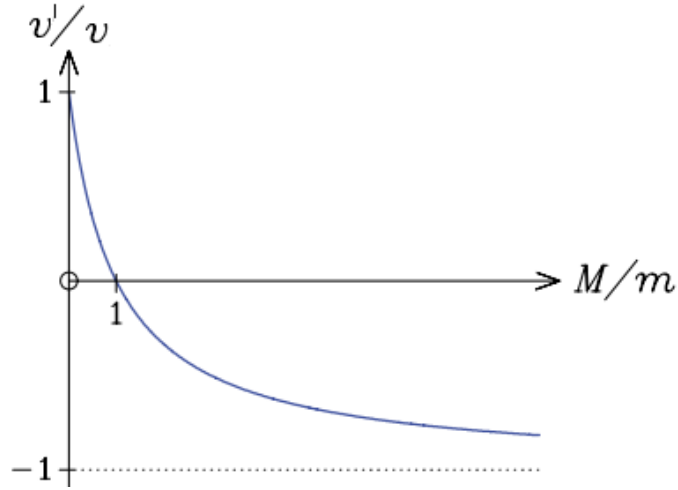


Figure 3.2: Trend of v'/v as a function of M/m .

In particular, D₂O moderators at a temperature of 294 K allow the outcoming of 25 meV neutrons corresponding to a wavelength of about 1.8 Å. It is worth emphasizing how in some kind of experiment cold neutrons (high wavelengths) are required (i.e. when using Small Angle Neutron Scattering technique). They can be produced by means of a liquid hydrogen moderator at 20 K.

3.1.3 Spallation sources

A high energetic ion beam (approx. 70 MeV), produced by a linear accelerator, is pumped into an acceleration synchrotron ring in order to increase its energy. Accordingly, ion beams of 600-800 MeV are produced. These energetic beams are collimated into neutron-rich targets (^{138}W or ^{238}U) knocking out 10-30 neutrons per collision. After that, the out-coming neutrons are moderated and finally collimated to the investigated systems. Neutrons produced by the spallation process are less energetic respect to those obtained by fission.

3.2 Small Angle Neutron Scattering (SANS)

The Small Angle Neutron Scattering (SANS) technique is an extremely powerful method to probe nano-structures (from 1 to 500 nm) by analysing the diffraction pattern of the elastic signal at very low scattering angles. In principle, the larger is the investigated sample the lower will be the momentum transfer Q compared to the position of the first Bragg peak in the structure factor. In order to access to the low Q range (0.005 up to 0.5 \AA^{-1}), cold moderators and low angles must be achieved. Experiments which focus on $Q < 1 \text{ nm}^{-1}$, such as those performed by SANS technique, provide a very low-resolution structural view of molecules and aggregates inside the sample, since the analysis of the resulting scattering pattern provides information about size, shape and correlations within the sample. SANS usually probes diffusion angles ranging between 0.2 and 20 degrees. It is worth noting that SANS measurements allow us to obtain direct information about the sample in the reciprocal space. For this reason, all data acquired must be processed from the reciprocal space to the real one by means of a Fourier transformation (FT). In the case of multi-phases materials (colloids, colloid suspensions, branched polymers, etc), SANS measurements allow to get structural information about single components because of the different way of interaction with neutrons due to the different scattering length densities (SLDs).

More in detail, in a common SANS experiment, a collimated neutron beam interacts with an ensemble of nuclei within the so-called *scattering volume*. All scattering events satisfy both the energy and the moment conservation principles. According to these let's consider a two-dimensional detector (or a set of detection

elements) of $dxdy$ size placed in a distance L and oriented at an angle of 2θ with respect to the sample (see Fig. 3.3). This element records the flow of scattered radiation within a solid angle equal to:

$$\Omega = dxdy/L^2. \quad (3.5)$$

Let us define \mathbf{k}_i and \mathbf{k}_f the incident and scattered wavevectors, respectively. Since SANS measurements exploit the coherent elastic signal coming from the sample:

$$|\mathbf{k}_i| = |\mathbf{k}_f|. \quad (3.6)$$

It can be demonstrated by geometric considerations that the wavevector transfer \mathbf{Q} , defined as $\mathbf{k}_i - \mathbf{k}_f$, can be written as:

$$Q = |\mathbf{Q}| = |\mathbf{k}_i - \mathbf{k}_f| = \frac{4\pi}{\lambda} \sin(\theta), \quad (3.7)$$

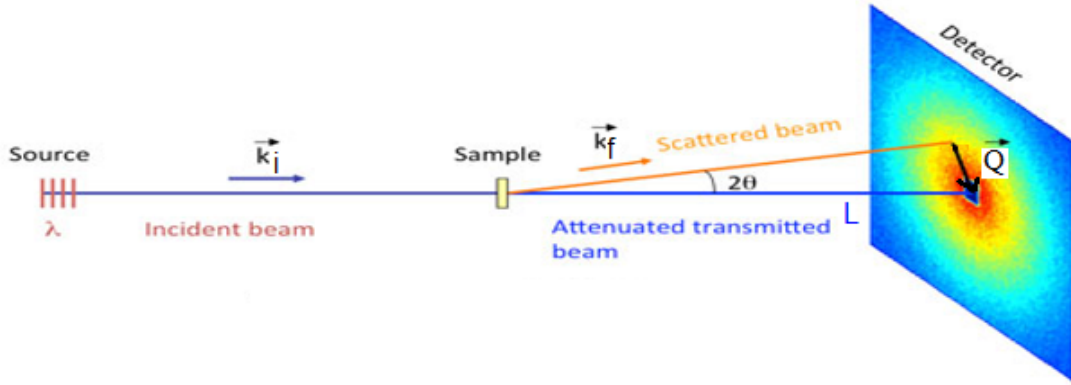


Figure 3.3: Typical scattering geometry.

where λ is the incoming neutron wavelength. In ordered materials, where the atomic positions are equally spaced and periodical, Eqn. 3.7 can be written as:

$$Q = |\mathbf{Q}| = 4\pi/d, \quad (3.8)$$

with d equal to distance between planes of the reticular lattice.

According to this, the study of macromolecular systems, which are characterized by larger size domains, requires access to low Q values - being Q and d inversely proportional [86]. This is well evident by an inspection of Fig. 3.4, that reports an example of behaviour of the small angle scattering intensity as a function of the wavevector transfer Q .

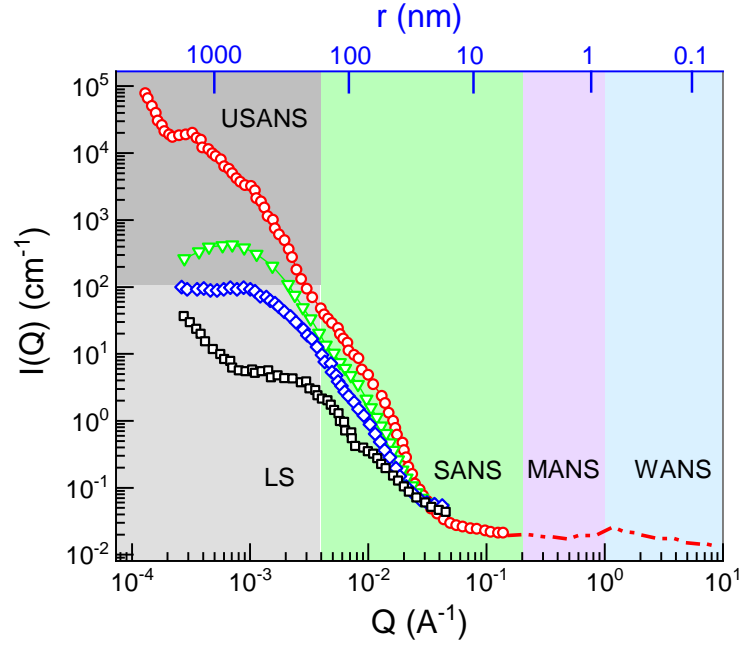


Figure 3.4: Small angle scattering intensity as a function of the wavevector transfer Q .

This example highlights the relationship between reciprocal space and real space and how some regions, although not accessible through the SANS technique, can be analyzed using different strategies that exploit, in any case, similar principles such as the Wide-Angle Neutron Scattering (WANS), Medium-Angle Neutron Scattering (MANS), Ultra Small-Angle Neutron Scattering (USANS) and Light Scattering (LS).

In small angles approximation, the relation between momentum and scattering angle can be written as:

$$Q = \frac{4\pi \sin\theta}{\lambda} \approx \frac{4\pi\theta}{\lambda}, \quad (3.9)$$

which means that low- Q values can be achieved both by reducing the scattering angle θ or increasing the neutron wavelength λ .

Let us consider a simple system composed of spherical particles spread within a solvent. The intensity of the measured elastic signal, $I_{el}(Q, \lambda)$, is related to the *microscopic differential cross-section* $(d\sigma/d\Omega)_{el}$ by:

$$I_{el}(Q, \lambda) = I_0(\lambda)\eta(\lambda)T(\lambda)\Delta\Omega \left(\frac{d\sigma}{d\Omega} \right)_{el} \otimes R(Q) + B(Q), \quad (3.10)$$

where:

- $I_0(\lambda)$: incident flux
- $\eta(\lambda)$: detector efficiency
- $T(\lambda)$: transmission function of the sample
- $\Delta\Omega$: solid angle covered by the detector
- $\left(\frac{d\sigma}{d\Omega} \right)_{el}$: *microscopic differential cross-section*

The term $R(Q)$ takes into account the resolution function of the instrument while $B(Q)$ is a background term slowly variable. All the information about the structure and correlations of the sample are contained in the *microscopic differential cross-section* $(d\sigma/d\Omega)_{el}$ or, equivalently, in the *macroscopic differential cross-section*:

$$\left(\frac{d\Sigma}{d\Omega} \right)_{el} = \frac{1}{V} \left(\frac{d\sigma}{d\Omega} \right)_{el},$$

where V is the volume of the sample.

The relation between the *microscopic differential cross-section* $(d\sigma/d\Omega)_{el}$ and the neutron scattering tendency of a given material, accounted by the *scattering length density* $\rho(\mathbf{R})$, can be obtained by considering what happens if a stream of neutrons encounter an assembly of nuclei.

Briefly, let us consider first a flux of monochromatic neutrons like a complex plane-wave $\psi_i = \psi_0 e^{i\mathbf{k}_i \cdot \mathbf{r}}$, of wavevector \mathbf{k}_i and energy E , interacting with a single fixed atom.

Unlike the incident beam, which is collimated by the instrument, the number of outgoing particles per unit area will fall with the distance \mathbf{r} according to the

inverse-square law. Hence, the scattered wave will take the general form:

$$\psi_f = \psi_0 f(\lambda, \theta) \frac{e^{i\mathbf{k}_f \mathbf{r}}}{r} = \psi_0 f(\lambda, \theta) \frac{e^{ikr}}{r}. \quad (3.11)$$

The replacing of $e^{i\mathbf{k}_f \mathbf{r}}/r$ with e^{ikr}/r is possible only if the origin is centred on the atom, so that the wavevector \mathbf{k}_f is parallel to the displacement vector \mathbf{r} .

Here, the function $f(\lambda, \theta)$ give us information about the chances that a particle of a given wavelength is deflected in a certain direction.

If we now consider a particular atom, labelled by the index j inside the sample, it will make a small contribution to the scattered wave function, $[\delta\psi_f]_j$, of the general form in Eqn. 3.11:

$$[\delta\psi_f]_j = \psi_0 e^{i\mathbf{k}_i \mathbf{R}_j} f_j(\lambda, \theta) \frac{e^{i\mathbf{k}_f (\mathbf{r} - \mathbf{R}_j)}}{|\mathbf{r} - \mathbf{R}_j|}, \quad (3.12)$$

where $f_j(\lambda, \theta)$ defines the relevant interaction characteristics of the j -th atom located at a position \mathbf{R}_j relative to an arbitrarily defined origin somewhere in the sample, \mathbf{k}_f is the wavevector of the outgoing particle and \mathbf{r} is an arbitrary position.

Assuming that the only non-zero component of the incident neutron wavevector is the z-one ($\mathbf{k}_i \equiv (0, 0, k)$), the scattering geometry can be arranged as in Fig. 3.5.

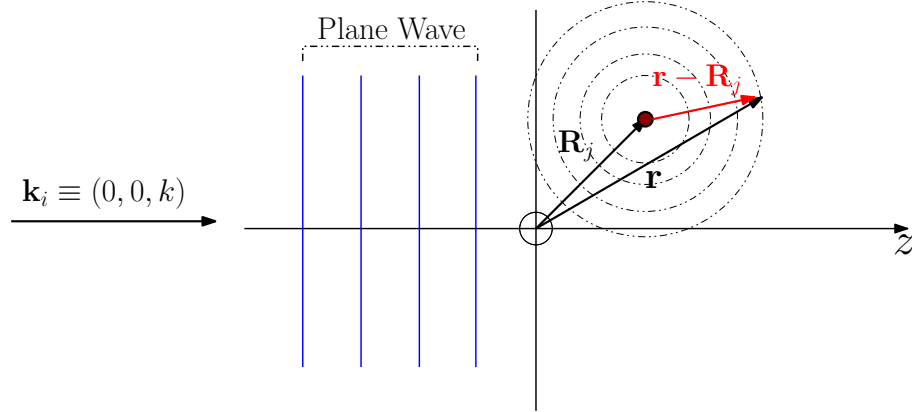


Figure 3.5: Contribution to the total scattered wave from atom j located at \mathbf{R}_j .

The choice of displacing the position of the nucleus away from the origin allows us to easily sum up each contributions coming out from all N atoms in the sample. According to the superposition principle, the total scattered wave ψ_f can be written

as a summation of Eqn. 3.12 over all nuclei positions:

$$\psi_f = \psi_0 \sum_{j=1}^N e^{i\mathbf{k}_i \mathbf{R}_j} f_j(\lambda, \theta) \frac{e^{i\mathbf{k}_f(\mathbf{r}-\mathbf{R}_j)}}{|\mathbf{r}-\mathbf{R}_j|}. \quad (3.13)$$

Taking outside every contribution in which j is not involved, we obtain:

$$\psi_f = \psi_0 e^{i\mathbf{k}_f \mathbf{r}} \sum_{j=1}^N f_j(\lambda, \theta) \frac{e^{i(\mathbf{k}_i - \mathbf{k}_f) \mathbf{R}_j}}{|\mathbf{r}-\mathbf{R}_j|} = \psi_0 e^{i\mathbf{k}_f \mathbf{r}} \sum_{j=1}^N f_j(\lambda, \theta) \frac{e^{i\mathbf{Q} \mathbf{R}_j}}{|\mathbf{r}-\mathbf{R}_j|}, \quad (3.14)$$

where $\mathbf{Q} = \mathbf{k}_i - \mathbf{k}_f$ is the *wavevector transfer* of Eqn. 3.7.

In this derivation, we implicitly assumed that the scattered wavefunction does not influence (or, at least, in a limited way) the incoming neutron wavefunction. This condition is usually referred as *Born* or *Kinematical* approximation. Events where particles are deflected more than once have also been ignored, and this is true only for very low interaction rates. Depending on the size of the sample, and the geometry of the experimental setup, corrections for multiple scattering may be needed.

The size of the sample illuminated by the incident beam is usually much smaller than the distance at which scattering measurements are taken (see Fig. 3.6), so with very good approximation we can write:

$$|\mathbf{r}-\mathbf{R}_j| = |\mathbf{r}| = r. \quad (3.15)$$

In this approximation, known as *Fraunhofer approximation*, $\mathbf{r}-\mathbf{R}_j$ can be replaced with r in Eqn. 3.14 and taken outside the summation, obtaining:

$$\psi_f = \psi_0 \frac{e^{i\mathbf{k}_f \mathbf{r}}}{r} \sum_{j=1}^N f_j(\lambda, \theta) e^{i\mathbf{Q} \mathbf{R}_j}. \quad (3.16)$$

Now, the number of scattered neutrons can be calculated by taking the squared modulus of Eqn. 3.16 in the form:

$$|\psi_f|^2 = \frac{|\psi_0|^2}{r^2} \left| \sum_{j=1}^N f_j(\lambda, \theta) e^{i\mathbf{Q} \mathbf{R}_j} \right|^2 = \frac{\Psi}{r^2} \left| \sum_{j=1}^N f_j(\lambda, \theta) e^{i\mathbf{Q} \mathbf{R}_j} \right|^2, \quad (3.17)$$

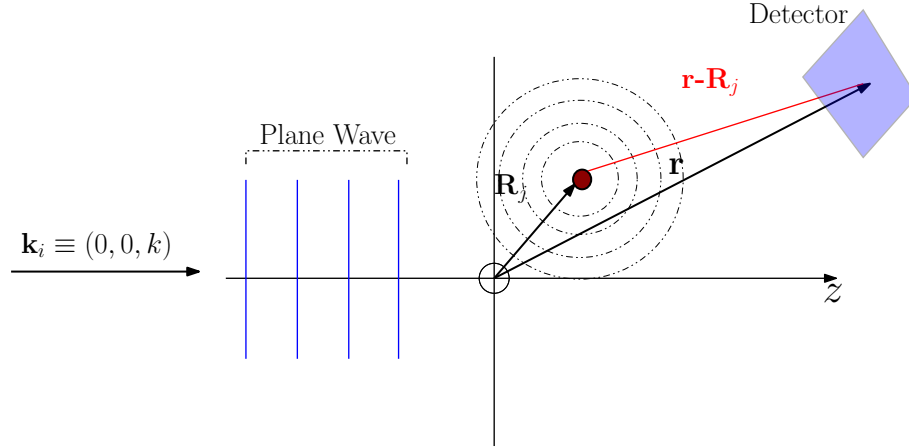


Figure 3.6: Sample-detector distance representation.

being $|e^{i\mathbf{k}_f \mathbf{r}}|^2 = 1$, and $\Psi = |\psi_0|^2$ equal to the incident neutron flux.

The number of neutrons Γ elastically scattered which strike a portion of the detector surface dS per unit time (see Fig. 3.7) can be written as the product between the number of the total outgoing neutrons (Eqn. 3.17) multiplied by the section dS itself:

$$\Gamma = |\psi_f|^2 \times dS \quad (3.18)$$

$$\Gamma = |\psi_f|^2 dS = \frac{\Psi dS}{r^2} \left| \sum_{j=1}^N f_j(\lambda, \theta) e^{i\mathbf{Q}\mathbf{R}_j} \right|^2 = \Psi d\Omega \left| \sum_{j=1}^N f_j(\lambda, \theta) e^{i\mathbf{Q}\mathbf{R}_j} \right|^2, \quad (3.19)$$

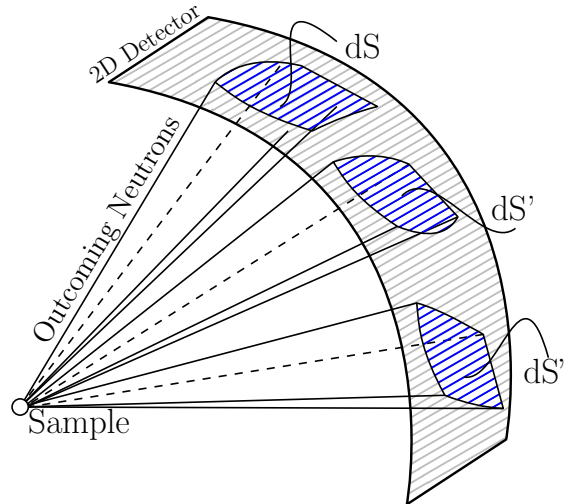


Figure 3.7: Number of scattered neutrons on different sections of the 2D detector.

where $d\Omega = dS/r^2$ is the solid angle subtended by the detector at the sample.

Since the *microscopic differential cross-section* is defined as the *number of scattered neutrons per second into a solid angle $d\Omega$* divided by the incident flux Ψ :

$$\left(\frac{d\sigma}{d\Omega}\right)_{el} = \frac{\Gamma/d\Omega}{\Psi} = \frac{\Gamma}{d\Omega \times \Psi}, \quad (3.20)$$

by replacing Eqn. 3.19 into Eqn. 3.20 we have:

$$\left(\frac{d\sigma}{d\Omega}\right)_{el} = \frac{\Psi d\Omega}{\Psi d\Omega} \left| \sum_{j=1}^N f_j(\lambda, \theta) e^{i\mathbf{Q}\cdot\mathbf{R}_j} \right|^2 = \left| \sum_{j=1}^N f_j(\lambda, \theta) e^{i\mathbf{Q}\cdot\mathbf{R}_j} \right|^2. \quad (3.21)$$

Eqn. 3.21 relates the microscopic differential cross-section to the structure of a material composed of N atoms of type $f_j(\lambda, \theta)$, located at \mathbf{R}_j with respect to an arbitrary origin.

It is worth of note that the characteristics of $f_j(\lambda, \theta)$ are different for X-rays and neutrons, and are also strongly dependent by the size and shape of the scattering object. In the case of neutrons $f_j(\lambda, \theta)$ tends to be invariant with respect to wavelength and scattering angle:

$$f_j(\lambda, \theta) = -b_j,$$

where the constant b_j is called *neutron scattering length* (of the j -st atom) and the minus sign is a matter of convention.

Typically, $f(\lambda, \theta)$ is quantified in terms of a scattering length density (SLD) function, $\rho(\mathbf{R})$ (with SI units of m^{-2}) of the appropriate scattering material; nuclear or electron depending on the type of probe and interaction. It increases with the macroscopic density up to high values for highly compacted materials and it's also a function of the individual scattering lengths. As already mentioned, $\rho(\mathbf{R})$ can be considered in this case as a measure of the neutron scattering tendency of a material.

According to this, an infinitesimally small volume dV , at a location \mathbf{R} , will contain a point source of isotropic scattering with:

$$f(\lambda, \theta) = \rho(x, y, z)dV = \rho(\mathbf{R}) d^3\mathbf{R}. \quad (3.22)$$

By replacing the summation over j with a three dimensional integral over the scattering volume in Eqn. 3.21, we obtain:

$$\left(\frac{d\sigma}{d\Omega}\right)_{el} = \left| \iiint_V d^3\mathbf{R} \rho(\mathbf{R}) e^{i\mathbf{Q}\cdot\mathbf{R}} \right|^2, \quad (3.23)$$

with V equal to the volume where the scattering process occurs. Taking into account the Fourier transform (FT) properties, Eqn. 3.23 tells us that the elastic component of the *microscopic differential cross-section* is related to the structure of the material through the Fourier Transform of the SLD function $\rho(\mathbf{R})$.

If the system is assumed to be incompressible, the SANS *microscopic differential cross-section* $(d\sigma/d\Omega)_{el}$ can be modeled as:

$$\left(\frac{d\sigma}{d\Omega}\right)_{el} = N V_p^2 (\varrho - \varrho_0)^2 P(Q) * S(Q), \quad (3.24)$$

where N is the number of particles contained within the investigated sample, V_p the volume of the particle/scattering object and $\varrho - \varrho_0$, defined as "contrast", is related to the difference in the scattering length density between solvent and solute. $P(Q)$ and $S(Q)$ are the single particle *form factor* and *structure factor*, respectively. The form factor takes into account the contribution of the coherent scattering signal due to the shape of the particles/molecules. It comes from interferences produced by scattered neutrons which are contained inside the same scattering object. The structure factor, on the other side, takes into account the presence of spatial correlations induced by interactions between different components. For a monatomic samples it can be written as:

$$S(Q) = 1 + \frac{4\pi n}{Q} \int_0^\infty r[g(r) - 1] \sin(Qr) dr, \quad (3.25)$$

where $g(r)$ is the pair-distribution function and n is the atomic number density. No spatial correlation means that $g(r)$ tends to 1 and hence $S(Q) \rightarrow 1$.

In Fig. 3.8, different trends of $P(Q)$ for some particular shapes are reported as a function of the wavevector transfer.

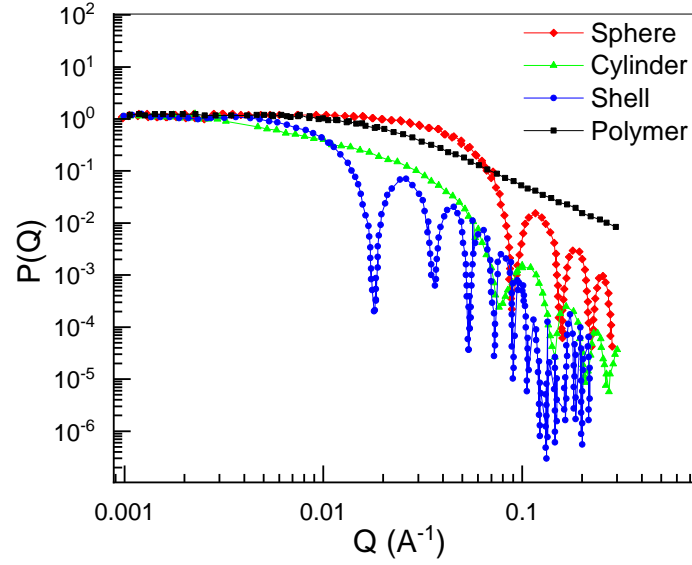


Figure 3.8: Form factor $P(Q)$ as a function of the wavevector transfer Q for some common shapes (sphere, cylinder, branched polymer, etc.).

It is worth of note that according to [Eqn. 3.24](#), for a non-zero scattered beam the term $\varrho - \varrho_0$ must be $\neq 0$. This means that the detection of structures in the investigated system can be possible only if the scattering length density of objects is numerically different from that of the surrounding medium.

Let us consider a scattering volume containing sphere of two different SLDs ([Fig. 3.9](#)); specifically, ϱ_1 for green spheres and ϱ_2 for the red ones, dispersed in a liquid medium having SLD equal to ϱ_0 . Also assume that the green spheres have $\rho_1 < \rho_0$ and that the red spheres have $\rho_2 > \rho_0$. It is worth noting that the green and red spheres are identical except for their scattering length densities (i.e., “color” as appearing to neutrons).

The scattered intensity, being susceptible to the difference squared of the solute-solvent SLDs, will not be able to distinguish between the two objects because both of them are characterized by a positive contrast factor $(\varrho_1 - \varrho_0)^2 > 0$ and $(\varrho_2 - \varrho_0)^2 > 0$ and therefore appear the same.

In order to overcome this problem, a second sample is necessary whereby the scattering length density of the solvent matches that of one of the two spheres for example when $\varrho_1 = \varrho_0$ (or $\varrho_2 = \varrho_0$) ([Fig. 3.10](#)).

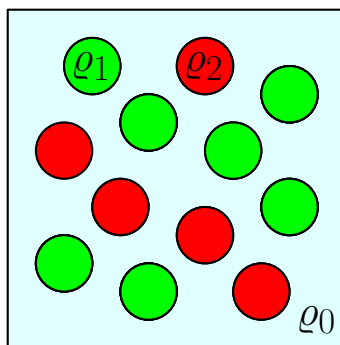


Figure 3.9: Graphical representation of a system containing two different types of spheres with SLDs of ϱ_1 and ϱ_2 , respectively, dispersed in a medium of SLD ϱ_0 .

In this way it is possible to eliminate the scattered contribution of such component making it "invisible" to the incoming neutron beam. As a result, single-component information can be obtained even in complex systems characterized by the presence of coexistent multi-phases.

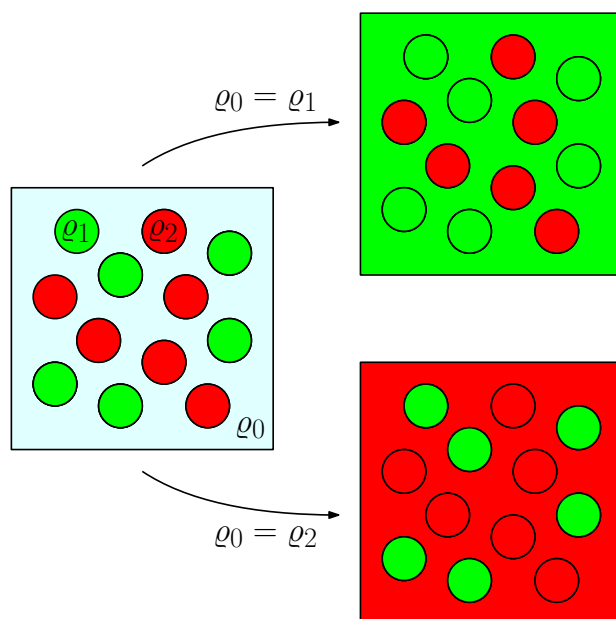


Figure 3.10: A schematic illustration of contrast matching in the case of $\varrho_0 = \varrho_1$ and $\varrho_0 = \varrho_2$.

This experimental procedure is known in literature as "matching" or "phase contrast", particularly useful for studying biomolecules and carbon-based structures.

3.2.1 Porod approximation

Debye (Debye 1949) and later Porod (Porod 1951) have shown that in a two phases system the SANS profile can be characterized by a constant value, called Porod invariant denoted by Δ , (Eqn. 3.26), which is independent by the scattering length density distribution:

$$\Delta = \int_0^\infty \left(\frac{d\Sigma}{d\Omega} \right)_{el} Q^2 dQ = 2\pi(\rho - \rho_0)^2 O_S, \quad (3.26)$$

where $(d\Sigma/d\Omega)_{el}$, $\rho - \rho_0$ and O_S are the *macroscopic differential cross-section*, the contrast term and the specific surface, respectively. For sharp surfaces between different scattering domains, the specific surface O_S can be calculated by the following relation:

$$O_s = S/V = \pi \frac{[I(Q)Q^{-4}]_{Q \rightarrow \infty}}{C}. \quad (3.27)$$

The logarithm of the intensity as a function of the logarithm of Q gives, as a result, a line of slope -4. If we represent $I(Q)Q^{-4}$ as function of Q^{-4} , the slope of the curve gives a measurements of the incoherent background scattering. Furthermore, the intersection with the y-axis allows us to obtain the value of the Porod invariant. Determining the specific surface is of extreme importance when the size of the scattering objects is equal or larger than the measuring limit, or in case of random phase containing structures, where the phases grow randomly into each other, but the surface between them is sharp. When this surface is diffuse, the scattering length density will change continuously across the surface, therefore the exponent of Q will be lower than -4. If the surface is fractal-like, the exponent value will be larger than -4.

3.2.2 Guinier approximation

In dilute systems, for values $QR \ll 1$ (with R equal to the particle radius), the scattered intensity can be written as:

$$I(Q) = (\rho - \rho_0)^2 V^2 e^{-Q^2 R_g^2/3}, \quad (3.28)$$

where R_g is the *gyration radius* and V the volume. In practice, the natural logarithm of the measured intensity ($\ln(Q^2)$) is represented versus Q^2 . The slope of the obtained profile yields to the exact value of the gyration radius. If the scattering object has simple shapes, its radius can be easily calculated.

Shape	Gyration Radius
Sphere (radius R)	$R_g^2 = 3/5 R^2$
Ellipsoid (axis a , b and c)	$R_g^2 = a^2 + b^2 + c^2/5$
Cylinder (length L and radius r)	$R_g^2 = L^2/12 + r^2/2$

3.3 SANS diffractometer "Yellow Submarine"

In this thesis, SANS measurements were performed at the "Yellow Submarine" (YS) diffractometer of the Budapest Neutron Reactor (BNC) in Hungary (Figs. 3.11 and 3.12).

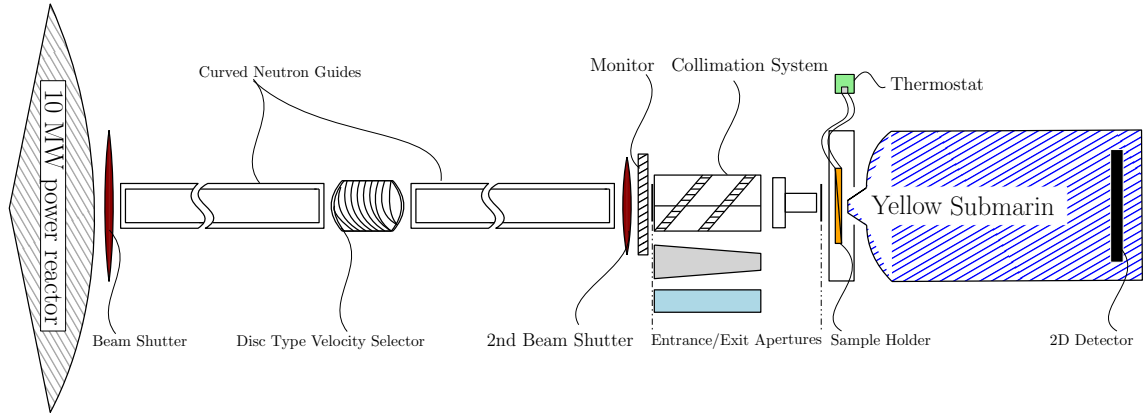


Figure 3.11: Scheme of the SANS diffractometer Yellow Submarine.



Figure 3.12: Yellow Submarine diffractometer.

The YS operates at the VVR type 10 MW power research reactor at the Budapest Neutron Centre. This produces neutrons with energies of about 1 - 2 MeV then slowed down in a light water moderator. For the purpose of this work, further slowing is needed, which is achieved in a cold source consisting of a helium cooled

cell containing liquid hydrogen. After a series of collisions with hydrogen nuclei having temperature of 20 K, neutrons are slowed down to wavelength between 3 - 25 Å. These neutrons are guided through a series of boron-based glass plates coated with nickel-titanium layers whose reflectivity can be tuned up to 0.8 – 0.9. They allow neutrons to pass from the reactor source to the sample with minimum loss.

Another factor which contributes to the initial intensity and divergence of the incoming neutron beam is the collimation. In the YS, collimation is achieved by using tubes under vacuum that contain diaphragms made up of neutron absorbing materials. Diaphragms define the diameter and the divergence of the beam. Shorter collimation length leads to higher neutron intensity and more divergent beam, while large collimation distances will decrease the divergence, reducing the neutron intensity. For an optimal intensity-resolution combination, usually the collimation length is chosen to be similar to the sample-to-detector distance. On the YS, a 4.7 m collimation length is used. The beam diameter at the sample position can be chosen between 2 mm and 16 mm. For monitoring the incoming neutron flux variations in time, a uranium fission chamber is used with 0.1 % efficiency. For detecting the thermal neutrons scattered from the sample nuclear reactions are involved. The detector at the YS instrument uses the $n(^{10}\text{B},\alpha)^7\text{Li}$ reaction. The α particles ionize the gas and induce a current proportional to the number of incoming neutrons. The position of the neutron is determined by specially designed components. The YS detector is a $^{10}\text{BF}_3$ gas detector. Its pixel size is 10 mm x 10 mm, and it has 64 x 64 pixels. It can be moved in a 6 m long vacuumed tube between 1.3 m (closest position to the sample) and 5.4 m. Before the detector house, a Cd plate is placed, with the purpose of absorbing the high intensity direct neutron beam transmitted through the sample. The Cd plate is called “beam-stop”, and its size can be varied according to the size of the beam defined by the collimator.

The instrument uses also a mechanical velocity selector which allows to set wavelengths from ~ 4 Å to ~ 12 Å with a wavelength spread, $\Delta\lambda/\lambda$, of 0.20. The mechanical velocity selector (designed and built at BNC) select a monochromatic neutron beam from the cold neutron spectrum, by allowing neutrons of defined velocity to pass through, while absorbing others. It consists of a turbine with several disks whose windows form helical channels (Fig. 3.13).

Disks are coated with a strongly neutron-absorbing material, i.e. gadolinium-

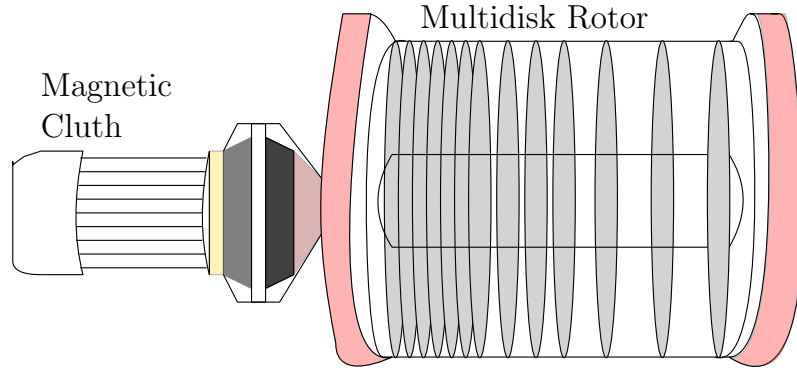


Figure 3.13: Velocity selector.

oxide. The rotation speed is variable between 700 rpm and 7000 rpm. By changing the rotation speed, the wavelength of neutrons can be varied from 3 Å to 25 Å. The relation between the rotation speed and the wavelength can be determined by measuring the time of flight of the neutrons using the following equation:

$$\lambda_n = \frac{ht_n}{m_n d_n}, \quad (3.29)$$

where:

- λ_n selected wavelenght of the neutrons
- t_n is the flight time
- $m_n = 1,6749 \times 10^{-27}$ Kg, mass of neutron
- $h = 6,625 \times 10^{-34}$ is the Planck constant
- d_n selector-detector distance

The wavelength spread can be tuned between 10 and 30% FWHM, by varying the rotor tilt angle (the angle between the beam and the selector axis).

YS allows the use of three different kind of specifically designed sample holders: a sample holder with a temperature regulator – from 15°C to 90°C - with 6 sample positions, a room temperature sample holder with 9 sample positions and a vertical sample changer, designed for samples to be measured under magnetic field. An electromagnet of max 1.8 T magnetic field is available. Larger (max. 0.5m diameter)

samples can be measured by removing the sample changer. Solid compact samples are placed into the sample holder without any preparation. For powder and liquid samples quartz cuvettes of various sizes (Fig. 3.14), or other holders made of low neutron absorbing and scattering material are used.



Figure 3.14: Quartz cuvettes.

3.4 SANS experiment

In order to reduce the incoherent contribution to the measured total scattering cross sections, the hydrogen-deuterium exchange for $-OH$ and $-NH$ groups was promoted by washing cycles in D_2O and subsequent lyophilisation. Generally, 1 g of CNS was suspended in 5 mL of D_2O and stirred for 1.5 h, then was frozen at $-80\text{ }^{\circ}C$ and freeze-dried until complete sublimation of solvent. We repeated this procedure for each sample 4 times. Hydrated samples were prepared by adding a suitable amount of D_2O to a weighed quantity the corresponding dry powder of CNS, in order to achieve the desired hydration level h (h = weight of water/weight of sponge). For each investigated sample, the highest water content was determined by the formation of a suspension, indicating that a further water uptake was not possible, and water went outside the pores of the material. In the case of CNS (0.2:1) sample, the hydration levels were chosen between $h = 0.8$ and $h = 5$. Regarding CNS (0.5:1), CNS (1:1), CNS (2:1) and CNS (2:1)-CA samples, higher values of hydration were possible, ranging from $h = 1.5$ to $h = 10$.

All spectra were recorded in the range of scattering wavevector modulus q from 0.006 to 0.4 Å⁻¹ using a 64 x 64 cm² (1 cm x 1 cm pixel size) BF₃ gas-type detector; the neutron beam was monochromatized by a mechanical velocity selector with a wavelength spread $\Delta\lambda/\lambda \cong 0.20$ [87, 88]. In order to have access to the whole range of q , we used three different configurations. In particular, the high- q region was obtained by setting the sample-detector (S-D) distance to 1 m and the incident neutron wavelength to ~ 4.4 Å. For the medium and low- q range the S-D distance was changed to 5.125 m, and the incident neutron wavelengths were ~ 4.4 Å and ~ 10.23 Å, respectively. The CNS sponges were prepared into quartz cuvettes that provided a 2 mm path length for the neutron beam, six samples per run. According to the estimated scattering intensity of each sample, the data collection time was chosen to collect an intensity integrated over the whole 2D detector of about 5×10^5 counts for the dry samples and about 2×10^6 counts for the hydrated ones, aimed at achieving optimal statistical accuracy for each data set, experimentally monitored. Measurement times varied from ~ 50 min to ~ 2 h. For a few samples, by selecting three different hydration levels for each CNS (low, medium, and high h values), experiments were repeated with fresh samples and at different times to test reproducibility. The error bars of the data points for all SANS plots are within the limits of the symbols. We azimuthally averaged the scattering intensities. Then, we corrected them for the sample transmission, detector efficiency and room background using standard procedures.

The experimental data reduction was performed by using the BerSANS software [89], which allowed us to take into account the incoherent scattering coming from hydrogens, the cadmium spectra for the detector pixels calibration, and the contribution of unwanted scattering and reflections coming from the empty cuvette. SANS data were transformed to absolute scale by comparing to a pre-calibrated light water sample. After a proper reduction, we analyzed and fitted the treated spectra by the SasView software (<http://www.sasview.org/>).

3.5 Fourier-Transform Infrared (FTIR) spectroscopy

Infrared (IR) absorption spectroscopy is a widely used method to determine dynamical, and indirectly also structural, features of molecules starting from their characteristic absorption of infrared radiation. In particular, IR spectrum is a molecular vibrational spectrum. When exposed to infrared radiation, molecules selectively absorb radiation at a specific frequency which causes a change of dipole moment of the molecules themselves. Consequently, the vibrational energy levels of sample molecules transfer from ground state to excited state. The frequency of the absorption peaks is determined by the vibrational energy gap, their number by the number of vibrational degrees of freedom of the molecule, their intensity by the change of dipole moment and the possibility of the transition of energy levels. In the last decades, several applications of IR spectroscopy have been realized thanks to the development of Fourier-transform infrared (FTIR) spectrometers, that replaced dispersive IR spectrometers because of their important advantages such as the high signal-to-noise ratio, the high accuracy in the determination of the wavenumber (the error is within $\pm 0.01 \text{ cm}^{-1}$ range), the short scan time required ($\sim 1 \text{ s}$), the extremely high resolution (up to 0.005 cm^{-1}), the wide range that can be scanned (approximately from 1000 cm^{-1} to 10 cm^{-1}), the strong reduction of the interference from stray light. Generally speaking, what is measured by a FTIR spectrometer is the amount of radiation transmitted by the specimen after the absorption process. This can be different according to the nature of the functional groups present, which is, in turn, related to the chemical composition of a given sample. In particular, a FTIR spectrometer allows to get IR spectra starting from an interferogram. The main component of a FTIR instrument is the Michelson interferometer ([Fig. 3.15](#)).

In a Michelson interferometer, light from the source strikes the beam splitter (BS), which consists of a glass plate with a partially reflective surface. The beam splitter allows 50% of the radiation to be reflected to the fixed mirror M1. The other 50% of the radiation is transmitted to the translatable mirror M2. After their reflection, the two beams return back towards the BS and recombine forming a single beam which travels towards the screen. At the screen, 50% of the intensity of each reflected beam is transmitted/reflected towards the screen for observation.

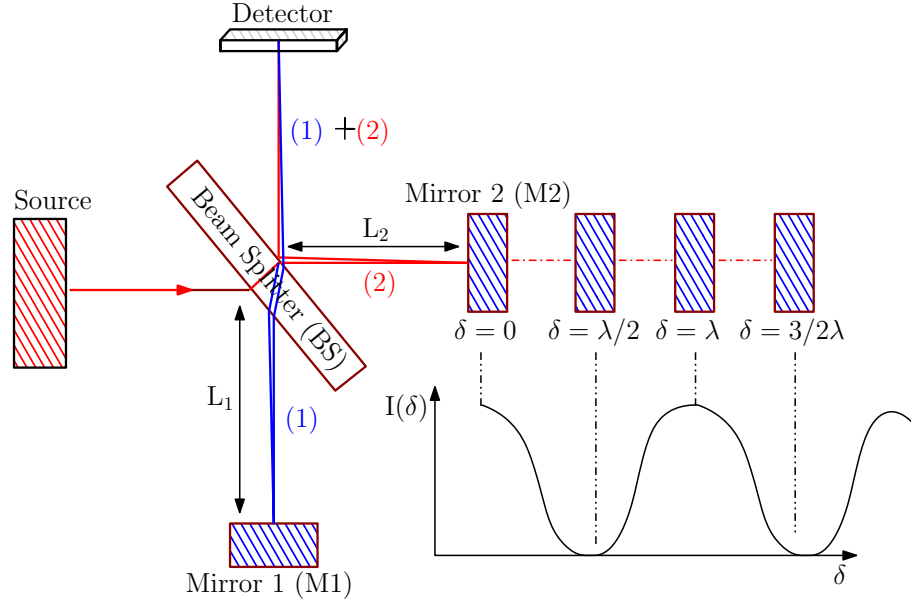


Figure 3.15: Michelson interferometer.

At the screen, the two beams overlap and constructive and destructive interference occurs depending on the relative phase shift between the two plane waves. The total phase shift between the two beams can be written as:

$$\phi = \phi^* + 2k(L_2 - L_1) = \phi^* + 2\pi x, \quad (3.30)$$

where the phase shift ϕ^* is due to the propagation through the glass of the beam splitter and the partial reflection at the semi-transparent surface. $k = 2\pi/\lambda$ is the wavenumber, being λ the incident wavelength, and $x = L_2 - L_1$, being L_1 and L_2 the BS-M1 and BS-M2 distances, respectively. Constructive interference will occur when $\phi = m2\pi$, with $m = 0, 1, 2, \dots$. Now, since L_2 changes continuously and L_1 is kept fixed, changes of constructive and destructive interference phenomena are generated at the detector, depending on the relative position of the movable mirror with respect to the fixed one. As a consequence, the intensity of the signal increases and decreases giving rise to a cosine wave. The plot is defined as an interferogram. When detecting the radiation of a broad band source rather than a single-wavelength source, a peak at the zero-path-difference (ZPD) position is found in the interferogram. At the other distance scanned, the signal decays quickly since the mirror moves back and forward.

3.5.1 Theoretical background

In this section, a general description developed by Volino (1978) for the principle of any spectroscopic experiment will be addressed. The aim of this mathematical formulation is to figure out the characteristic of the investigated material in terms of a coupling between a *probe* and a *reservoir*.

A common flow chart of a scattering experiment is displayed in Fig. 3.16.

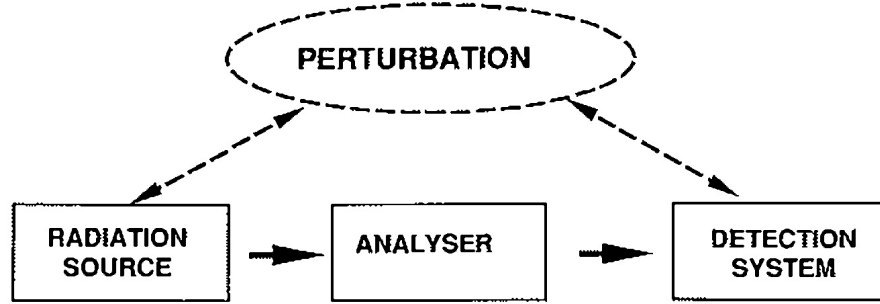


Figure 3.16: Flow chart of a general spectroscopic experiment.

Let's define the initial state of the probe P , characterized its Hamiltonian H_P , with $|m\rangle$. The investigated system (hereafter designated as the 'reservoir' and described by its appropriate Hamiltonian H_R) R , at thermal equilibrium T , can be found in any state $|m'\rangle$ with a probability given by the Boltzmann law:

$$P_{m'} = \frac{1}{Z_R} e^{(-\beta E_{m'})}, \quad (3.31)$$

with $Z_R = \sum_{m'} e^{-\beta E_{m'}}$ and $\beta = 1/k_B T$, where k_B is the Boltzmann constant.

Let us consider the total system S as the sum of P and R (probe + reservoir). Then, the corresponding initial and final eigenfunctions will be $|m\rangle|m'\rangle$ and $|n\rangle|n'\rangle$ (with $|n\rangle$ and $|n'\rangle$ final states of the probe and reservoir, respectively). The transition probability between these two states can be calculated with the *Fermi Golden rule* as:

$$W_{nn'mm'} = \frac{2\pi}{\hbar} |\langle n'|\langle n|H_c|m\rangle|m'\rangle|^2 \delta(E_m + E_{m'} - E_n - E_{n'}). \quad (3.32)$$

Here, $W_{nn'mm'}$ describes the probability per unit time that the total system composed of the probe and the reservoir changes from the initial state $|m\rangle|m'\rangle$ to the final state $|n\rangle|n'\rangle$, and H_c represents the Hamiltonian of interaction between the

probe and the reservoir. Eqn. 3.32 is true only in linear approximation, which means that $H_c \ll H_R$ and $H_c \ll H_P$ and also over long times.

Then, the change of the state of the probe can be written as:

$$W_{nm} = \sum_{m'n'} W_{nn'mm'} P_{m'} = \frac{1}{Z_R} \sum_{m'n'} W_{nn'mm'} e^{-\beta E_{m'}}. \quad (3.33)$$

The principle of any spectroscopic experiment is to measure a quantity which is proportional to W_{nm} as a function of either the final state $|n\rangle$ or the initial state $|m\rangle$ of P. In other words, we measure the response of the specimen to the perturbation caused by the probe.

If we define $\overline{H_c}$ as the mean value of the interaction Hamiltonian between the initial and final state of P:

$$\overline{H_c} = \langle n | H_c | m \rangle,$$

and considering $\hbar\omega = E_m - E_n$ and $\hbar\omega_{n'm'} = E_{n'} - E_{m'}$, Eqn. 3.33 can be rewritten as:

$$W_{nm} = \frac{2\pi}{\hbar^2} \sum_{n'm'} \frac{e^{-\beta E_{m'}}}{Z_R} |\langle n' | \overline{H_c} | m' \rangle|^2 \delta(\omega_{n'm'} - \omega). \quad (3.34)$$

Thus $\hbar\omega$ is defined as the energy gain of the probe, whilst $\hbar\omega_{n'm'}$ is the energy loss for the reservoir. Furthermore, the presence of a δ -function in Eqn. 3.34 ensures a non-vanishing transition probability when $\hbar\omega$ and $\hbar\omega_{n'm'}$ are equal.

It is possible to demonstrate how the transition probability W_{nm} can be calculated from $\overline{H_c}$ using the Heisenberg representation. Accordingly, we can write $\overline{H_c}(t)$ as:

$$\overline{H_c}(t) = e^{\left(\frac{-iH_R t}{\hbar}\right)} \overline{H_c} e^{\left(\frac{iH_R t}{\hbar}\right)}. \quad (3.35)$$

The notation $\overline{H_c}(t)$ holds for the Heisenberg representation of operator $\overline{H_c} = \overline{H_c}(0)$.

Let us define now the autocorrelation function $C_{\overline{H_c}\overline{H_c}}(t)$ as:

$$C_{\overline{H_c}\overline{H_c}}(t) = \langle \overline{H_c}^+(0) \overline{H_c}(t) \rangle, \quad (3.36)$$

which represents the quanta-mechanic expression for the self-correlation function of $\overline{H_c}$. The Fourier transform of Eqn. 3.36 gives us the spectral density $C_{\overline{H_c}\overline{H_c}}(\omega)$

which is related to the autocorrelation function $C_{\overline{H}_c \overline{H}_c}(t)$ by:

$$C_{\overline{H}_c \overline{H}_c}(\omega) = \frac{1}{2\pi} \int_{-\infty}^{+\infty} C_{\overline{H}_c \overline{H}_c}(t) e^{-i\omega t} dt. \quad (3.37)$$

This relation can be used, finally, to calculate the transition probability W_{nm} as:

$$W_{nm} = \frac{2\pi}{\hbar^2} C_{\overline{H}_c \overline{H}_c}(\omega). \quad (3.38)$$

If we are interested in the "inverse" ($m \rightarrow n$) transition probability we must change ω in Eqn. 3.38 with $-\omega$. The inverse probability is related to the direct transition W_{nm} through the detailed balance condition:

$$W_{mn} = e^{-\beta\hbar\omega} W_{nm}. \quad (3.39)$$

This last equation is known as Kubo-Ayant theorem. This theorem asserts that a transition probability between two eigenstates is proportional to the population of the initial level.

In summary, in a spectroscopic experiment we have to define the system R, the probe P and the interaction H_c between them. Then we have to compute its average value and its time correlation function in order to obtain the expression for the transition probability W_{nm} . The last step is to obtain a relation between this probability W_{nm} and an experimentally accessible quantity.

Classically, the electric and magnetic fields are described in terms of the oscillating vectors $\mathbf{E}(\mathbf{r})$ and $\mathbf{H}(\mathbf{r})$, respectively. When an electromagnetic wave strikes an ensemble of particles, it interacts with the electric charges of the material. According to this, it is possible to define a polarizability tensor $\boldsymbol{\alpha}(\mathbf{r})$ and a dipole moment $\boldsymbol{\mu}(\mathbf{r})$ per unit volume. If we assume to deal with a high-wavelength electromagnetic radiation, the Hamiltonian of interaction H_c can be written as:

$$H_c = - \int_V d\mathbf{r} [\mathbf{E}(\mathbf{r})\boldsymbol{\mu}(\mathbf{r}) + 1/2\mathbf{E}(\mathbf{r})\boldsymbol{\alpha}(\mathbf{r})\mathbf{E}(\mathbf{r}) + \text{superior order terms}]. \quad (3.40)$$

The first term of Eqn. 3.40 is related to the infrared and dielectric absorption. The second term describes the Raman and Rayleigh scattering and, finally, the other

superior order terms account magnetic interactions and iper-polarizability phenomena.

In the case of induced absorption/emission processes, the autocorrelation function of the mean value of \overline{H}_c between the initial and finale state of the probe can be written as:

$$C_{\overline{H}_c\overline{H}_c}^{\pm}(t) = \frac{2\pi\hbar\omega_0}{V} N_{k_0I} \left\langle \sum_{ij} (\boldsymbol{\epsilon}_i \boldsymbol{\mu}_i(t)) (\boldsymbol{\epsilon}_i \boldsymbol{\mu}_i(0)) e^{\pm i \mathbf{k}_0 [\mathbf{r}_i(t) - \mathbf{r}_j(0)]} \right\rangle. \quad (3.41)$$

In this case, we have assumed that the probe is made up of photons of momentum \mathbf{k}_0 and polarization $\boldsymbol{\epsilon}_i$. Here, N_{k_0I} is the number of photons and $\boldsymbol{\mu}_i$ is the dipole moment. Finally, the \pm sign takes into account the emission and absorption processes.

It is worth of note that in case of high wavelengths the term \mathbf{k}_0 can be neglected (being equal to $2\pi/\lambda_0$) as well as its variation over time. As a result, the correlation functions for both the absorption and emission will assume the same form:

$$C_{\overline{H}_c\overline{H}_c}(t) = \frac{2\pi\hbar\omega_0}{V} N_{k_0I} \left\langle \sum_{ij} (\boldsymbol{\epsilon}_i \boldsymbol{\mu}_i(t)) (\boldsymbol{\epsilon}_i \boldsymbol{\mu}_i(0)) \right\rangle. \quad (3.42)$$

In linear approximation, from the Kubo-Ayant theorem we can state that

$$W^{abs} > W^{emi}.$$

So we conclude that the induced phenomenon is the absorption, and the corresponding probability per unit of time is:

$$W^t = W^{abs} - W^{emi} = \frac{2\pi}{\hbar^2} [1 - e^{-\beta\hbar\omega_0}] C_{\overline{H}_c\overline{H}_c}(\omega_0). \quad (3.43)$$

We can now figure out a new correlation function by relating W^t to the absorbed power P_a during the experiment. The latter, can be considered as a correlation between fluctuations in the dipole moment components along the polarization direction. Being proportional to the spectral density of the dipole fluctuations we have:

$$C_{\mu\mu}(t) = \frac{1}{N} \left\langle \sum_{ij} (\boldsymbol{\epsilon}_i \boldsymbol{\mu}_i(t)) (\boldsymbol{\epsilon}_i \boldsymbol{\mu}_i(0)) \right\rangle. \quad (3.44)$$

This relation can be further simplified if we consider an isotropic medium. Accordingly, mediating ϵ_i over all possible orientations we get:

$$C_{\mu\mu}(t) = \frac{1}{N} \langle \sum_{ij} \boldsymbol{\mu}_i(0) \boldsymbol{\mu}_j(t) \rangle. \quad (3.45)$$

It is worth to remark that the electric dipole moment of a given molecule depends on how the electric charges are distributed around it. Such distribution changes if the molecule makes *vibrations*. In this case we can write:

$$\boldsymbol{\mu} = \boldsymbol{\mu}^0 + \sum_{\nu} \boldsymbol{\mu}^{\nu} q^{\nu}, \quad (3.46)$$

where $\boldsymbol{\mu}^0$ is the *permanent dipole moment* and $\boldsymbol{\mu}^{\nu}$ takes into account the dipole moment variations due to vibrations of the molecule (*derived dipole moment*). This last term can be written as:

$$\boldsymbol{\mu}^{\nu} = \left(\frac{\partial \boldsymbol{\mu}}{\partial q^{\nu}} \right)_{q^{\nu}=0}. \quad (3.47)$$

Here, ν is the vibrational state and q^{ν} the corresponding normal coordinate.

According to this procedure, it is possible to split the correlation function in two different contributions:

$$C_{00}(t) = \frac{1}{N} \langle \sum_{ij} \boldsymbol{\mu}_i^0(0) \boldsymbol{\mu}_j^0(t) \rangle. \quad (3.48)$$

$$C_{\nu\nu}(t) = \frac{1}{N} \langle \sum_{i,j,\nu,\nu'} \left(\boldsymbol{\mu}_i^{\nu}(0) \boldsymbol{\mu}_j^{\nu'}(t) \right) \left(\mathbf{q}_i^{\nu}(0) \mathbf{q}_j^{\nu'}(t) \right) \rangle. \quad (3.49)$$

Eqn. 3.48 is the correlation function for the dielectric absorption; whereas Eqn. 3.49 describes the correlation function for the infrared absorption in a isotropic medium. Typically, it is possible to simplify the correlation function for the IR absorption considering the following assumptions:

- Molecules in the sample are identical
- Vibrations and rotations are decoupled
- Vibrations among different and within the same molecule are decoupled

From these considerations it follows that:

$$\langle \mathbf{q}_i^\nu(0) \mathbf{q}_j^{\nu'}(t) \rangle = 0, \quad (3.50)$$

for $i \neq j$ and $\nu \neq \nu'$. Taking into account these assumptions we can rewrite Eqn. 3.49 as:

$$C_{\nu\nu}(t) = \frac{1}{N} \sum_{\nu} \langle (\boldsymbol{\mu}^\nu(0) \boldsymbol{\mu}^\nu(t)) \rangle \langle (\mathbf{q}^\nu(0) \mathbf{q}^\nu(t)) \rangle. \quad (3.51)$$

In the case of weakly damped vibrations:

$$\langle \mathbf{q}_i^\nu(0) \mathbf{q}_j^\nu(t) \rangle = (q^\nu)^2 e^{(-i\Omega_\nu t)} G(t). \quad (3.52)$$

This relation states that each oscillation mode can be seen as a damped harmonic oscillator with frequency Ω_ν , where q^ν indicates the vibration amplitude and $G(t)$ a damping term slowly variable. If we consider now the rotational part:

$$\langle \boldsymbol{\mu}^\nu(0) \boldsymbol{\mu}^\nu(t) \rangle = (\boldsymbol{\mu}^\nu)^2 \langle \cos\theta^\nu(t) \rangle = (\boldsymbol{\mu}^\nu)^2 F_{1\nu}(t), \quad (3.53)$$

with $\theta^\nu(t)$ the angle subtended by the same dipole moment at different times and $F_{1\nu}(t) = \langle \cos\theta^\nu(t) \rangle$ is the *single molecule correlation function*. By replacing all these relations in Eqn. 3.51 we obtain:

$$C_{\nu\nu}(t) = \sum_{\nu} (\mu^\nu q^\nu)^2 e^{(-i\Omega_\nu t)} G_\nu(t) F_{1\nu}(t). \quad (3.54)$$

By applying the Fourier transform of Eqn. 3.54 we obtain:

$$C_{\nu\nu}(\omega) = \sum_{\nu} (\mu^\nu q^\nu)^2 G_\nu(\omega + \Omega_\nu) \otimes F_{1\nu}(\omega + \Omega_\nu). \quad (3.55)$$

The infrared absorption spectrum is therefore made up of a series of absorption lines centred around the vibrational frequencies Ω_ν . Each line can be considered as a convolution of a rotational and vibrational contribution. Since Ω_ν generally fall within the infrared region of the electromagnetic spectrum, we usually refer to this phenomenon as *infrared absorption*.

Generally, the separation of these two terms (rotations and vibrations) in the absorption spectrum is a challenging task. However, it is well known that the vibra-

tional contribution becomes predominant with respect to the rotational one as the dimension of the molecule increases. A general approach to overcome this problem consists in comparing the IR results with those obtained with other techniques, such as the Raman spectroscopy.

3.5.2 Harmonic oscillator model

The simplest theoretical model which is used to describe the IR absorption process consists of a bi-atomic molecule acting as a harmonic oscillator. For this system it is possible to apply the Hooke law if we assume to neglect anharmonic effects. The Schrödinger equation of an harmonic oscillator can be written as:

$$-\frac{\hbar^2}{2\mu} \frac{d^2\Psi}{dx^2} + \frac{1}{2}kx^2\Psi = E\Psi, \quad (3.56)$$

where μ is the reduced mass and k is the bond strength. The resolution of [Eqn. 3.56](#) provides the vibrational levels allowed for the molecule, having energy:

$$E = \left(\nu + \frac{1}{2}\right) \hbar\omega. \quad (3.57)$$

Here, ν is the *vibrational quantum number* and ω is the vibrational frequency given by:

$$\omega = \sqrt{\frac{k}{\mu}}. \quad (3.58)$$

From [Eqn. 3.58](#) several considerations can be drawn: (i) the greater the binding force, the greater will be the vibration frequency (ii) the heavier the molecule, the lower the frequency of vibration.

An infrared radiation can induce a vibrational transition only if it causes a variation in the molecular dipole moment. However, not all the vibrations are followed by a change in the dipole moment. To these kind of vibrations we generally refer as *IR inactive*. Conversely, if vibrations lead to dipole moment variations are called *IR active*. Selection rules state that absorption and emission occur according to $\Delta\nu = \pm 1$. However, it is also possible to observe also transitions in the absorption spectrum which violate this condition, known as "*overtones*".

3.5.3 Vibrational normal modes

It is well known that a molecule composed of N atoms has $3N$ *degrees of freedom*. In non-linear molecules, the total number of vibrational modes are $3N-6$; being three both the translation and rotation modes. Whereas, for linear molecules such vibrational modes are $3N-5$.

Vibrations can be classified in two different categories: *stretching vibrations* and *bending vibrations* (Fig. 3.17). Stretching modes consist in periodical variations of the inter-atomic bond length and can be *symmetric* ν_s (if atoms bounce back and forth simultaneously) and *anti-symmetric* ν_a (if atoms oscillate out-of-phase). In *bending vibrations* the position of atoms changes relative to the bond axis.

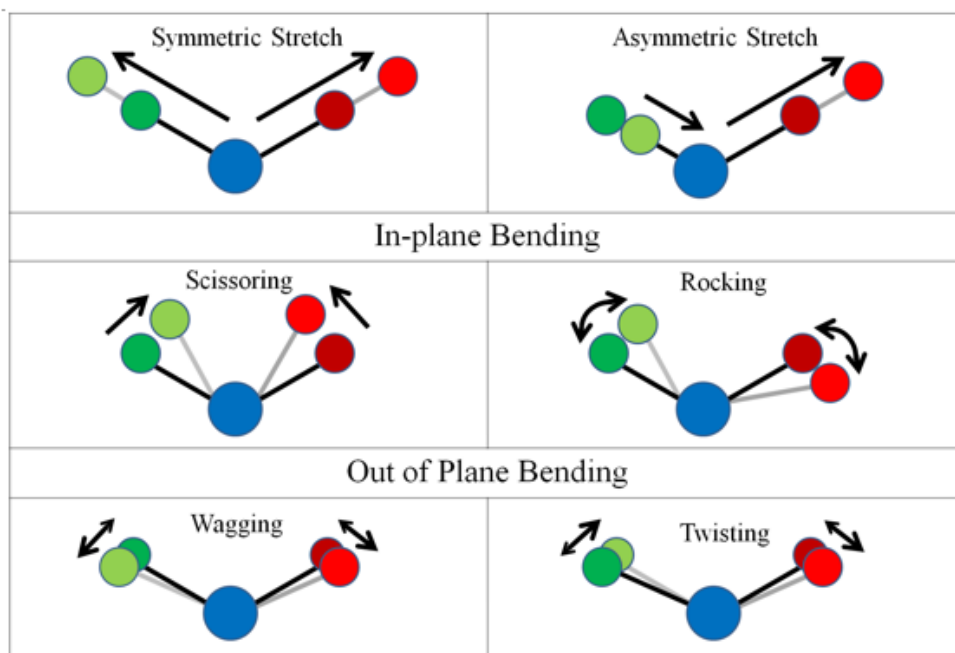


Figure 3.17: Schematic representation of stretching and bending vibrations.

Molecules can experience a symmetric or an anti-symmetric bending vibration along the plane on which lies the bond angle or out of it. Symmetric and anti-symmetric in-plane vibrations are known as *scissoring* (δ) and *rocking* (ρ), respectively. Symmetric and anti-symmetric out-of-plane vibrations, instead, are called *twisting* (τ) and *wagging* (w).

Being the infrared range of the electromagnetic spectrum extremely large, it is usually divided in three different spectral regions: Near-Infrared (NIR, 12.000-

4000 cm⁻¹), Mid-Infrared (MIR, 4000-400 cm⁻¹) and Far-Infrared range (FIR, <400 cm⁻¹).

In the NIR range falls all the absorption bands produced by electronic transitions, similarly to what happen in the case of visible light or UV. In MIR, we can found absorptions caused by fundamental vibrational levels. Finally, in FIR all the rotational modes of the system can be detected.

Between 3800 and 1300 cm⁻¹, know as *functional groups region*, we can recognise all the absorption bands which came from stretching modes. Here, X-H bonds and C-Y multiple bonds vibrations can be found. Between 1300 and 400 cm⁻¹, known as *fingerprint* region, falls vibrations of the whole molecule, also known as "skeleton" vibrations. Finally, the 400 - 200 cm⁻¹ range includes heavy atom bonds and vibrations of functional groups without hydrogens.

3.5.4 IR absorption band features

When a monochromatic light of intensity I_0 passes through a layer of thickness d , a portion of it will be absorbed by the material while the remaining will be transmitted with a residual intensity:

$$I = I_0 e^{-\frac{2k\omega d}{c}} = I_0 e^{-\frac{4\pi k d}{\lambda}} = I_0 e^{-\alpha d}. \quad (3.59)$$

This equation, know as *Lambert-Beer* law, relates the amount of absorbed radiation with the material properties, concentration and thickness. In fact, α is the *absorption coefficient*, d the thickness crossed by the radiation, λ the wavelength, ω the frequency, k the imaginary part of the refractive index (known also as extinction coefficient) and c the speed of light.

The ratio of transmitted intensity, I , to incident intensity, I_0 , at a given frequency is called the *transmittance*, T , of the sample:

$$T = \frac{I}{I_0} = e^{-\alpha d}. \quad (3.60)$$

We can define now the *Absorbance* A as the logarithm of the inverse of T :

$$A = \log_{10} \frac{1}{T} = \log_{10} \frac{I_0}{I} = \alpha d \log_{10} e = \frac{\alpha d}{2.303}. \quad (3.61)$$

If the sample is dispersed in solution, we can define A as a function of its molar concentration c as:

$$A = \epsilon(\tilde{\nu})cd, \quad (3.62)$$

where ϵ is the *molar absorption coefficient* (sometimes still called the “extinction coefficient”). The maximum value of $\epsilon(\tilde{\nu})$ gives us an indication of the transition intensity. However, the absorption band spreads across a range of wavenumbers, so a single wavenumber may not reflect the true intensity of the transition. For this reason we usually deal with an integrated absorption coefficient, A , which is the sum of the absorption coefficients over the entire band, and corresponds to the area under the plot of molar absorption coefficient as a function of wavenumbers:

$$A = \int \epsilon(\tilde{\nu})d\tilde{\nu}. \quad (3.63)$$

A graphical representation of Eqn. 3.63 is displayed in Fig. 3.18.

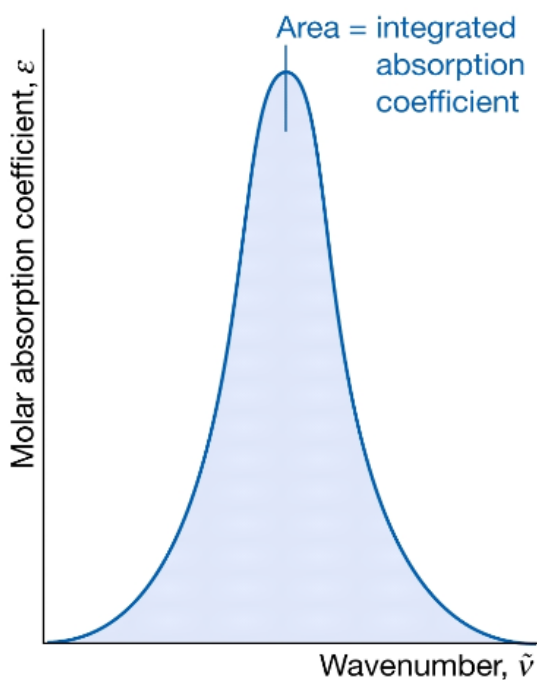


Figure 3.18: Molar absorption coefficient $\epsilon(\tilde{\nu})$ as a function of wavenumbers ν .

Spectral line formation, both in absorption or emission, strictly depends on quantum phenomena which involve the i and j states account for the low (i) and high (j) energy levels. Generally, three kinds of transitions can occur between these two

eigenstates: spontaneous and stimulated *emission*, and *absorption*.

Concerning the transition between the i and j energy levels we can distinguish two types of excitations: (i) *radioactive* excitation, in which a photon is absorbed by the electron and as a result of it "jumps" from i to j . (ii) *Collisional* excitation, if the system is pumped by an external energy source in such a way to exceed the energy gap $h\nu$, then transition from i to j may occur.

If the system is conducted in a non-equilibrium state (the j state, in this case, being at higher energy content with respect to i), the electron will eventually experience a decay from the upper quantum state j to the lower one i through three different processes.

- Collisional de-excitation
- Stimulated de-excitation
- Spontaneous de-excitation

In the stimulated absorption, electromagnetic field oscillations at transition frequency cause transitions between different states. Let's define w the *rate of change* that a molecule passes from its initial state to one of higher energy (also know as *transition rate*):

$$w = B\rho, \quad (3.64)$$

with B equal to the stimulated Einstein coefficient and ρ the energy density of the radiation. The transition rate w multiplied by the number of molecules N in the low-energy state give us the *total absorption rate* W :

$$W = Nw. \quad (3.65)$$

It is worth of note that the molecule may also experiences a de-excitation process, generating a new photon of frequency ν . Accordingly, the *stimulated emission rate* w' can be written as:

$$w' = B'\rho, \quad (3.66)$$

with B' equal to the stimulated emission coefficient. For spontaneous emission, being always a decay process as the previous one, the total transition rate is given by:

$$w' = A + B'\rho, \quad (3.67)$$

where A represents the Einstein coefficient for the spontaneous emission.

Hence, the overall emission rate assumes the form:

$$w' = (A + B'\rho)N', \quad (3.68)$$

with N' equal to the population of the upper energy level. Furthermore, the absorption and emission coefficient are equal. This means that if both the lower and upper energy level share exactly the same population, the two corresponding transition rates will be equal and no absorption occurs.

Considering that the spontaneous emission is a function of frequency, for low frequency values (typical of roto-vibrational transitions) it can be neglected and the total absorption can hence be written as a function of the population difference between the energy states involved:

$$W_t = (N - N')B\rho. \quad (3.69)$$

According to these equations, some considerations can be made: (i) since the first electronic excited state is generally located 10^4 cm^{-1} above the fundamental state, at ambient temperature it is always empty. Consequently, the electronic spectrum is usually composed of transitions which come from the lowest energy level. This is similar for vibrations, being the fundamental and the first energy state separated by $500 - 4000 \text{ cm}^{-1}$. This consideration cannot be applied to rotations, because even at ambient temperature most of the rotational excited states are populated (separation of $1 - 10 \text{ cm}^{-1}$). Hence, rotational transition may be generated from a large number of initial states and not only from the fundamental one.

Finally, there are several factors which affect the band width in a IR absorption spectrum. The first is the *Natural line broadening*. This type of spectral line broadening arises from the spontaneous decay rate. If we consider a bunch of atoms, their lifetimes are affected by the uncertainty in their energy states from quantum mechanics:

$$\Delta E \Delta t \sim \hbar.$$

A photon in a certain energy state will therefore have a range of possible frequencies

when it decays to a lower state:

$$\Delta\nu \sim \frac{\Delta E}{h} \sim \frac{1}{2\pi\Delta t}.$$

The line profile function due to natural broadening is the Lorentzian Profile. A typical lifetime for an atomic energy state is 10^{-8} seconds, which corresponds to a natural line width of 6.6×10^{-8} eV. However, this contribution is usually very small compared with other causes of broadening.

The second source of broadening comes from the *Doppler effect*. It occurs when the radiating atoms have a movement relative to the observer. The random atomic movement of the atoms is directly related to the temperature, which is why this broadening mechanism is called also *thermal*. In particular, if a moving source emits radiations at a frequency ν , depending on whether get away or closer with respect to the observer, we can calculate the variation of frequency as:

$$\nu' = \frac{\nu}{1 \pm \frac{v}{c}}, \quad (3.70)$$

where the $+$ and $-$ signs take into account the relative movement of the source. The line profile function due to the Doppler broadening is the Gaussian profile.

The last phenomenon that induces broadening of spectral lines is the collisions between excited atoms. We have to consider two types of collisions: (i) Lorentz collisions (between different atoms) and (ii) Holtsmark collisions (between atoms of the same type). For electrically neutral particles we have:

$$\Delta\nu_{coll}(P, T) = \Delta\nu_{coll}(P_0, T_0) \frac{P}{P_0} \sqrt{\frac{T_0}{T}}. \quad (3.71)$$

Collisional broadening $\Delta\nu_{coll}(P, T)$ depends on the relative pressure (P respect to P_0) and temperature (T respect to T_0) of the gas; with P_0 and T_0 equal to the ambient pressure and temperature. In particular if both T and P increase we shall assist to a strong broadening. It is worth noting that in this case, the spectral line profile is not Gaussian but Lorentzian, characterized by a narrower spike and longer wings. In the context of high pressure and high temperatures, the phenomenon of resonant self-absorption can also occur. This phenomenon consists in the auto-absorption of the emitted radiation by colder external gas layers.

3.6 BOMEM DA8 spectrometer

FTIR measurements reported here were carried out in the $400 - 4000 \text{ cm}^{-1}$ range using a Bomem DA8 spectrometer (Fig. 3.19) equipped with a Globar lamp source, a potassium bromide (KBr) beam-splitter (BS) and a deuterated triglycine sulfate (DTGS)/MIR detector.



Figure 3.19: Bomem DA8 spectrometer.

The instrument is basically made up of three different main sections: the upper one containing the source and beam-splitter compartment, the middle section with the beam switching compartment, the sample compartment and the detector modules, and finally the lower part containing the vacuum leads, the data processing and control electronics and the power supplies. As sources, the DA8 spectrometer is equipped with a Hg lamp ($5 - 200 \text{ cm}^{-1}$), a Globar (SiC, $200 - 10.000 \text{ cm}^{-1}$) and a Quartz lamp ($2000 - 25.000 \text{ cm}^{-1}$). Concerning the beamsplitters, we can find a $25 \mu\text{m}$ Mylar film ($10 - 125 \text{ cm}^{-1}$), a Hypersplitter ($40 - 700 \text{ cm}^{-1}$), a KBr ($500 - 5000 \text{ cm}^{-1}$) BS or a Quartz BS ($4000 - 25000 \text{ cm}^{-1}$). As already mentioned, for the purpose of this thesis a KBr BS was used. It has a diameter of 10 cm, and it is coated with a protective film of Ge or Sb_2S_3 . It is also hygroscopic, and therefore, despite the coating, it must be kept in a dry and moisture-free environment.

Close to the interferometer there is a 45° -tilted mirror (*output beam selection mirror*) that can be rotated thanks a software-controlled motor.

This allows to focus the beam towards one of the five output ports of the instrument (see Fig. 3.20).

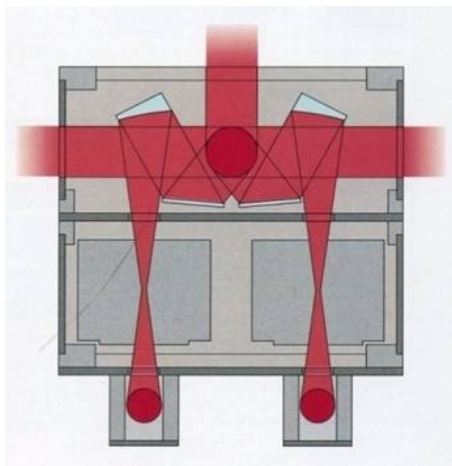


Figure 3.20: The five output ports of the BOMEM DA8 spectrometer.

Two of them are for the two detectors (one for MIR and the other for FIR) installed on the instruments (frontal exits); whereas the other two are located laterally to the sample compartment in a symmetrical position, and the last one is placed at the back of the instrument. For the frontal ports (*right sample position* and *left sample position*), the beam is directed, thanks to a *flat mirror*, towards one of the two paraboloid mirrors which focuses the beam on the sample (see Fig. 3.21). The outgoing radiation, now partially absorbed by the sample, is collected by the other paraboloid mirror (*detector focusing mirror*), which is used to focus the beam on the detector.

The DA8 spectrometer can operate at six different resolutions: 4, 2, 1, 0.5, 0.1 and 0.40 cm^{-1} . Furthermore, it is possible to set the velocity of the movable mirror of the interferometer between 16 values from 0.01 and 4 cm/s. However, it must be compatible with the response times of the detector used.

Finally, the dedicated software allows to select also a pressure threshold (eight different values between 0.1 and 50 *torr*) and set a *gain* of 1, 4, 16 or 64. Concerning the data acquisition and processing DA8 uses the GRAMS software.

For the purpose of this work, our measurements were performed exploiting a particular geometry known as *Attenuated Total Reflectance* (ATR). The internal reflection and the concept of evanescent wave, which represent the main features of

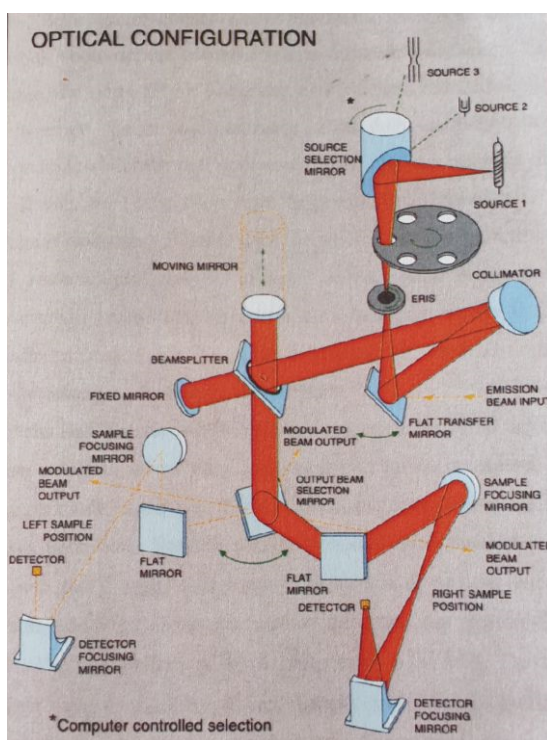


Figure 3.21: Internal optical configuration of the BOMEM DA8 spectrometer.

ATR spectroscopy, was firstly described by ISAAC NEWTON. Generally, the ATR technique is based on the *total reflection principle* occurring on the interface between materials having different refractive index n ; and it is extremely helpful in those case when opaque samples, or organic materials, must be characterized. The procedure described here is for single reflection ATR.

In a common FTIR spectrometer, the IR beam coming from the interferometer travels through a series of lenses and mirrors of the ATR unit, which is placed inside the sample compartment (Fig. 3.22). Then, it goes into a non-absorbing crystal (ATR crystal) placed in contact with the investigated material, in order to perform an internal reflection at the back of the crystal itself. In fact, according to the Snell law (see Fig. 3.23):

$$n_1 \sin \theta_1 = n_2 \sin \theta_2, \quad (3.72)$$

when an electromagnetic wave travels from a high refractive index n_1 to a low refractive index n_2 medium, we can define an angle know as *critical angle*:

$$\theta_{crit} = \arcsin\left(\frac{n_2}{n_1}\right),$$

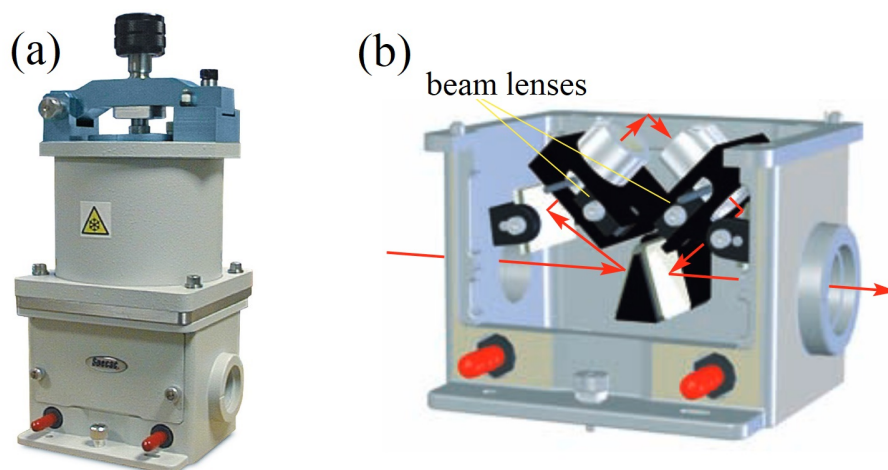


Figure 3.22: (a) ATR unit and (b) internal section.

such that if $\theta_1 > \theta_{crit}$ no refracted wave will occur, and the incident light undergoes a total reflection by the interface.

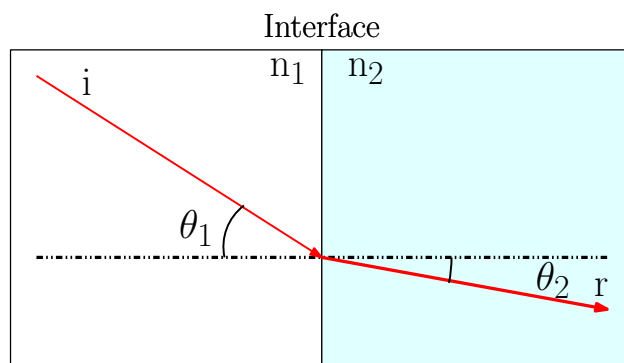


Figure 3.23: Representation of a propagating wave from a high refractive index material n_1 towards a low refractive index material n_2 . i and r are representative of the incident and refracted wave; whereas θ_1 and θ_2 of the incident and refracted angle, respectively.

As a result of this, we observe the formation of an *evanescent wave* that shows an exponential decay within the medium at lower refractive index (n_2). Some of the energy of the evanescent wave is absorbed by the sample and the reflected radiation is returned to the detector. This phenomenon is displayed in the following representation of a single reflection ATR (Fig. 3.24).

This evanescent wave penetrates into the investigated sample for microns, with the exact value being determined by the wavelength of light, the angle of incidence and the indices of refraction for the ATR crystal and the medium being probed.

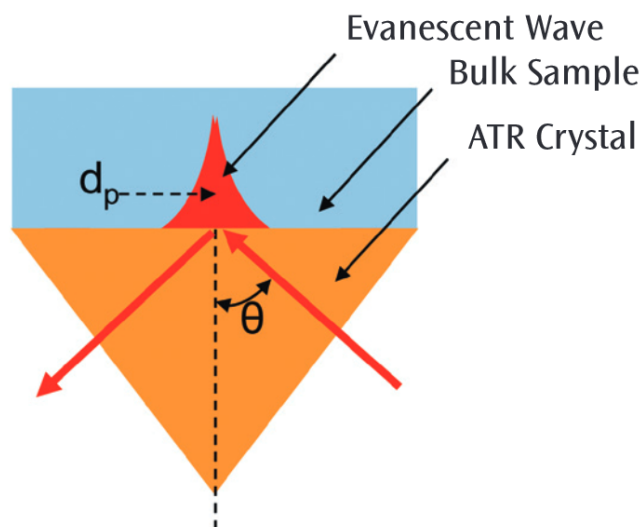


Figure 3.24: Penetration of the evanescent wave into the sample.

Typically, it propagates 2-15 μm beyond the surface and for this reason an intimate contact of the ATR crystal with the sample is essential.

As previously stated, in order to assist to internal reflection, some special material properties are required. In particular, for the evanescent wave to occur, one of the two media (crystal or sample) must have a very low refractive index with respect to the other one. In our case, a diamond ATR crystal (there are also zinc sulphide (ZnS), zinc selenide (ZnSe) and germanium ATR crystals) was used ($n = 2.41$ at 1000 cm^{-1}). Diamond is a valuable material for a wide range of samples, because it is resistant to scratching and abrasion and can tolerate a wide pH range as well as strong oxidants and reductants. Finally, it is worth mention that in case of multiple reflection ATR (see Fig. 3.25), the path length of the sampling surface can be calculated as the product of the number of reflections and penetration depth d_p (which will be defined further in the text). This produces more intense spectra and hence it is useful in case of weak absorbers; while the single bounce-ATR is preferred in those case in which strong absorbent materials must be analyzed.

Since the materials investigated in this thesis posses a water component, the use of an ATR unit is of extreme advantage. In fact, according to the Lambert-Beer law (see Eqn. 3.59 and 3.62), the IR absorption associated to each component inside the sample will be strongly dependent on its concentration.

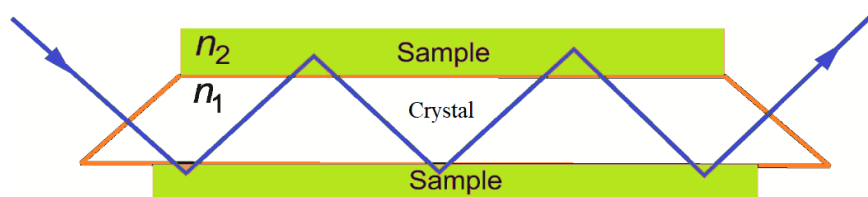


Figure 3.25: Multiple internal reflection cell.

Because of the high molar concentration of water (and, therefore, an extremely large molar absorptivity), the fundamental O-H stretching mode centred at $\sim 3400 \text{ cm}^{-1}$ makes IR transmission measurements difficult to carry out due to well-documented saturation effects [90–93].

The ATR unit allows to get reliable FTIR spectra of water-based materials in the mid-infrared region, because of the small penetration depth d_p of the evanescent wave. Technically, d_p is defined as the distance required for the electric field amplitude to fall to e^{-1} of its value at the surface, and can be written as:

$$d_p = \frac{\lambda}{2\pi n_1 \sqrt{(\sin^2 \theta - n_{21}^2)}}, \quad (3.73)$$

with θ , n_1 and n_{21} the incident angle, the refractive index of the ATR crystal and the ratio of the refractive indices of the sample and probe, respectively. The dependence of the penetration depth on these parameters provides the opportunity to choose whether one wants to investigate the surface or the bulk of the sample. The larger the incident angle and the higher the refractive index of the internal reflecting element is, the lower the penetration depth, thus only the surface is investigated. Furthermore, the penetration depth d_p depends also on the wavelength λ of the beam, which means that an increase of λ leads to an increase of the penetration depth and therefore of the intensity. However, it should be pointed out that the wavelength dependency causes small distortions in the resulting spectra but it is always taken into account in all commercial BOMEM software.

Finally, it is worth of note that ATR measurements could cause some variations in the band shape due to the *anomalous dispersion* (AD) effect. Basically, according to optics laws, "normal" light dispersion occurs when the refractive index n increases

as the wavelength λ decreases (like in prisms)

$$dn/d\lambda < 0. \quad (3.74)$$

AD is achieved when the refractive index increases with increasing the wavelength λ (Fig. 3.26), as opposed to the previous case.

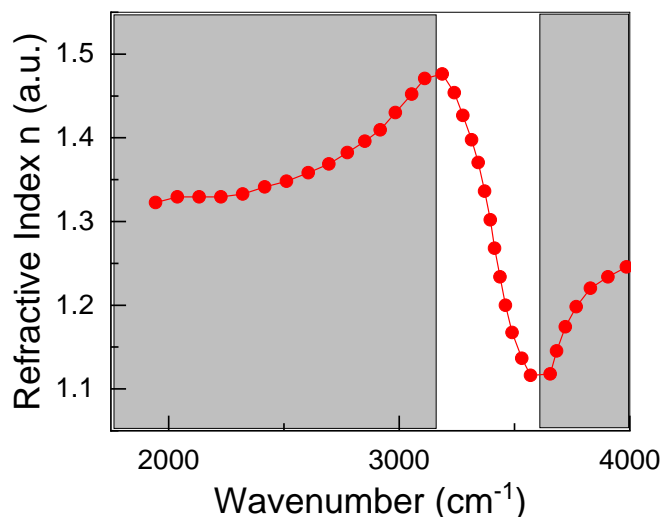


Figure 3.26: Behaviour of the refractive index n as a function of the wavenumber. Grey areas display normal dispersion; whereas the white area shows anomalous dispersion.

As a result of this, we can observe variations in the intensity and band positioning (generally red-shifted down to $\sim 70 \text{ cm}^{-1}$) of the FTIR-ATR peaks, although no new bands or peaks will be formed.

3.7 FTIR experiment

FTIR-ATR absorption spectra were recorded, as already mentioned, using a Bomem DA8 Fourier transform spectrometer, operating with a Globar source, in combination with a KBr beamsplitter and a thermoelectrically cooled deuterated triglycine sulphate (DTGS) detector. The samples of sponge were contained in Golden Gate diamond ATR system, just based on the Attenuated Total Reflectance (ATR) technique. The spectra were recorded with a resolution of 4 cm^{-1} , automatically adding 100 repetitive scans in order to obtain a good signal-to-noise ratio and highly reproducible spectra. All the measurements were performed in a dry atmosphere. To

check a possible unwanted effect induced by wetting and/or drying phenomena when the sample holder was filled with dry nitrogen, IR spectra in presence and absence of air were compared without showing any significant difference. All the spectra were normalized for taking into account the effective number of absorbers. No smoothing was done, and spectroscopic manipulations such as baseline adjustment and normalization were performed using the Spectracalc software package GRAMS (Galactic Industries, Salem, NH, USA). The analysis of the 3000–3800 cm^{-1} region, that required a band decomposition procedure, was undertaken using the curve fitting routine provided in the PeakFit 4.0 software package.

Measurements were carried out, as a function of temperature and hydration level h , on bPEI/TOUS-CNFs sponges at three different weight fractions, namely CNS (0.2:1), CNS (1:1) and CNS (2:1). The hydrated samples were prepared by adding a suitable amount of D_2O and H_2O to a weighed quantity the corresponding dry powder of CNS, in order to achieve the desired hydration level h (h = weight of water/weight of sponge). The lowest hydration level for each sample was $h = 0.4$; whereas the highest was $h = 8$ for CNS (0.2:1) and $h = 10$ for CNS (1:1) and CNS (2:1). For each hydration level a temperature scan was carried out between 250 K and 340 K (with a 10 K-degree step) through a 4000 SeriesTM Stability Temperature Controller (Fig. 3.27).

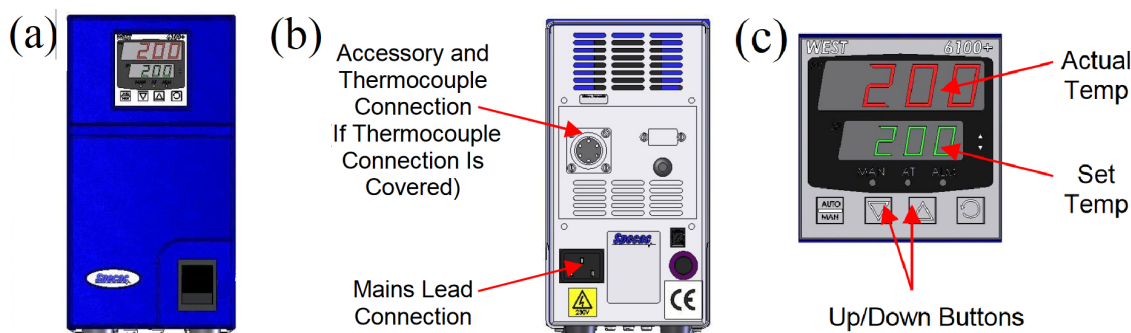


Figure 3.27: (a) frontal and (b) back view of the 4000 SeriesTM Stability Temperature Controller. (c) Monitor for the temperature set-up.

Chapter 4

SANS analysis on bPEI/TOUS-CNFs sponges

In Fig. 4.1 we display, as example, the 2D scattering profiles of CNS (2:1) sample, in the dry state and at different hydration levels, measured at a S-D distance of 5.125 m and using an incident wavelength of 4.4 Å.

The observed profiles are isotropic for all the investigated samples in the entire q -range explored in the present experiment, suggesting the absence of privileged orientations of the bPEI and nano-cellulose chains in real space. In other words, a random conformation of both the network-forming components, both in the dry and in the hydrated state, is observed. Taking into account the experimental method used for the synthesis of the investigated sponges, a random conformation of the bPEI/TOUS-CNFs chains was in a way expected. More precisely, the polymer network is initially due to the freezing of the solution where TOUS-CNFs are randomly dispersed. This approach implies the formation of ice crystals in the microscopic spatial domain and the freezing of the structure with a random distribution of fibers. After the freeze-drying process, the removal of water generates micro-sized pores, with the consequent formation of a cellulose-based porous material which maintains the random chains conformation. In addition, the grinding of the sponge into smaller particles and the occurrence that the scattering is done on powders allows us to expect an isotropic profile. The obtained 2D scattering profiles, then, experimentally confirm what expected.

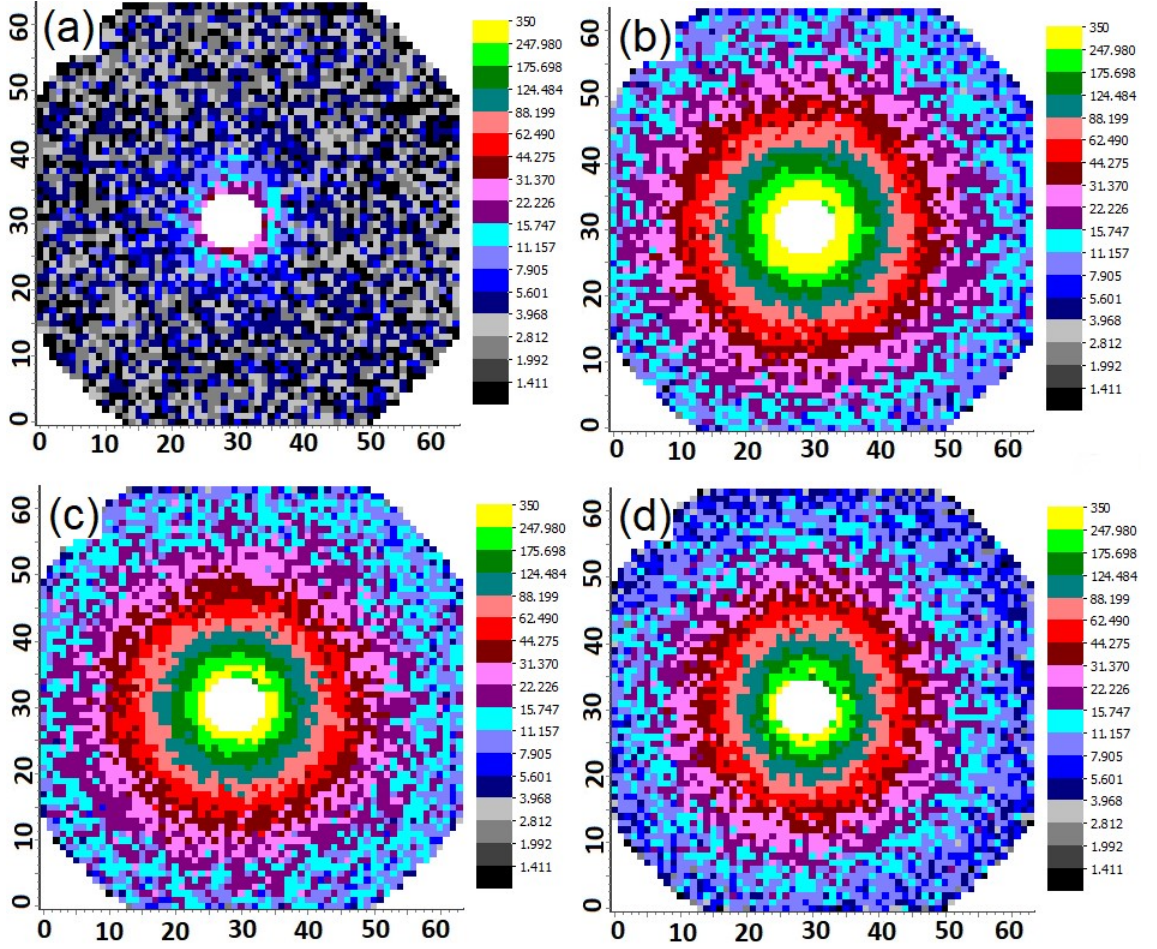


Figure 4.1: 2D scattering profiles of CNS (2:1) sample, in the dry state (a), and hydrated at $h = 2$ (b), $h = 4$ (c), and $h = 10$ (d). The brightness represents the logarithm of the total number of neutrons counted on the detector arbitrary scale, not corrected for the background or the contribution of the sample cell. Different colors have been used in order to show contours of constant neutron counts. Note that a beam stop is used to prevent detector damage due to the unscattered beam, resulting in a black spots centered at $q = 0$. Here a white mask was applied in order to eliminate this contribution in the data treatment.

Furthermore, a variation in the pattern is observed passing from the dry sample to the one hydrated at $h = 10$, revealing structural variations induced by the water content.

Fig. 4.2 displays the neutron scattering curves $I(q)$ vs. q of CNS (0.2:1), CNS (0.5:1), CNS (1:1) and CNS (2:1) sponges, dry and swollen from $h = 0.8$ to $h = 10$, azimuthally averaged from the reduced 2D spectra.

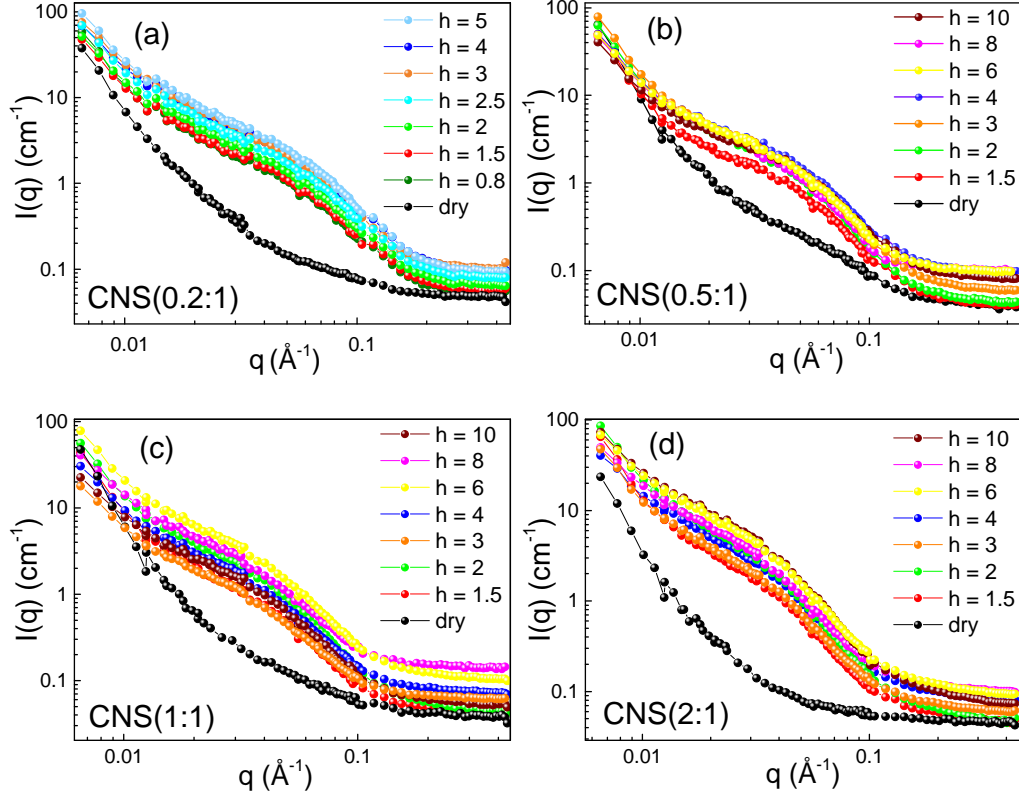


Figure 4.2: Scattering intensity as a function of q for CNS (0.2:1) (a), CNS (0.5:1) (b), CNS (1:1) (c), and CNS (2:1) (d) sponges, in the dry state and swollen at different hydration values h .

A first important consideration can be made by comparing the scattering profiles of the dry samples with those of the hydrated ones, regardless of the content of bPEI. In fact, for the latter, a double curvature is well evident. More precisely, we observe an upturn at low q values, below 0.02 \AA^{-1} , followed by a broad shoulder in the medium q -range, between 0.02 and 0.1 \AA^{-1} , and a horizontal plateau above 0.1 \AA^{-1} .

This trend is indicative of significant structural changes induced by the hydration process, which leads the chains forming the network to reorganize, generating, at two different length scales, inhomogeneities in the density of the nanofibers caused by the presence of water molecules.

In particular, the low- q upturn can be associated to a spatial distortion of the order of hundreds of nanometres. On the other side, the high- q feature is due to a variation, upon hydration, in the local structure ($\sim 10 - 100 \text{ \AA}$) of cross-links points between different fibers. It is worth remarking that if, on one side, the low- q upturn was in a way expected due to the presence, for such systems, of inhomogeneities at micro-scale level already experimentally observed [23], on the other side, the observed high- q feature can be considered as a first evidence of the existence of nanoscopic structural features, for our samples.

Furthermore, as can be seen from an inspection of Fig. 4.3, a clear evolution of the spectra can be also detected as a function of the chemical composition of the sponges in terms of weight fraction between the two components, i.e. bPEI and TOUS-CNFs. In particular, the broad shoulder in the medium q -range shifts towards high q values with a decrease of the bPEI:TOUS-CNFs weight fraction.

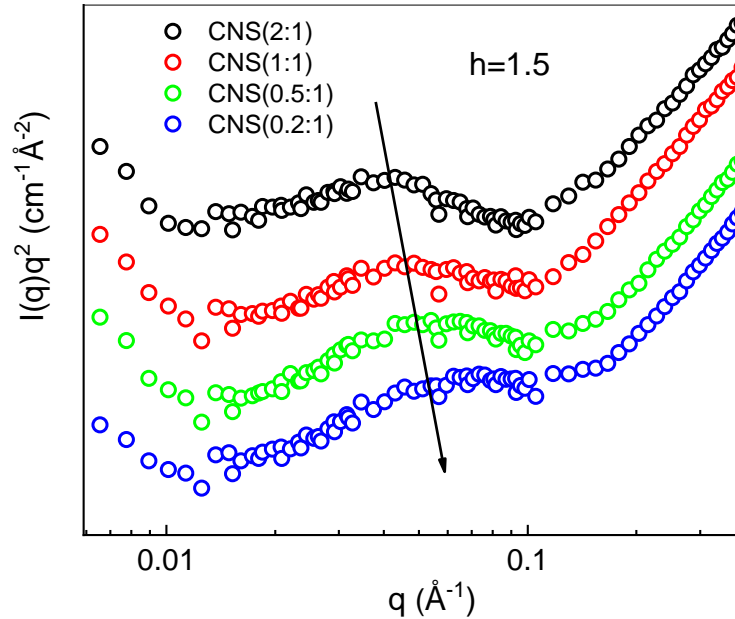


Figure 4.3: $I(q)q^2$ vs. q plot for CNS samples at different weight fraction between cross-linker and TOUS-CNFs ranging from 0.2:1 (blue circles) to 2:1 (black circles), at $h = 1.5$ as example. The arrow indicates the decrease of the weight fraction. In order to highlight the q -shift of the broad shoulder, the scattering curves were properly vertically translated for a better visualization.

This observed shift, which implies a decrease of a typical length scale in the range of several tens of \AA , can be related to a reduction of the dimensions of the clusters characterizing the polymer network. This can be explained by considering

the role of the polyethyleneimine into the 3D structure of the sponge. In fact, as the amount of bPEI decreases, smaller molecular aggregates are expected. The higher is the amount of bPEI, more interconnections among different cellulose nanofibers are expected, leading to the formation of larger aggregates with a lower cross-linking density. On the contrary, by decreasing the amount of bPEI, the number of TOUS-CNFs involved in the formation of aggregates decreases, and consequently an intensification of cross-linking density is expected, leading to a more rigid structure.

From the qualitative description of the overall trend depicted in Fig. 4.2 and Fig. 4.3, two important conclusions can be drawn: (i) hydration leads to changes in the low- and medium-range structures of the sponge as a consequence of water confinement inside the CNS polymeric network, and (ii) the chemical composition of the sponge, and more specifically the ratio between bPEI and TOUS-CNFs, strongly affects the structure of the network. In order to quantitatively describe the structural variations occurring in the CNS sponges, and how the nano- and micro-porosity of the material change upon hydration, the Correlation Length Model (CLM) was used.

It consists in an empirical functional form describing all those kinds of profiles which have a low- and a high- q signal, like those typically observed in hydrogels [23, 26, 94–97], polyelectrolyte solutions [98] and water-soluble polymers [99].

In the framework of this model, the SANS intensity data are fitted to the following functional form:

$$I(q) = \frac{A}{q^n} + \frac{B}{1 + (\xi q)^m} + bkg. \quad (4.1)$$

This scattering law assumes the existence of two types of correlations in the scattering length density that are independent, and hence their contributions are additive in the fitting law. The first correlation is out of our experimental window, i.e. a large-scale correlation extending at distances larger than hundreds of Å (as estimated by the inverse of minimum q -value explored), and it is described by a power-law which is asymptotic and accounts for a *gel-like* behavior ($\sim q^{-2}$). The second term in the scattering law, is a Lorentzian term widely used in the aforementioned literature, that describes the high- q behavior covering a spatial scale of $\sim 10 - 100$ Å and allows to extract a *short-range correlation length* ξ . In our case, according to previously reported literature, it is reasonable to assume that the correlation length ξ can represent an estimation of the mesh size (MS) of the CNS network, in turn related to

the average distance between cross-links of the network itself. Hence, this quantity can be interpreted as an indirect estimation of the effective dimension of the nano-cavities produced by the cross-linking of the reticulated cellulose nanofibers. Going on, A and B are two free parameters that describe the weighting coefficients of these contributions. In the above model, the incoherent scattering is also taken into account by adding a constant background (bkg) term, which is left as a floating parameter. Finally, the power-law (n) and Lorentzian (m) exponents account for the scattering due to the presence of inhomogeneities on different spatial scales. As already reported [95, 99], n and m can be interpreted, for this class of systems, as the density of fibers seen at two different length scales.

In Fig. 4.4 we report an example of best-fit to the experimental data by using the CLM model, in the case of CNS (0.5:1) sample at $h = 10$.

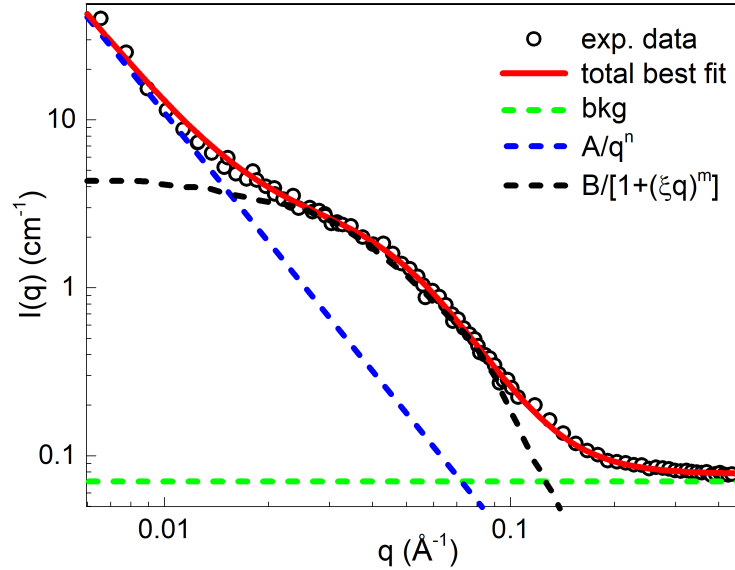


Figure 4.4: Example of best-fit applied to the experimental data, as obtained in the case of CNS (0.5:1) sample at $h = 10$.

A possible representation of the aforementioned parameters, and how these are associated to the polymeric structure of the CNS system, is reported in Fig. 4.5.

The short-range behavior of the CNS network upon increasing the amount of water can be visualized by looking at the hydration-dependence of the ξ parameter, as pointed out in Fig. 4.6 for all the investigated systems. The correlation length for CNS (0.2:1) and CNS (0.5:1) samples exhibits an almost constant behavior, with average values of ~ 17.5 Å and ~ 21 Å, respectively.

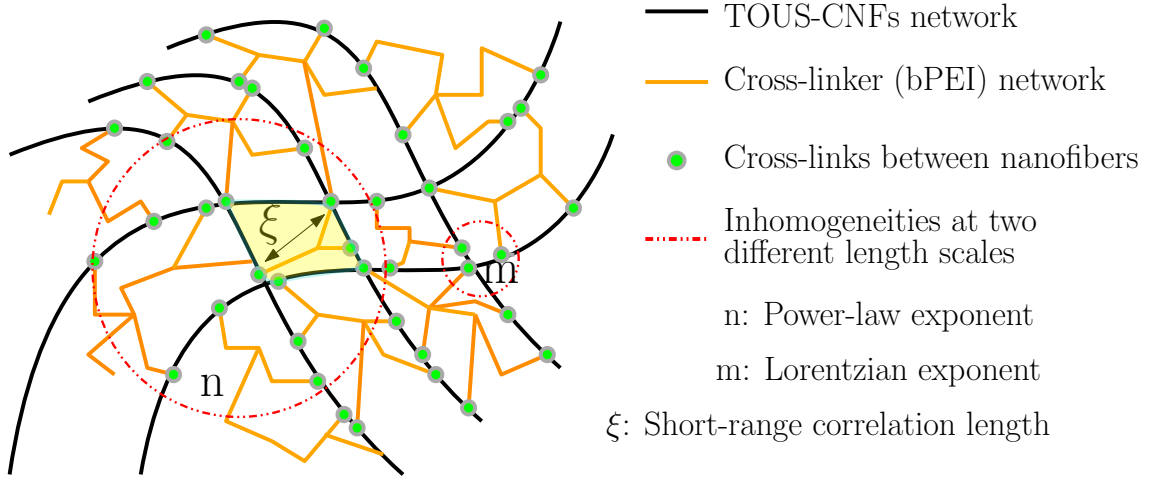


Figure 4.5: Network structure of the CNS sponge, together with the corresponding model parameters. Black lines are representative of the TOUS-CNFs network, orange lines are indicative, instead, of the cross-linker (bPEI) network. The green dots are the cross-links between nanofibers (amide covalent bonds). The dash-dotted red curves describe the presence of inhomogeneities at two different length scales, as taken into account by the power-law (n) and Lorentzian (m) exponents. Finally, as already pointed out, the correlation length ξ can be used to figure out the mesh size, i.e. the dimensions of the pores of the sponge-like material (yellow area). We remark that the reported figure has to be intended just as a fast visualization of the physical parameters under investigation, so it should not be read in scale.

On the other side, significant variations are observed for CNS (1:1) and CNS (2:1). Specifically, ξ diminishes from $\sim 29.5 \text{ \AA}$ (at $h = 1.5$) to $\sim 25 \text{ \AA}$ (at $h = 10$) for CNS (1:1), and from $\sim 34.7 \text{ \AA}$ (at $h = 1.5$) to $\sim 27.5 \text{ \AA}$ (at $h = 10$) for CNS (2:1). Based on what previously observed on similar systems [94, 100], a reduction of the correlation length is generally associated to a packing in the local structure of the CNS polymer chains.

For our investigated samples, the observed trends can be justified in terms of the onset of new physical cross-links between cellulose nanofibers due to intermolecular hydrogen bonds activated by water molecules, together with the protonation, in presence of water, of the nitrogen atoms of the primary amino groups of bPEI. Presumably, these hydrogen bonds occur between the strongly electronegative nitrogen atoms of the primary amino groups of polyethyleneimine and deuterium atoms of water molecules.

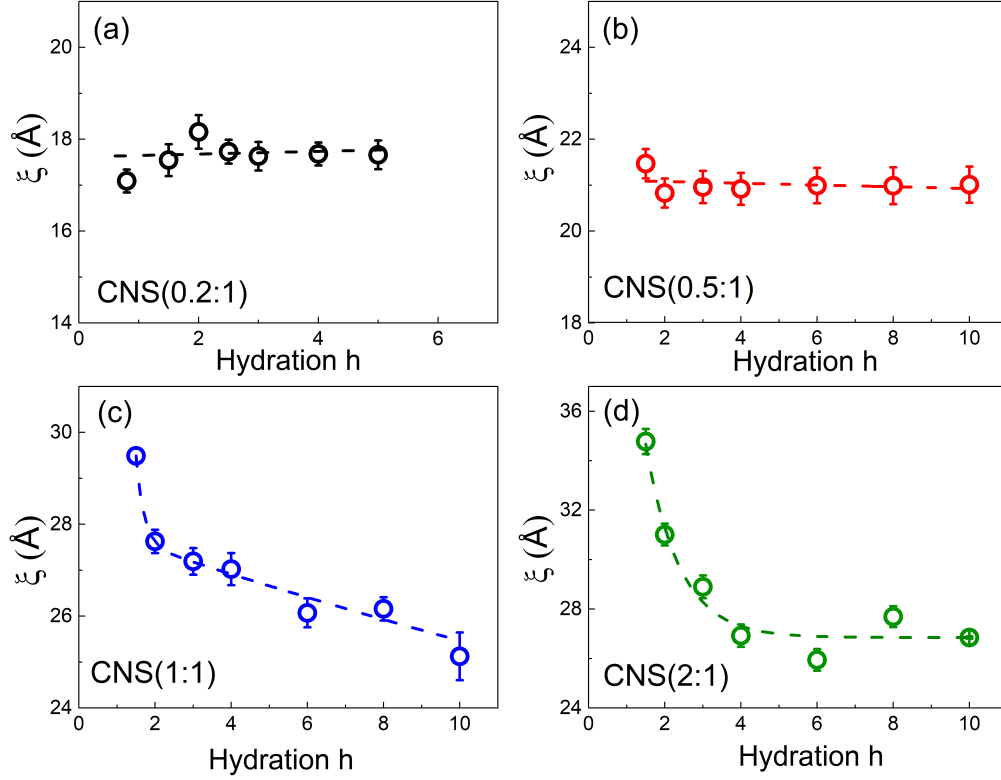


Figure 4.6: Hydration-dependence of the correlation length ξ for all the investigated CNS sponges (the dashed-lines represents a guide for eyes). Error bars represent the uncertainty from the best-fit procedure.

As a matter of fact, it has been already reported [101–104] that, thanks to the high quantity of positively charged N atoms, the bPEI behaves like a "proton sponge", showing interesting buffer properties in solution. Water molecules entrapped in the CNS local network lead to the protonation of amines, resulting in an increasing of electrostatic interactions between charged polymeric chains. This factor influences the short-range structure of the sponge (and, as we will describe in the following, the long-range one) due to the activation of repulsive electrostatic interactions involving the monomeric units of the polyethyleneimine itself. Then, an elongation of the branched chains of the bPEI as a consequence of the protonation of the primary amino groups can be reasonable, especially at high values of the hydration level h . Because of this conformational variation, the bPEI chains can entrap, in principle, an increased number of water molecules inside the nano-cavities with respect to the unprotonated condition, *via* the formation of hydrogen bonding [103].

As previously discussed, in the case of CNS (0.2:1) and CNS (0.5:1) samples, a strong interconnection between same CNFs is expected, with high-density cross-linking and consequently smaller rigid pores, whose dimension cannot be further reduced. In the case of CNS (1:1) and CNS (2:1) specimens, the increased concentration of bPEI, which implies a wider interconnection between different CNFs, leads to higher ξ values. This structure allows more water molecules to be disposed in the first solvation shell inside the pores, being involved in the formation of hydrogen bonds. Therefore, CNS (1:1) and CNS (2:1) sponges exhibit a more enhanced water confinement around the polymeric chains with respect to CNS (0.2:1) and CNS (0.5:1). This water confinement is reasonably responsible of a local re-distribution of the bPEI chains around the TOUS-CNFs network, with polyethyleneimine concentrating in specific regions of the space formed by cellulose nanofibers, i.e. of the packing of the network structure at low-scale ($\sim 10 - 100 \text{ \AA}$). At the light of the aforementioned considerations, this packing, reflected in a reduction of the polymeric mesh size defined by the CNS network, is revealed only at the highest values of the bPEI:TOUS-CNFs weight fractions.

Another factor that can contribute to justify the constant trend of the correlation length ξ observed for CNS (0.2:1) and CNS (0.5:1) samples is water saturation. Probably, these two materials reached the full hydration conditions already at the lowest analyzed hydration levels, due to the high rigidity of pores. Further added water cannot be entrapped in the pores and, hence, cannot contribute to the swelling/shrinkage of the network, whose structural features will remain almost unaltered.

The structural and conformational variations of the CNS polymeric network, as a function of hydration, and hence the possibility of “tuning” the dimensions of the micro- and nano-porosity of the cellulose material, can be also accounted by the analysis of the power-law n and Lorentzian m exponents extracted from the model. As already pointed out, the n and m exponents can be associated, for this class of materials, to the density of TOUS-CNFs at high (larger than hundreds of \AA) and low ($\sim 10 - 100 \text{ \AA}$) spatial scale, respectively.

In Fig. 4.7a and b, we display the behavior of the n and m exponents as a function of hydration level for all the investigated samples.

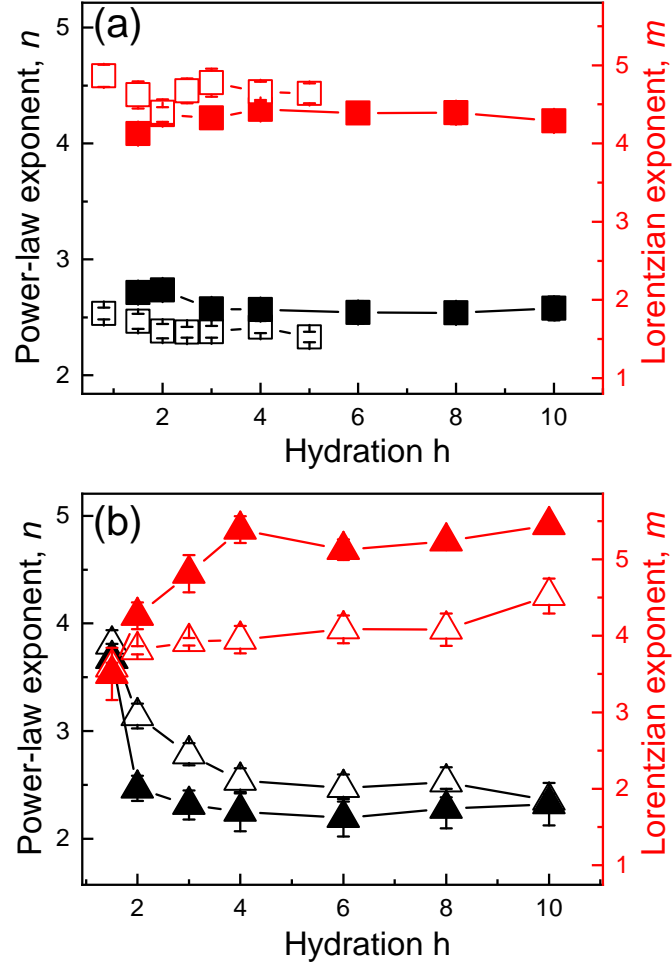


Figure 4.7: Plot of the power-law n (black symbols) and Lorentzian m (red symbols) exponents as a function of hydration level h for (a) CNS (0.2:1) (open squares) and CNS (0.5:1) (closed squares) and for (b) CNS (1:1) (open triangles) and CNS (2:1) specimens (closed triangles). Lines are guide for eyes. Error bars represent the uncertainty from the best-fit procedure.

In the case of CNS (0.2:1) and CNS (0.5:1) sponges, reported in Fig. 4.7a, both n and m exponents appear almost constant in the investigated hydration range, suggesting a constant value of the density of the nanofibers both at high and low spatial scale. This result appears in agreement with the constant trend vs. h of the correlation length ξ already observed for these systems and justified in terms of low number of N atoms involved in the hydrogen bonds with water and water saturation. On the other side, as can be seen from an inspection of Fig. 4.7b, variations in the TOUS-CNFs density are induced by the presence of water, both at high and low spatial scale, in the case of CNS (1:1) and CNS (2:1) samples.

Interestingly, for both samples the power-law exponent n exhibits, starting from $h = 1.5$, a diminishing tendency by increasing the water content. This observation can be explained by taking into account that, for low hydration levels, the systems reasonably show scattering associated to the presence of homogeneous clusters conformations, caused by bPEI and TOUS-CNFs densely arranged in space. In fact, as stated above, for low content of water the bPEI chains are almost unprotonated, with a high hydrophobicity that does not allow the swelling of the material. As the water content increases, the observed diminishing of the large-scale density of NFs accounted by the power-law exponent reveals a change in the medium-range structure, that passes from a homogeneous cluster conformation (Fig. 4.8, at the top), to a “swelled” structure characterized by the formation of polymeric “bubbles” inside the CNS network (Fig. 4.8, at the bottom). At the same time, the low-scale clustering, already highlighted for these systems by the diminishing vs. h of the correlation length ξ , is reflected in an increasing of the Lorentzian exponent m , indicative of an increasing of the local density of TOUS-CNFs and bPEI at spatial windows of $\sim 10 - 100 \text{ \AA}$. As indirect consequence, this process leads to an increasing of the dimensions of the micro-cavities at medium range, that will contain a reduced number of bPEI and TOUS-CNFs units (Fig. 4.8, at the bottom). In addition, the role played by water molecules entrapped in the nano-sized domains and not entrapped must also be considered in justifying these structural changes. On one side, in fact, water molecules out of nano-cavities exert a not-negligible hydrostatic pressure on the polymeric bubbles that tends to enlarge the network. On the other side, this structural variation is also favored by water molecules confined in the nano-pores, where the establishment of new physical cross-links, which tends to attract cellulose chains, will cause a densification at low scale with the formation of water “pocket”.

In support of what has just been stated, it is also worth remarking that, as well known [105], the plot $\log[I(q)]$ vs. $\log(q)$ can yield information about the so-called “fractal dimension” of the scattering objects. A value of n between 3 and 4 characterizes rough interfaces of “surface fractals” of fractal dimension D , with $n = 6 - D$. $n = 3$ is indicative of collapsed polymer coils, whereas a value of n between 2 and 3 is indicative of “mass fractals” such as branched systems (gels).

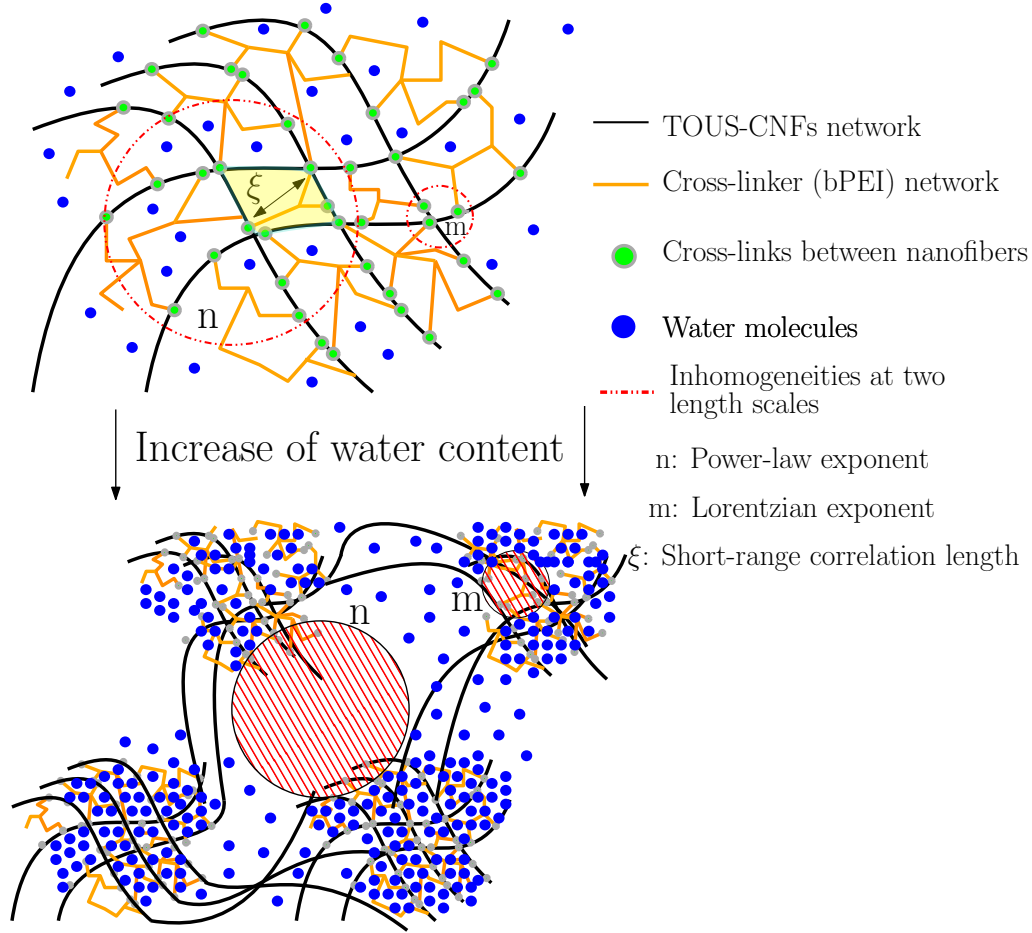


Figure 4.8: Schematic overall representation of the structural variations exhibited by the CNS network by increasing the water content. As can be seen, at low h -values the system shows an almost homogeneous conformation. The symbols correspond to those reported in the caption of Fig. 4.5, with blue dots representing water molecules, in addition. By increasing h , a conformational change at short range is observed, leading to the formation of fiber-poor and fiber-rich regions whose density will be taken into account by the n and m exponents behavior (see text for details). We remark that the reported figure has to be intended just as a fast visualization of the physical parameters under investigation, so it should not be read in scale.

In the case of CNS (0.2:1) and CNS (0.5:1) sponges, the power-law exponent n turns out to be between 2 and 3 in the whole h -range explored, suggesting the presence of mass fractals typical of a gel-like structure. For CNS (1:1) and CNS (2:1) systems, the power-law exponent n assumes a value of ~ 3.8 at the lowest investigated hydration level ($h = 1.5$), indicating a dense structure due to the presence of sharp interfaces. By increasing h , a progressive diminishing of n is observed,

that reaches a value of ~ 2.3 at the highest hydration ($h = 10$). This implies that, in the analyzed hydration range, the systems undergo a structural transition from a more rigid network to a flowing gel state. An inspection of Fig. 4.7b gives a first estimation of the cross-over value h^* at which this transition occurs, between 2 and 3 for CNS (1:1) sample, and between 1.5 and 2 for CNS (2:1) system. Nevertheless, for an accurate evaluation of this cross-over, further SANS measurements focused in these specific intervals are necessary.

Finally, we also investigated the role of a co-crosslinker, i.e. citric acid (CA), on the structural properties of CNS. CA is an organic polycarboxylic acid made up of one hydroxyl and three carboxyl functional groups, which acts as cross-linking agent enhancing the mechanical stability of the structure by activation of covalent interactions [106]. As widely reported in literature, the multi-carboxyl nature of such compound promotes the reticulation with a large amount of polysaccharides, including cotton fibers [107], cellulose films [108] and chitin derivatives [109]. CA has already been proved to interact with the bPEI/TOUS-CNFs network according to two different mechanisms [23]. The first one involves the onset of new amine-based covalent interactions between CA and bPEI chains, the second one regards the esterification process.

In Fig. 4.9 the short-range correlation length ξ and Lorentzian exponent m as a function of the water content h for samples CNS (2:1) and CNS (2:1)-CA are reported. As can be seen, the low-scale behavior in the case of CNS (2:1)-CA is different from that of CNS (2:1), indicative of a strong influence of CA on the bPEI/TOUS-CNFs network. In particular, the presence of citric acid seems to “stabilize” the low-scale arrangement, as suggested by the constant trend of both ξ and m . This occurrence can be explained considering that the presence of CA promotes a significant increase of cross-linking, maximizing the interconnections between single fibers and thus minimizing links distances and pores dimensions. Coherently, the effect of CA on high-scale structure of the investigated sponge can be visualized by comparing the behavior of the power-law exponent n as a function of h for CNS (2:1) and CNS (2:1)-CA, as displayed in Fig. 4.10.

The high values of the power-law exponent for sample CNS (2:1)-CA with respect to CNS (2:1), obtained at all the hydration levels, are indicative of an increasing of the fibers density in the high spatial scale.

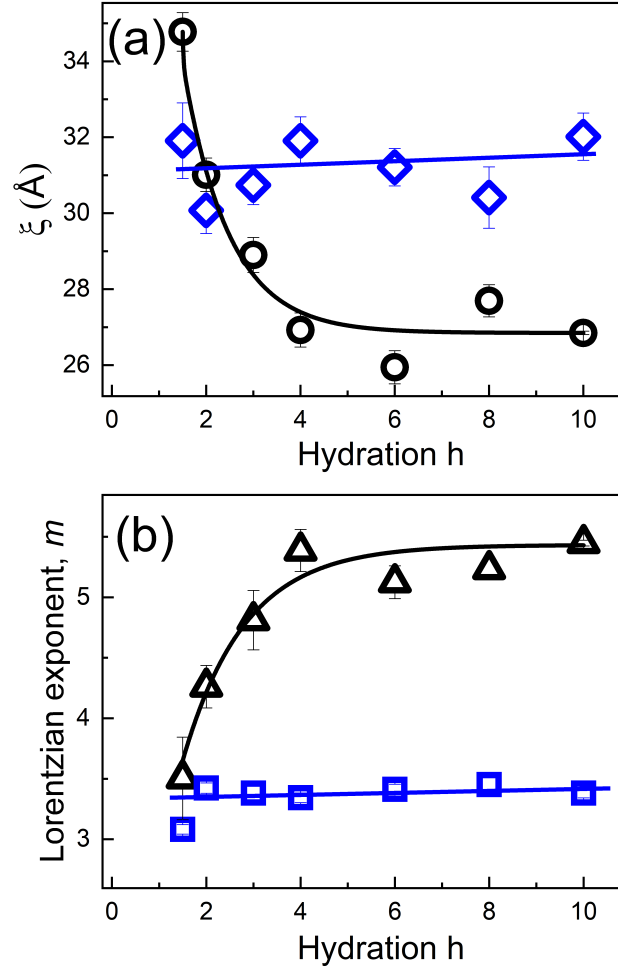


Figure 4.9: h -dependence of (a) short-range correlation length ξ and (b) Lorentzian exponent m for CNS (2:1) (black symbols) and CNS (2:1)-CA (blue symbols) sponges.

Reasonably, the formation of amide bonds between bPEI chains and the carboxyl acid moieties of CA leads to a denser and more rigid structure compared to that of CNS (2:1), due to the increase of new intermolecular bonds. Consequently, we can hypothesize that the addition of citric acid allows the reduction of the size of the micro-bubbles induced by the presence of water molecules.

Interestingly, the trend vs. h of m and n exponents observed for CNS (2:1)-CA closely recalls that of CNS (0.2:1) and CNS (0.5:1) systems. This occurrence testifies that the addition of CA brings the network from an elastic condition, characterizing samples with the highest content of bPEI, to a more rigid conformation, typical of the samples at the lowest content of bPEI. In particular, n values in the case of CNS

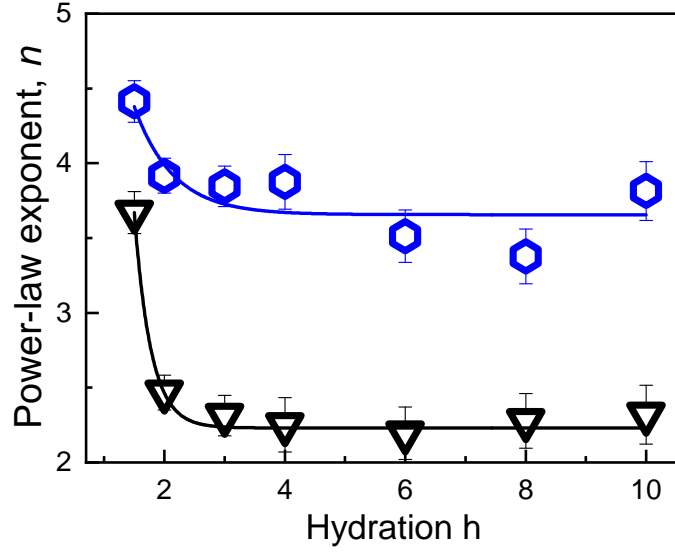


Figure 4.10: h -dependence of the power-law exponent n for CNS (2:1) (black symbols) and CNS (2:1)-CA (blue symbols) sponges.

(2:1)-CA turned out to be, at all the analyzed hydration levels, definitely higher than the values of CNS (0.2:1) and CNS (0.5:1), whereas m values are almost comparable. We can explain this occurrence thinking that CA, acting as co-crosslinker, will force the fibers to stay closer, at long distances. At short distances, instead, a condition, also in terms of rigidity, similar to that of CNS (0.2:1) and CNS (0.5:1) samples will be restored.

These observations are consistent with those reported in a previous study, where we reported a significant increase of the Young's modulus in the presence of increasing amounts of CA compared to the CNS (2:1) sample [23].

Chapter 5

Vibrational dynamics in bPEI/TOUS-CNFs sponges

FTIR-ATR measurements have been performed on bPEI/TOUS-CNFs sponges following the procedure described in section 3.7 ("*FTIR experiment*"). The results reported here are, however, preliminary, and a detailed analysis is still in progress.

Fig. 5.1 reports the comparison between the experimental FTIR-ATR spectra of samples CNS (0.2:1), CNS (1:1) and CNS (2:1) in (a) H₂O and (b) D₂O, at T = 300 K and $h = 1.5$, as example. The absorption bands at ~ 896 , ~ 1027 , ~ 1334 , ~ 1367 and ~ 1428 cm⁻¹ belong to stretching and bending vibrations of C—O, —OH, —CH and —CH₂ bonds in cellulose [110, 111]. Going on, the absorption peak at ~ 1588 cm⁻¹ can be associated with the residual —COO⁻ groups of the TOUS-CNFs [23]. As we can see from a first inspection of Fig. 5.1, all spectra show the presence of an intense peak at ~ 1650 cm⁻¹ associated to the C=O stretching vibration due to the formation of amide moieties. Being the bPEI mainly constituted by primary, secondary and tertiary amino groups in a 25/50/25 molar ratio, we can justify the increase of the C=O stretching peak intensity observed in the FTIR-ATR spectra as a consequence of the increase of the amino functional groups inside the CNS polymeric network. At ~ 2400 cm⁻¹, the symmetric stretching mode vibration of O—D can be also detected, which appear particularly intense even at $h = 1.5$. Peaks at ~ 2900 cm⁻¹ are attributed to different —CH₂ stretching vibrations of all hydrocarbon constituent in polysaccharides [112].

Furthermore, the N—H stretching peak can be clearly detected at ~ 3300 cm⁻¹.

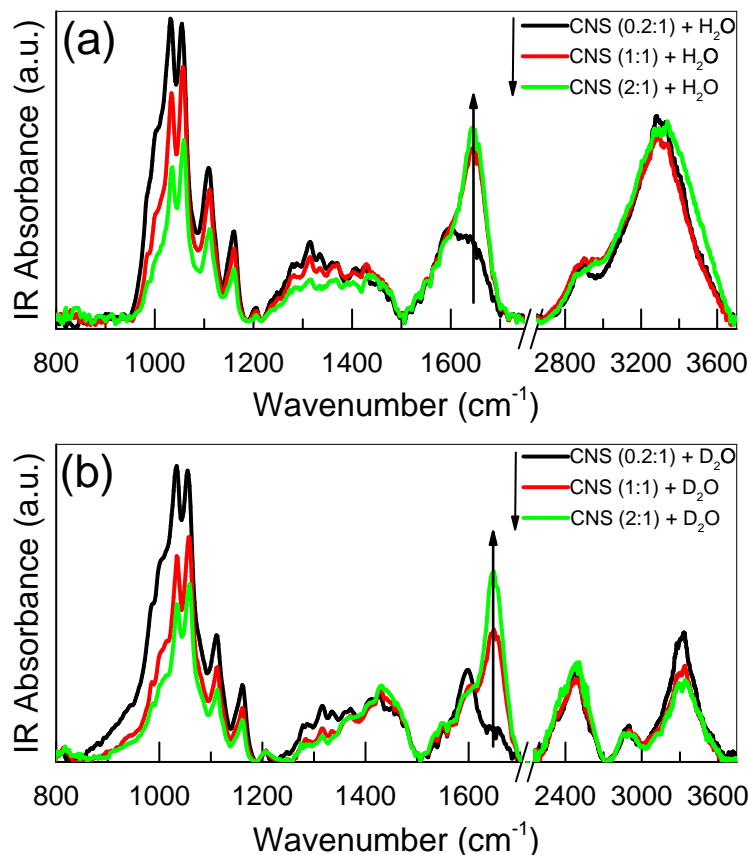


Figure 5.1: FTIR-ATR spectra of bPEI/TOUS-CNFs sponges with: (black curve) 0.2 g, (red curve) 1 g and (green curve) 2 g of bPEI in (a) H_2O and (b) D_2O . The arrow indicates the increase of cross-linker.

It partially overlaps the broad O—H stretching band, as can be observed. Moreover, in sponge hydrated with H_2O , the contribution due to H—O—H bending mode ($\delta(\text{HOH})$, $\sim 1630 \text{ cm}^{-1}$) of water molecules engaged in the system appears partially overlapped to the C=O vibration. Worth of note, the presence of the O—H broad band even in deuterated samples is observed. It can be explained considering that, as suggested by many authors, the use of D_2O as solvent in aqueous solution leads to an immediate D—H exchange between D atoms of heavy water and superficial H atoms of the xerogel matrix. As a result, we assist to the formation of DHO (deuterium-hydrogen-oxygen) water molecules whose contribution to the FTIR spectra can be found in the $3000 \text{ cm}^{-1} - 3650 \text{ cm}^{-1}$ region. In addition, O—H stretching modes can be found in hydroxyl groups in polysaccharides promoting intra- and intermolecular

HBs between cellulose chains [112]. Based on these considerations, we can suppose, in agreement with previous studies [113–115], that DHO water molecules are those strongly interacting with the chemical groups of the bPEI/TOUS-CNFs cavities.

As preliminary results, in Fig. 5.2(a) we report the temperature-evolution of the IR spectra recorded on sample CNS (1:1) after hydration with water (hydration level $h = 2$) in the spectral window 1500–1800 cm^{-1} and at different selected temperatures. Fig. 5.2(b) shows the IR spectra acquired on CNS (1:1) hydrated with D_2O at $h = 2$ and at the same temperatures of the data reported in Fig. 5.2(a).

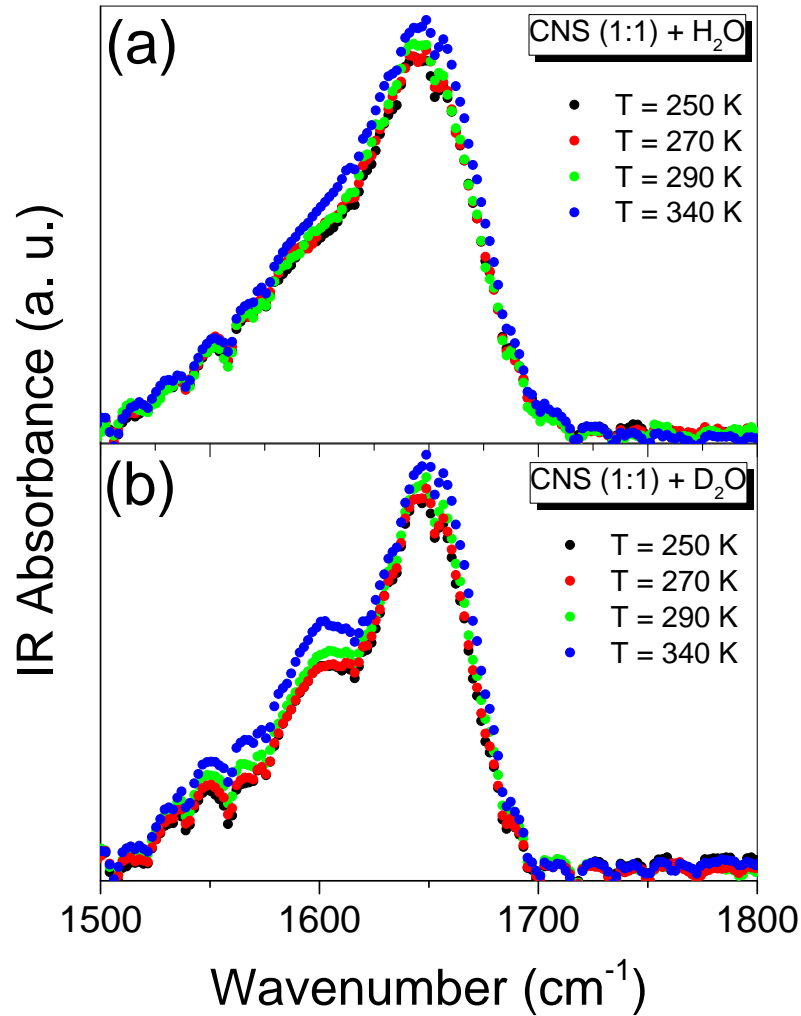


Figure 5.2: Temperature-evolution of the infrared spectra obtained for CNS (1:1) hydrated in H_2O (a) and D_2O (b).

It appears evident that in the spectra of sponges prepared with deuterated water the characteristic HOH bending mode of engaged H_2O is not present, as expected.

Indeed, it is well known [116] that the DOD (deuterium-oxygen-deuterium) bending mode of D₂O is shifted in the vibrational spectra to $\sim 1210\text{ cm}^{-1}$. Thus, the use of D₂O instead of H₂O for the polymer swelling allows us to separate and to examine the effect of the water confinement on the vibration modes assigned to the sponge matrix and on the HOH bending mode of engaged H₂O molecules.

The experimental profiles of Fig. 5.2 point out that the increase of temperature is responsible for variations of the IR spectrum of the sponge. The feature at about $\sim 1630\text{ cm}^{-1}$ associated to the HOH bending mode of H₂O tends to become more intense at high temperatures. At the same time, the total intensity of the residual —COO[−] peak ($\sim 1588\text{ cm}^{-1}$) and of the C=O stretching band ($\sim 1650\text{ cm}^{-1}$) of the polymer increases.

The temperature evolution of the vibrational modes of nanosponge can be better visualized looking at the profiles of Fig. 5.2(b), where these bands are not strongly deconvoluted with the bending mode of water. The increasing intensity of the C=O stretching mode in bPEI/TOUS-CNFs sponge as a function of temperature is consistent with previous experimental investigations and it has been explained by taking into account that the thermal motion tends to induce a destructuring effect on the hydrogen bond network of H₂O or D₂O molecules which surround the C=O groups of the polymer. As a consequence, the electrostatic environment experienced by these chemical groups of polymer is such that it reinforces the overall dipole moment of the CO functional group [116].

In order to better emphasize the temperature-behaviour of the HOH bending mode of confined water, we report in Fig. 5.3 the spectral contribution of this mode at $T = 290\text{ K}$, as example. Such mode is isolated by considering the experimental profiles of CNS (1:1) hydrated in H₂O and in D₂O. The profile in deuterated water is then subtracted from the corresponding in H₂O. The spectra in H₂O and D₂O have been preliminary normalized to the intensity of the band at about $\sim 1030\text{ cm}^{-1}$, assumed as a reliable internal standard [116–119].

Indeed, the latter vibrational mode is related to stretching vibrations of C–O groups of the cellulose material that are not expected to be affected by the hydration of the sponge or by a variation of temperature.

Fig. 5.3 presents the superimposition of the normalized spectral profile of the protium and deuterated sponge in the spectral region, $1500 - 1800\text{ cm}^{-1}$.

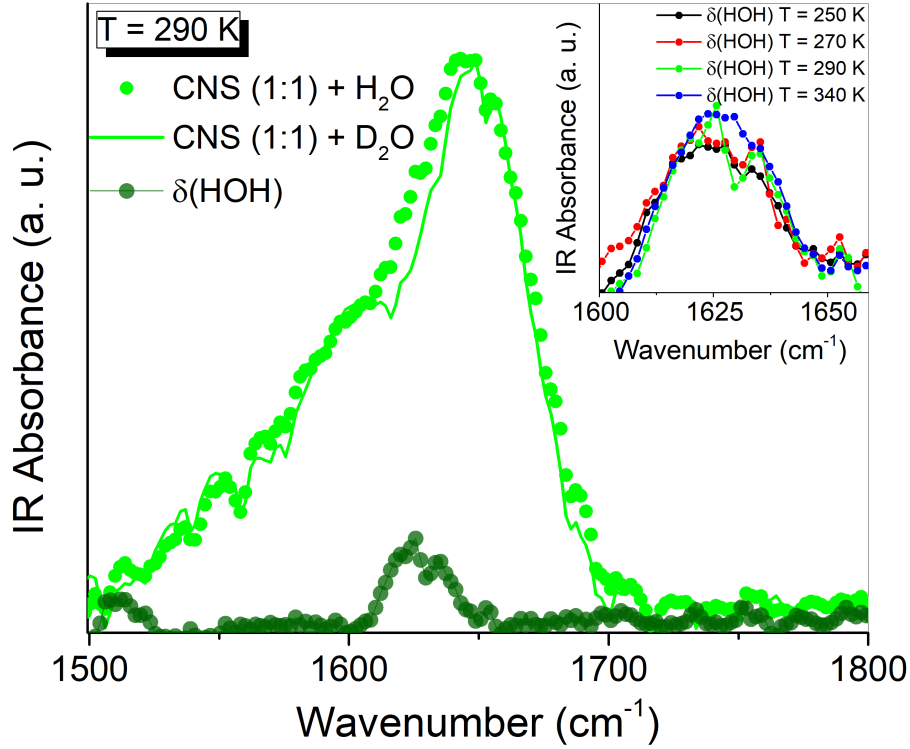


Figure 5.3: Infrared spectra obtained for CNS (1:1) in H₂O (green dots) at $T = 290$ K; in the same panel, the contribution of HOH bending of water was isolated by subtraction of the signal of CNS (1:1) in D₂O (see text for details). In the inset, the temperature-evolution of the HOH bending mode of water is reported.

The profile of D₂O sponge traces, within the experimental error, the corresponding spectrum in H₂O except for the component of HOH bending mode. This finding confirms the reliability of the data handling followed for the subtraction of the spectra. As first important result, we find that HOH bending mode of water at $T = 250$ K (inset of Fig. 5.3, black profile) shows a characteristic Gaussian-like form different from the nearly flattened profile typically exhibited by polycrystalline ice at the same temperature [120–122]. Indeed, previous IR measurements independently performed by different authors [120–122], consistently show that during the phase transition, the IR absorption band of the bending mode of water undergoes sharp changes in the spectra of both H₂O and D₂O: in the solid phase, the bending mode appears very weak, while in the liquid state this band is a dominating peak. Moreover, in the crystalline ice at temperatures below of $T = 264$ K, the HOH bending mode rapidly vanishes and it appears as a very weak flattened profile, as clearly shown in Refs. [120] and [122].

Based on these considerations, the spectra of Fig. 5.3 give evidence that the H₂O molecules engaged in the polymer network of nanosponge remain in liquid state even below the nucleation temperature where usually the bulk water crystallizes. This finding, recalling what already observed for water entrapped in a variety of amorphous porous materials and phyllosilicates [121, 123–125], is consistent with the conclusion that water is strongly confined in the nano-cavities of nanosponge polymer in the xerogel phase. In addition, the comparison of the HOH bending mode observed at different temperatures (inset of Fig. 5.3) points out an increase in intensity of this mode and a slight shift to lower wavenumber upon the increase of temperature. This behaviour, recalling what already observed in bulk water [120, 126, 127] and in water confined in other nano-porous systems [121, 123–125], indicates a sudden decrease in the molecular connectivity of the water molecules arranged in hydrogen bond networks as a consequence of the thermal motion.

Finally, we discuss, as example, the temperature-evolution of the IR spectra of CNS (1:1) hydrated in D₂O in the high frequency range of 2700–3700 cm⁻¹ (Fig. 5.4, panel at the top), where the characteristic OH stretching modes (ν_{OH}) of water are typically observed [116, 128–131]. As suggested by other authors in the case of aqueous solutions of proteins [132], the use of D₂O as solvent allows to selectively probe the ν_{OH} modes of water molecules resulting from isotopic exchanges between the superficial H atoms of bPEI/TOUS-CNFs sponge and the solvent D₂O placed closely around the polymer surface, namely, DHO (deuterium-hydrogen-oxygen) water molecules. These water molecules give a contribution to the IR spectrum in the OH stretching region between 2700 and 3700 cm⁻¹ which appears significantly different from that observed for the same sample in H₂O, as pointed out in the inset of Fig. 5.4. This occurrence, in agreement with previous studies [113–115] is consistent with the hypothesis that the DHO spectrum reflects a population of water molecules which more strongly interact with the chemical groups of bPEI/TOUS-CNFs sponge within the nano-cavities of the xerogel. Consequently, the DHO spectrum can be considered to be free of intermolecular coupling vibrations and it is called uncoupled stretching region [132].

As a general trend, we observe a slight shift to higher frequency of the DHO spectrum upon the increase of temperature (Fig. 5.4, panel at the top) together

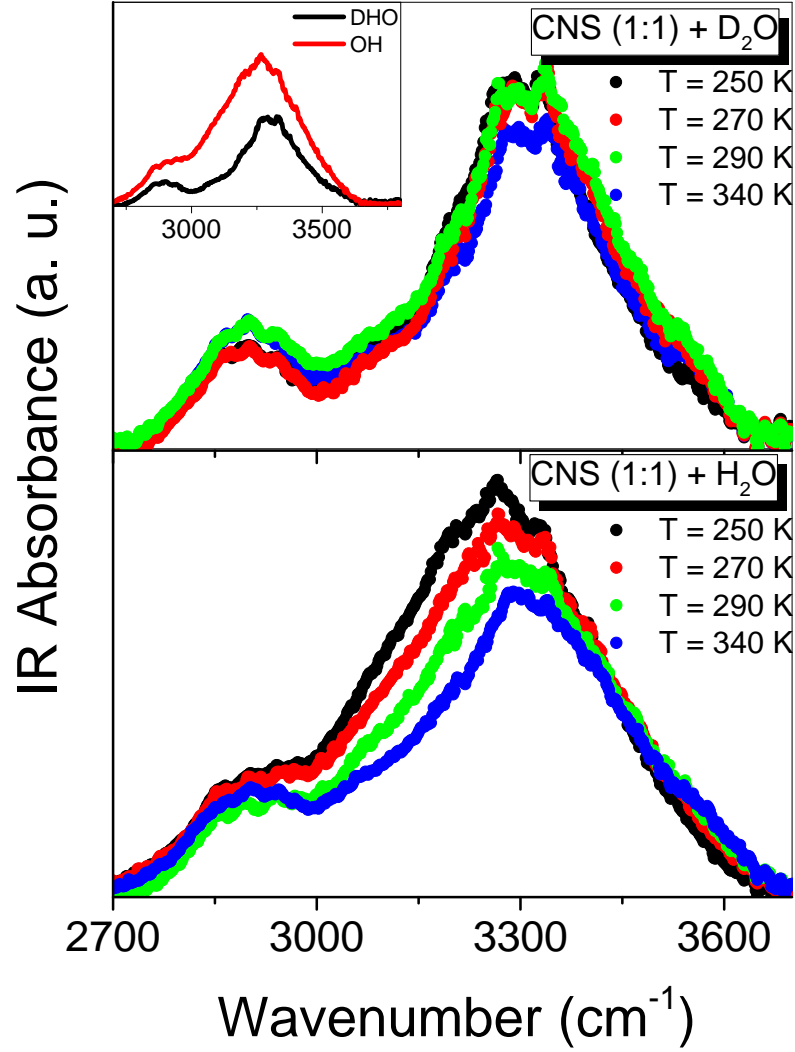


Figure 5.4: Selected IR spectra of CNS (1:1) in D₂O (panel at the top) and H₂O (panel at the bottom) at different values of temperature in the high-frequency range of 2700 – 3700 cm⁻¹. Inset: comparison between the OH stretching band in H₂O-sponge and in DHO spectrum, at T = 250 K.

with an attenuation in intensity of the low-frequency contributions of the DHO stretching band (shoulder at about 3250 cm⁻¹). As expected, a similar trend is found also for the OH stretching band of engaged water, as evident by inspection of the spectra of CNS (1:1) in H₂O (Fig. 5.4, panel at the bottom).

These experimental findings are consistent with the behaviour observed and above discussed for the HOH bending mode of water and confirm the destructuring effect induced by the thermal motion on the water molecules confined in bPEI/TOUS-CNFs cavities. As widely reported in literature [113, 127, 133, 134],

the ν_{OH} vibrations of water are particularly sensitive to the co-operativity of the HB arrangements developed by the solvent molecules in the sponge. This suggests that the DHO spectrum may be interpreted in terms of the local environment of the water molecules present in the system [113, 127, 133–138]. By recalling a well assessed model [135–138] already applied to the analysis of the OH stretching band in Raman and IR spectra of similar systems [116, 128–131], the spectral modifications observed in the DHO spectrum can be quantitatively related to different co-operativity degrees of the HB arrangements of water more closely confined in the pores of bPEI/TOUS-CNFs sponge.

After a preliminary subtraction from the total DHO profile of the spectral signal assigned to the CH vibrational modes of nanosponges (signals falling between about 2760 and 3050 cm^{-1}), the DHO stretching band of water has been decomposed into four different contributions corresponding to four classes of OH oscillators present in the system [135–138].

A typical result of the fitting procedure obtained for the DHO spectrum of CNS (1:1) at $T = 270$ K (panel at the top) and $T = 320$ K (panel at the bottom) is shown in Fig. 5.5, as example.

Taking into account the interpretation of the spectral components of the OH band as reported in literature [135–138], the sum of the percentage intensities of the two sub-bands at the lowest wavenumbers, labelled as $I_1 + I_2$, can be used to describe the population of water molecules arranged in tetrahedral HB networks that exhibit strong hydrogen bonding on both the hydrogen atoms. Conversely, the sum of the two other contribution to the DHO band, $I_3 + I_4$, is representative of the population of water molecules that develop less strongly interconnected HB patterns with coordination number less than four [128–130]. The temperature-dependence of percentage intensities $I_1 + I_2$ and $I_3 + I_4$ obtained for the DHO spectrum is reported in Fig. 5.6. It clearly appears that an increase of the temperature, T , corresponds to a reduction of the population of water molecules arranged in tetrahedral HB networks ($I_1 + I_2$), i.e., bulk-like contribution.

Correspondingly, an enhancement of the population of water molecules involved in HB network with connectivity less than four ($I_3 + I_4$, not bulk-like water) is observed upon the increase of temperature.

The plot of Fig. 5.6 shows the existence of a characteristic crossover point at

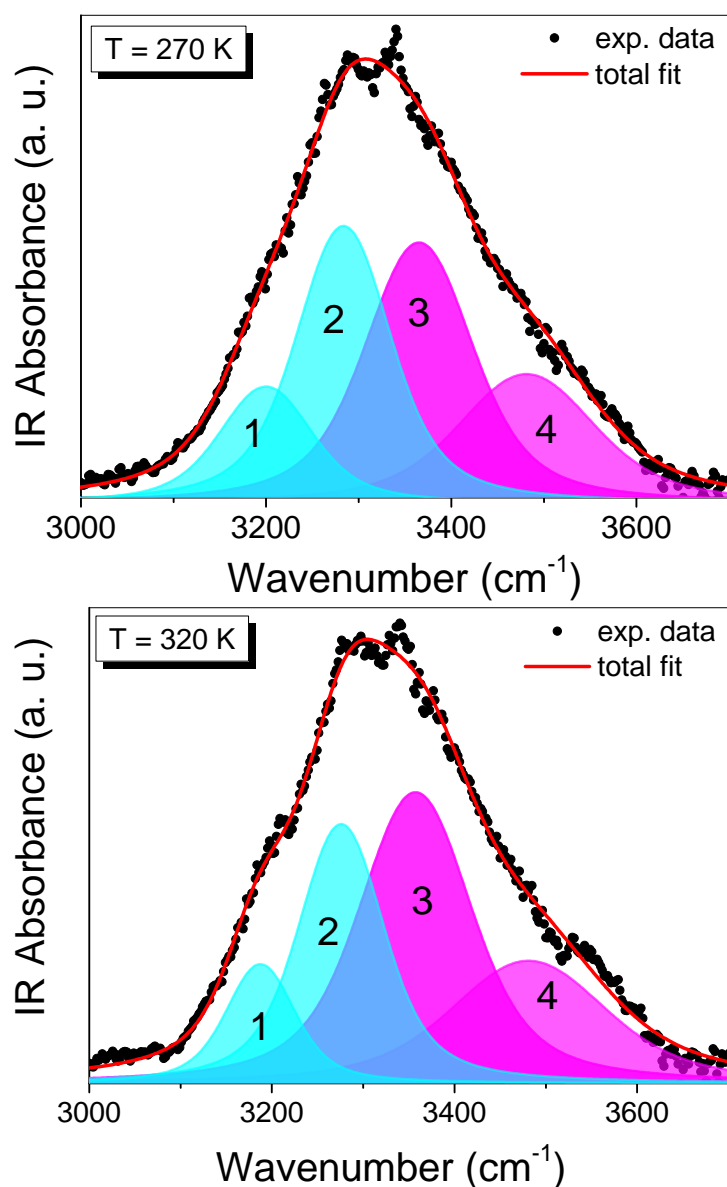


Figure 5.5: Typical schematic of the fitting procedure results for DHO spectrum of CNS (1:1) at $T = 270$ K (panel at the top) and $T = 320$ K (panel at the bottom).

about $T = 260$ K, where the population of not bulk-like water molecules becomes favoured with respect to the population of bulk-like water. This occurrence suggests that the water molecules more closely confined in the cavities of polymer preferably develop HB networks with connectivity less than four, even at low temperature, due to the proximity with the chemical groups of the bPEI/TOUS-CNFs sponge. A more detailed analysis is, at present, in progress.

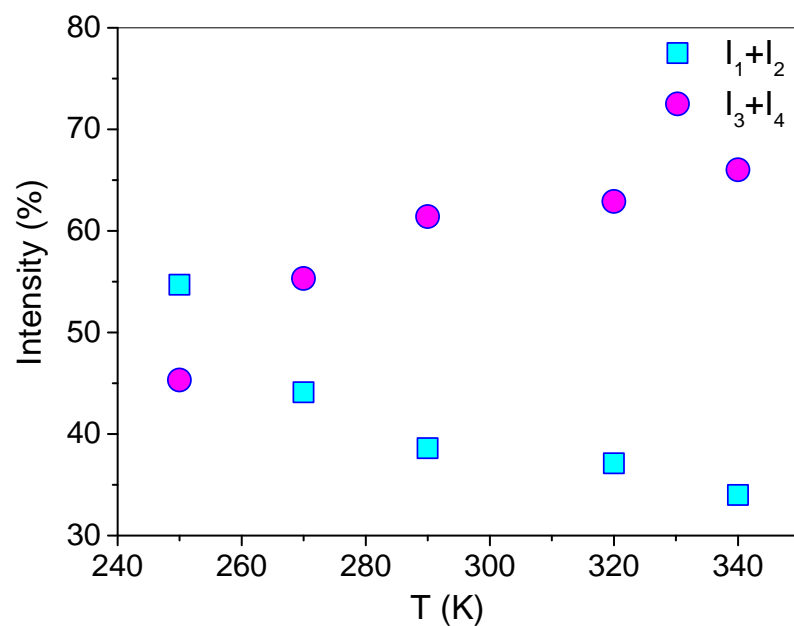


Figure 5.6: Percentage intensities $I_1 + I_2$ and $I_3 + I_4$ of the spectral contributions to the DHO stretching band as a function of temperature, T , for sample CNS (1:1).

Conclusions

In this thesis, a structural and dynamical investigation of cellulose nanosponges (CNS), obtained by cross-linking TEMPO oxidized and ultra-sonicated cellulose nanofibers with branched polyethyleneimine, was performed by Small Angle Neutron Scattering (SANS) and Fourier-Transform Infrared (FTIR) spectroscopy techniques, respectively. From the SANS results, the CNS hydration is shown to give rise to significant structural changes at two different length scales, as described by the trend of scattering intensity versus the scattering wavevector modulus q . This revealed inhomogeneity in the density of the nanofibers caused by the presence of water molecules. The analysis of the experimental data, performed in terms of a Correlation Length Model (CLM), allowed us to demonstrate the role of the cross-linker and hydration in determining the density of CNFs at high (power-law exponent) and low (Lorentzian exponent) spatial scale. For the very first time it was also possible to reveal the nano-porosity in the TOUS-CNFs network by determining the short-range correlation length ξ , and its variation in terms of hydration and cross-linking, reaching the same minimum both at the highest hydration levels and the lowest amounts of bPEI. In this latter case, a higher cross-linking density is expected among fewer CNFs. Finally, the role of citric acid as additional cross-linker was shown in terms of increased CNFs density and ξ minimization.

From the FTIR results, the molecular connectivity and the extent of hydrogen bonds patterns of water molecules confined in these sponges was clarified. As main result, the HOH bending mode of water in sponge exhibits, at temperatures below ~ 270 K, a characteristic form quite different from the flattened profile typically observed for polycrystalline ice, giving a strong experimental evidence of a liquid-like behaviour of the H_2O molecules confined in the nano-cavities of TOUS-CNFs matrix. Moreover, the changes in wavenumber position and intensity observed for HOH bending mode of water upon the increase of temperature indicate a character-

istic destructuring effect on the hydrogen bond pattern of confined water molecules, induced by thermal motion.

The overall results provides an unprecedent characterization of structural and dynamical properties of bPEI/TOUS-CNFs sponges, and constitute a key preliminary step to understand the close relationship between these properties and the functionality of these materials, also in view of their possible application in many different technological fields.

Bibliography

- [1] G. Centi and S. Perathoner. Remediation of water contamination using catalytic technologies. *Applied catalysis B: environmental*, **41**(1-2):15–29, 2003.
- [2] Y.-E. Miao, R. Wang, D. Chen, Z. Liu, and T. Liu. Electrospun self-standing membrane of hierarchical $\text{SiO}_2@ \gamma\text{-AlOOH}$ (Boehmite) core/sheath fibers for water remediation. *ACS applied materials & interfaces*, **4**(10):5353–5359, 2012.
- [3] U. V. Gunten. Ozonation of drinking water: part I. Oxidation kinetics and product formation. *Water research*, **37**(7):1443–1467, 2003.
- [4] X. Chen, G. Chen, and P. L. Yue. Novel electrode system for electroflotation of wastewater. *Environmental science & technology*, **36**(4):778–783, 2002.
- [5] C.-Y. Hu, S.-L. Lo, and W. Kuan. Effects of co-existing anions on fluoride removal in electrocoagulation (EC) process using aluminum electrodes. *Water research*, **37**(18):4513–4523, 2003.
- [6] B. Van der Bruggen and C. Vandecasteele. Removal of pollutants from surface water and groundwater by nanofiltration: overview of possible applications in the drinking water industry. *Environmental pollution*, **122**(3):435–445, 2003.
- [7] V. V. Goncharuk, D. D. Kucheruk, V. M. Kochkodan, and V. P. Badekha. Removal of organic substances from aqueous solutions by reagent enhanced reverse osmosis. *Desalination*, **143**(1):45–51, 2002.
- [8] U. I. Gaya and A. H. Abdullah. Heterogeneous photocatalytic degradation of organic contaminants over titanium dioxide: a review of fundamentals, progress and problems. *Journal of photochemistry and photobiology C: photochemistry reviews*, **9**(1):1–12, 2008.

- [9] V. J. Inglezakis, M. D. Loizidou, and H. P. Grigoropoulou. Ion exchange of Pb^{2+} , Cu^{2+} , Fe^{3+} , and Cr^{3+} on natural clinoptilolite: selectivity determination and influence of acidity on metal uptake. *Journal of colloid and interface science*, **261**(1):49–54, 2003.
- [10] R. Celis, C. Hermosin, and J. Cornejo. Heavy metal adsorption by functionalized clays. *Environmental science & technology*, **34**(21):4593–4599, 2000.
- [11] A. Zhang, T. Asakura, and G. Uchiyama. The adsorption mechanism of uranium (VI) from seawater on a macroporous fibrous polymeric adsorbent containing amidoxime chelating functional group. *Reactive and functional polymers*, **57**(1):67–76, 2003.
- [12] T. Robinson, B. Chandran, and P. Nigam. Studies on desorption of individual textile dyes and a synthetic dye effluent from dye-adsorbed agricultural residues using solvents. *Bioresource technology*, **84**(3):299–301, 2002.
- [13] M.-W. Jung, K.-H. Ahn, Y. Lee, K.-P. Kim, J.-S. Rhee, J. T. Park, and K.-J. Paeng. Adsorption characteristics of phenol and chlorophenols on granular activated carbons (GAC). *Microchemical journal*, **70**(2):123–131, 2001.
- [14] S. Srivastava, A. Kardam, and K. R. Raj. Nanotech reinforcement onto cellulosic fibers: green remediation of toxic metals. *International journal of green nanotechnology*, **4**(1):46–53, 2012.
- [15] A. Kardam, K. R. Raj, and S. Srivastava. Novel nano cellulosic fibers for remediation of heavy metals from synthetic water. *International journal of nano dimension*, **3**(2):155–162, 2012.
- [16] A. Kardam, K. R. Raj, S. Srivastava, and M. M. Srivastava. Nanocellulose fibers for biosorption of cadmium, nickel, and lead ions from aqueous solution. *Clean technologies and environmental policy*, **16**(2):385–393, 2014.
- [17] A. W. Carpenter, C.-F. de Lannoy, and M. R. Wiesner. Cellulose nanomaterials in water treatment technologies. *Environmental science & technology*, **49**(9):5277–5287, 2015.

- [18] A. J. Svagan, M. A. S. A. Samir, and L. A. Berglund. Biomimetic foams of high mechanical performance based on nanostructured cell walls reinforced by native cellulose nanofibrils. *Advanced materials*, **20**(7):1263–1269, 2008.
- [19] F. Soyekwo, Q. Zhang, R. Gao, Y. Qu, C. Lin, X. Huang, A. Zhu, and Q. Liu. Cellulose nanofiber intermediary to fabricate highly-permeable ultrathin nanofiltration membranes for fast water purification. *Journal of membrane science*, **524**:174–185, 2017.
- [20] S. Musyoka, C. Ngila, B. Moodley, A. Kindness, L. Petrik, and C. Greyling. Oxolane-2,5-dione modified electrospun cellulose nanofibers for heavy metals adsorption. *Journal of hazardous materials*, **192**(2):922–927, 2011.
- [21] L. Melone, B. Rossi, N. Pastori, W. Panzeri, A. Mele, and C. Punta. TEMPO-oxidized cellulose cross-linked with branched polyethyleneimine: nanostructured adsorbent sponges for water remediation. *Chempluschem*, **80**(9):1408–1415, 2015.
- [22] I. Corsi, A. Fiorati, G. Grassi, I. Bartolozzi, T. Daddi, L. Melone, and C. Punta. Environmentally sustainable and ecosafe polysaccharide-based materials for water nano-treatment: an eco-design study. *Materials*, **11**(7):1228–1250, 2018.
- [23] A. Fiorati, G. Turco, A. Travan, E. Caneva, N. Pastori, M. Cametti, C. Punta, and L. Melone. Mechanical and drug release properties of sponges from cross-linked cellulose nanofibers. *Chempluschem*, **82**(6):848–858, 2017.
- [24] B. Rossi, A. Paciaroni, V. Venuti, G. C. Fadda, L. Melone, C. Punta, V. Crupi, D. Majolino, and A. Mele. SANS investigation of water adsorption in tunable cyclodextrin-based polymeric hydrogels. *Physical chemistry chemical physics*, **19**(8):6022–6029, 2017.
- [25] S. I. Yun, K.-C. Lai, R. M. Briber, S. J. Teertstra, M. Gauthier, and B. J. Bauer. Conformation of arborescent polymers in solution by small-angle neutron scattering: segment density and core-shell morphology. *Macromolecules*, **41**(1):175–183, 2008.

- [26] L. E. Millon, M.-P. Nieh, J. L. Hutter, and W. Wan. SANS characterization of an anisotropic poly(vinyl alcohol) hydrogel with vascular applications. *Macromolecules*, **40**(10):3655–3662, 2007.
- [27] S. K. Agrawal, N. Sanabria-DeLong, P. R. Jemian, G. N. Tew, and S. R. Bhatia. Micro- to nanoscale structure of biocompatible PLA-PEO-PLA hydrogels. *Langmuir*, **23**(9):5039–5044, 2007.
- [28] C. J. Vörösmarty, P. B. McIntyre, M. O. Gessner, D. Dudgeon, A. Prusevich, P. Green, S. Glidden, S. E. Bunn, C. A. Sullivan, C. R. Liermann, and P. M. Davies. Global threats to human water security and river biodiversity. *Nature*, **467**(7315):555–561, 2010.
- [29] H. M. Irving, M. G. Miles, and L. D. Pettit. A study of some problems in determining the stoichiometric proton dissociation constants of complexes by potentiometric titrations using a glass electrode. *Analytica chimica acta*, **38**:475–488, 1967.
- [30] C. N. Nupearachchi, K. Mahatantila, and M. Vithanage. Application of graphene for decontamination of water; implications for sorptive removal. *Groundwater for sustainable development*, **5**:206–215, 2017.
- [31] S. Tanabe and T. B. Minh. Dioxins and organohalogen contaminants in the asia-pacific region. *Ecotoxicology*, **19**(3):463–478, 2010.
- [32] O. C. Eneh. Managing Nigeria’s environment: the unresolved issues. *Journal of environmental science and technology*, **4**(3):250–263, 2011.
- [33] D. Q. Zhang, S. Jinadasa, R. M. Gersberg, Y. Liu, W. J. Ng, and S. K. Tan. Application of constructed wetlands for wastewater treatment in developing countries – a review of recent developments (2000–2013). *Journal of environmental management*, **141**:116–131, 2014.
- [34] M. A. Barakat. New trends in removing heavy metals from industrial wastewater. *Arabian journal of chemistry*, **4**(4):361–377, 2011.
- [35] F. Fu and Q. Wang. Removal of heavy metal ions from wastewaters: a review. *Journal of environmental management*, **92**(3):407–418, 2011.

- [36] Y. Zheng, X. Li, and P. K. Dutta. Exploitation of unique properties of zeolites in the development of gas sensors. *Sensors*, **12**(4):5170–5194, 2012.
- [37] A. Carvalho, M. Marinova, N. Batalha, N. R. Marcilio, A. Y. Khodakov, and V. V. Ordonsky. Design of nanocomposites with cobalt encapsulated in the zeolite micropores for selective synthesis of isoparaffins in Fischer–Tropsch reaction. *Catalysis science & technology*, **7**(21):5019–5027, 2017.
- [38] G. Zhao, X. Wu, X. Tan, and X. Wang. Sorption of heavy metal ions from aqueous solutions: a review. *The open colloid science journal*, **4**(1):19–31, 2011.
- [39] M. R. Jakobsen, J. Fritt-Rasmussen, S. Nielsen, and L. M. Ottosen. Electro-dialytic removal of cadmium from wastewater sludge. *Journal of hazardous materials*, **106**(2-3):127–132, 2004.
- [40] J. M. Salman. Optimization of preparation conditions for activated carbon from palm oil fronds using response surface methodology on removal of pesticides from aqueous solution. *Arabian journal of chemistry*, **7**(1):101–108, 2014.
- [41] J. M. Dias, M. C. M. Alvim-Ferraz, M. F. Almeida, J. Rivera-Utrilla, and M. Sánchez-Polo. Waste materials for activated carbon preparation and its use in aqueous-phase treatment: a review. *Journal of environmental management*, **85**(4):833–846, 2007.
- [42] M. J. Ayotamuno, R. Kogbara, S. O. T. Ogaji, and S. D. Probert. Petroleum contaminated ground-water: remediation using activated carbon. *Applied energy*, **83**(11):1258–1264, 2006.
- [43] K. D. Henning and J. Degel. Activated carbon for solvent recovery. *Meeting of the european rotogravure association engineers group*, **1**:20–21, 1990.
- [44] V. Hooda. Phytoremediation of toxic metals from soil and waste water. *Journal of environmental biology*, **28**(2):367–376, 2007.
- [45] I. Raskin, R. D. Smith, and D. E. Salt. Phytoremediation of metals: using plants to remove pollutants from the environment. *Current opinion in biotechnology*, **8**(2):221–226, 1997.

- [46] A. Puri. Green materials for sustainable remediation of metals in water. *Green materials for sustainable water remediation and treatment*, **23**:11–26, 2013.
- [47] O. Akpor and M. Muchie. Remediation of heavy metals in drinking water and wastewater treatment systems: processes and applications. *International journal of physical sciences*, **5**(12):1807–1817, 2010.
- [48] T. Mahmood. Phytoextraction of heavy metals: the process and scope for remediation of contaminated soils. *Plant soil and environment*, **29**(2):91–109, 2010.
- [49] M. D. Vidali. Bioremediation: an overview. *Pure and applied chemistry*, **73**(7):1163–1172, 2001.
- [50] K. Chojnacka. Biosorption and bioaccumulation—the prospects for practical applications. *Environment international*, **36**(3):299–307, 2010.
- [51] K. M. Paknikar, A. V. Pethkar, and P. Puranik. Bioremediation of metalliferous wastes and products using inactivated microbial biomass. *Indian journal of biotechnology*, **2**:426–443, 2003.
- [52] J. Wang and C. Chen. Biosorbents for heavy metals removal and their future. *Biotechnology advances*, **27**(2):195–226, 2009.
- [53] J. C. G. Rincon, F. González, M. A. Ballester, M. L. Blázquez, and J. A. Munoz. Biosorption of heavy metals by chemically-activated alga *Fucus vesiculosus*. *Journal of chemical technology & biotechnology: international research in process, environmental & clean technology*, **80**(12):1403–1407, 2005.
- [54] L. Brinza, M. J. Dring, and M. Gavrilescu. Marine micro and macro algal species as biosorbents for heavy metals. *Environmental engineering & management journal (EEMJ)*, **6**(3):237–251, 2007.
- [55] E. R. Birnbaum, K. C. Rau, and N. N. Sauer. Selective anion binding from water using soluble polymers. *Separation science and technology*, **38**(2):389–404, 2003.
- [56] R. Q. Long and R. T. Yang. Carbon nanotubes as superior sorbent for dioxin removal. *Journal of the American chemical society*, **123**(9):2058–2059, 2001.

- [57] Y.-H. Li, S. Wang, A. Cao, D. Zhao, X. Zhang, C. Xu, Z. Luan, D. Ruan, J. Liang, D. Wu, et al. Adsorption of fluoride from water by amorphous alumina supported on carbon nanotubes. *Chemical physics letters*, **350**(5-6):412–416, 2001.
- [58] C. Park, E. S. Engel, A. Crowe, T. R. Gilbert, and N. M. Rodriguez. Use of carbon nanofibers in the removal of organic solvents from water. *Langmuir*, **16**(21):8050–8056, 2000.
- [59] M. S. Diallo, S. Christie, P. Swaminathan, J. H. Johnson, and W. A. Goddard. Dendrimer enhanced ultrafiltration. 1. Recovery of Cu(II) from aqueous solutions using PAMAM dendrimers with ethylene diamine core and terminal NH₂ groups. *Environmental science & technology*, **39**(5):1366–1377, 2005.
- [60] M. Diallo, J. Thonnon, M. Traore-Lamizana, and D. Fontenille. Vectors of chikungunya virus in senegal: current data and transmission cycles. *The American journal of tropical medicine and hygiene*, **60**(2):281–286, 1999.
- [61] K. Zodrow, L. Brunet, S. Mahendra, D. Li, A. Zhang, Q. Li, and P. J. J. Alvarez. Polysulfone ultrafiltration membranes impregnated with silver nanoparticles show improved biofouling resistance and virus removal. *Water research*, **43**(3):715–723, 2009.
- [62] H. Strathmann. Membrane separation processes: current relevance and future opportunities. *AIChE journal*, **47**(5):1077–1087, 2001.
- [63] Y. Nishiyama. Structure and properties of the cellulose microfibril. *Journal of wood science*, **55**(4):241–249, 2009.
- [64] O. A. Hisseine, A. F. Omran, and A. Tagnit-Hamou. Influence of cellulose filaments on cement paste and concrete. *Journal of materials in civil engineering*, **30**(6):04018109–04018122, 2018.
- [65] T. C. Davidson, R. H. Newman, and M. J. Ryan. Variations in the fibre repeat between samples of cellulose I from different sources. *Carbohydrate research*, **339**(18):2889–2893, 2004.

- [66] Y. Nishiyama, J. Sugiyama, H. Chanzy, and P. Langan. Crystal structure and hydrogen bonding system in cellulose I α from synchrotron x-ray and neutron fiber diffraction. *Journal of the American chemical society*, **125**(47):14300–14306, 2003.
- [67] D. Hayakawa, Y. Nishiyama, K. Mazeau, and K. Ueda. Evaluation of hydrogen bond networks in cellulose I β and II crystals using density functional theory and Car–Parrinello molecular dynamics. *Carbohydrate research*, **449**:103–113, 2017.
- [68] J. Sugiyama, R. Vuong, and H. Chanzy. Electron diffraction study on the two crystalline phases occurring in native cellulose from an algal cell wall. *Macromolecules*, **24**(14):4168–4175, 1991.
- [69] R. J. Viëtor, K. Mazeau, M. Lakin, and S. Pérez. A priori crystal structure prediction of native celluloses. *Biopolymers: original research on biomolecules*, **54**(5):342–354, 2000.
- [70] M. Wada, T. Okano, J. Sugiyama, and F. Horii. Characterization of tension and normally lignified wood cellulose in *Populus maximowiczii*. *Cellulose*, **2**(4):223–233, 1995.
- [71] A. Hirai, F. Horii, and R. Kitamaru. Transformation of native cellulose crystals from cellulose I β to I α through solid-state chemical reactions. *Macromolecules*, **20**(6):1440–1442, 1987.
- [72] D. Liu, X. Chen, Y. Yue, M. Chen, and Q. Wu. Structure and rheology of nanocrystalline cellulose. *Carbohydrate polymers*, **84**(1):316–322, 2011.
- [73] H. O’neill, S. V. Pingali, L. Petridis, J. He, E. Mamontov, L. Hong, V. Urban, B. Evans, P. Langan, J. C Smith, et al. Dynamics of water bound to crystalline cellulose. *Scientific reports*, **7**(1):11840–11852, 2017.
- [74] D. Klemm, F. Kramer, S. Moritz, T. Lindström, M. Ankerfors, D. Gray, and A. Dorris. Nanocelluloses: a new family of nature-based materials. *Angewandte chemie international edition*, **50**(24):5438–5466, 2011.

- [75] Y. Lu and S. Ozcan. Green nanomaterials: on track for a sustainable future. *Nano today*, **10**(4):417–420, 2015.
- [76] T. Abitbol, A. Rivkin, Y. Cao, Y. Nevo, E. Abraham, T. Ben-Shalom, S. Lapidot, and O. Shoseyov. Nanocellulose, a tiny fiber with huge applications. *Current opinion in biotechnology*, **39**:76–88, 2016.
- [77] W. Wu, N. G. Tassi, H. Zhu, Z. Fang, and L. Hu. Nanocellulose-based translucent diffuser for optoelectronic device applications with dramatic improvement of light coupling. *ACS applied materials & interfaces*, **7**(48):26860–26864, 2015.
- [78] F. Hoeng, A. Denneulin, and J. Bras. Use of nanocellulose in printed electronics: a review. *Nanoscale*, **8**(27):13131–13154, 2016.
- [79] M. Kaushik and A. Moores. nanocelluloses as versatile supports for metal nanoparticles and their applications in catalysis. *Green chemistry*, **18**(3):622–637, 2016.
- [80] T. G. M. van de Ven and A. Sheikhi. Hairy cellulose nanocrystalloids: a novel class of nanocellulose. *Nanoscale*, **8**(33):15101–15114, 2016.
- [81] S. Coseri, G. Nistor, L. Fras, S. Strnad, V. Harabagiu, and B. C. Simionescu. Mild and selective oxidation of cellulose fibers in the presence of n-hydroxyphthalimide. *Biomacromolecules*, **10**(8):2294–2299, 2009.
- [82] S. Coseri, G. Biliuta, B. C. Simionescu, K. Stana-Kleinschek, V. Ribitsch, and V. Harabagiu. Oxidized cellulose—survey of the most recent achievements. *Carbohydrate polymers*, **93**(1):207–215, 2013.
- [83] A. Isogai, T. Saito, and H. Fukuzumi. TEMPO-oxidized cellulose nanofibers. *nanoscale*, **3**(1):71–85, 2011.
- [84] G. Pierre, C. Punta, C. Delattre, L. Melone, P. Dubessay, A. Fiorati, N. Pastori, Y. M. Galante, and P. Michaud. TEMPO-mediated oxidation of polysaccharides: an ongoing story. *Carbohydrate polymers*, **165**:71–85, 2017.

- [85] L. Melone, S. Bonafede, D. Tushi, C. Punta, and M. Cametti. Dip in colorimetric fluoride sensing by a chemically engineered polymeric cellulose/bPEI conjugate in the solid state. *Rsc advances*, **5**(101):83197–83205, 2015.
- [86] T. Kanaya, N. Takahashi, H. Takeshita, M. Ohkura, K. Nishida, and K. Kaji. Structure and dynamics of poly(vinyl alcohol) gels in mixtures of dimethyl sulfoxide and water. *Polymer journal*, **44**(1):83–94, 2012.
- [87] L. Rosta and R. Baranyai. Budapest research reactor–20 years of international user operation. *Neutron news*, **22**(3):31–36, 2011.
- [88] L. Almásy, A. Len, M. Markó, and E. Rétfalvi. Wavelength calibration in conventional SANS setup with a mechanical velocity selector. *Zeitschrift für kristallographie*, **23**:211–216, 2006.
- [89] U. Keiderling. The new ‘berSANS-PC’ software for reduction and treatment of small angle neutron scattering data. *Applied physics A*, **74**(1):1455–1457, 2002.
- [90] Z. S. Nickolov, Ö. Ozcan, and J. D. Miller. FTIR analysis of water structure and its significance in the flotation of sodium carbonate and sodium bicarbonate salts. *Colloids and surfaces A: physicochemical and engineering aspects*, **224**(1-3):231–239, 2003.
- [91] J. Ryczkowski. IR spectroscopy in catalysis. *Catalysis today*, **68**(4):263–381, 2001.
- [92] A. R. Hind, S. K. Bhargava, and A. McKinnon. At the solid/liquid interface: FTIR/ATR—the tool of choice. *Advances in colloid and interface science*, **93**(1-3):91–114, 2001.
- [93] L.-M. Döppers, C. Sammon, C. Breen, and J. Yarwood. FTIR–ATR studies of the sorption and diffusion of acetone/water mixtures in poly(vinyl alcohol). *Polymer*, **47**(8):2714–2722, 2006.
- [94] R. A. Hule, R. P. Nagarkar, A. Altunbas, H. R. Ramay, M. C. Branco, J. P. Schneider, and D. J. Pochan. Correlations between structure, material properties and bioproperties in self-assembled β -hairpin peptide hydrogels. *Faraday discussions*, **139**:251–264, 2008.

- [95] R. A. Hule, R. P. Nagarkar, B. Hammouda, J. P. Schneider, and D. J. Pochan. Dependence of self-assembled peptide hydrogel network structure on local fibril nanostructure. *Macromolecules*, **42**(18):7137–7145, 2009.
- [96] F. Horkay, P. J. Basser, A.-M. Hecht, and E. Geissler. Structural investigations of a neutralized polyelectrolyte gel and an associating neutral hydrogel. *Polymer*, **46**(12):4242–4247, 2005.
- [97] E. M. Saffer, M. A. Lackey, D. M. Griffin, S. Kishore, G. N. Tew, and S. R. Bhatia. SANS study of highly resilient poly(ethylene glycol) hydrogels. *Soft matter*, **10**(12):1905–1916, 2014.
- [98] B. Hammouda, F. Horkay, and M. L. Becker. Clustering and solvation in poly(acrylic acid) polyelectrolyte solutions. *Macromolecules*, **38**(5):2019–2021, 2005.
- [99] B. Hammouda. Solvation characteristics of a model water-soluble polymer. *Journal of polymer science part B: polymer physics*, **44**(22):3195–3199, 2006.
- [100] B. Hammouda, D. L. Ho, and S. Kline. Insight into clustering in poly(ethylene oxide) solutions. *Macromolecules*, **37**(18):6932–6937, 2004.
- [101] D. R. Chang, S. Harden, and N. Loverro. Protonation of polyethylenimine. *Journal of macromolecular science: part A - chemistry*, **23**(6):801–804, 1986.
- [102] J. D. Ziebarth and Y. Wang. Understanding the protonation behavior of linear polyethylenimine in solutions through Monte Carlo simulations. *Biomacromolecules*, **11**(1):29–38, 2009.
- [103] C. K. Choudhury and S. Roy. Structural and dynamical properties of polyethylenimine in explicit water at different protonation states: a molecular dynamics study. *Soft matter*, **9**(7):2269–2281, 2013.
- [104] J.-P. Behr. The proton sponge: a trick to enter cells the viruses did not exploit. *CHIMIA international journal for chemistry*, **51**(1-2):34–36, 1997.
- [105] G. Beaucage. Small-angle scattering from polymeric mass fractals of arbitrary mass-fractal dimension. *Journal of applied crystallography*, **29**(2):134–146, 1996.

- [106] R. Shi, Z. Zhang, Q. Liu, Y. Han, L. Zhang, D. Chen, and W. Tian. Characterization of citric acid/glycerol co-plasticized thermoplastic starch prepared by melt blending. *Carbohydrate polymers*, **69**(4):748–755, 2007.
- [107] E. J. Blanchard, R. M. Reinhardt, E. E. Graves, and B. A. K. Andrews. Dyeable cross-linked cellulose from low formaldehyde and non-formaldehyde finishing systems. *Industrial & engineering chemistry research*, **33**(4):1030–1034, 1994.
- [108] V. Coma, I. Sebti, P. Pardon, F. H. Pichavant, and A. M. Deschamps. Film properties from crosslinking of cellulosic derivatives with a polyfunctional carboxylic acid. *Carbohydrate polymers*, **51**(3):265–271, 2003.
- [109] H. Möller, S. Grelier, P. Pardon, and V. Coma. Antimicrobial and physicochemical properties of chitosan-HPMC-based films. *Journal of agricultural and food chemistry*, **52**(21):6585–6591, 2004.
- [110] F. Xu, J. Yu, T. Tesso, F. Dowell, and D. Wang. Qualitative and quantitative analysis of lignocellulosic biomass using infrared techniques: a mini-review. *Applied energy*, **104**:801–809, 2013.
- [111] K. Fackler, J. S. Stevanic, T. Ters, B. Hinterstoisser, M. Schwanninger, and L. Salmén. FT-IR imaging microscopy to localise and characterise simultaneous and selective white-rot decay within spruce wood cells. *Holzforschung*, **65**(3):411–420, 2011.
- [112] V. Hospodarova, E. Singovszka, and N. Stevulova. Characterization of cellulosic fibers by FTIR spectroscopy for their further implementation to building materials. *American journal of analytical chemistry*, **9**(6):303–310, 2018.
- [113] J. R. Scherer, M. K. Go, and S. Kint. Raman spectra and structure of water from -10 to 90.deg. *The journal of physical chemistry*, **78**(13):1304–1313, 1974.
- [114] T. T. Wall and D. F. Hornig. Raman intensities of HDO and structure in liquid water. *The journal of chemical physics*, **43**(6):2079–2087, 1965.
- [115] W. F. Murphy and H. J. Bernstein. Raman spectra and an assignment of the vibrational stretching region of water. *The journal of physical chemistry*, **76**(8):1147–1152, 1972.

- [116] V. Crupi, D. Majolino, A. Mele, B. Rossi, F. Trotta, and V. Venuti. Modelling the interplay between covalent and physical interactions in cyclodextrin-based hydrogel: effect of water confinement. *Soft matter*, **9**(28):6457–6464, 2013.
- [117] F. Castiglione, V. Crupi, D. Majolino, A. Mele, B. Rossi, F. Trotta, and V. Venuti. Inside new materials: an experimental numerical approach for the structural elucidation of nanoporous cross-linked polymers. *The journal of physical chemistry B*, **116**(43):13133–13140, 2012.
- [118] F. Castiglione, V. Crupi, D. Majolino, A. Mele, B. Rossi, F. Trotta, and V. Venuti. Effect of cross-linking properties on the vibrational dynamics of cyclodextrins-based polymers: an experimental–numerical study. *The journal of physical chemistry B*, **116**(27):7952–7958, 2012.
- [119] V. Crupi, A. Fontana, M. Giarola, D. Majolino, G. Mariotto, A. Mele, L. Melone, C. Punta, B. Rossi, F. Trotta, et al. Connection between the vibrational dynamics and the cross-linking properties in cyclodextrins-based polymers. *Journal of Raman spectroscopy*, **44**(10):1457–1462, 2013.
- [120] J.-B. Brubach, A. Mermet, A. Filabozzi, A. Gerschel, and P. Roy. Signatures of the hydrogen bonding in the infrared bands of water. *The journal of chemical physics*, **122**(18):184509–184515, 2005.
- [121] F. Mallamace, M. Broccio, C. Corsaro, A. Faraone, D. Majolino, V. Venuti, L. Liu, C.-Y. Mou, and S.-H. Chen. Evidence of the existence of the low-density liquid phase in supercooled, confined water. *Proceedings of the national academy of sciences*, **104**(2):424–428, 2007.
- [122] A. Millo, Y. Raichlin, and A. Katzir. Mid-infrared fiber-optic attenuated total reflection spectroscopy of the solid–liquid phase transition of water. *Applied spectroscopy*, **59**(4):460–466, 2005.
- [123] V. Crupi, D. Majolino, P. Migliardo, V. Venuti, and M. C. Bellissent-Funel. Structure and dynamics of water confined in a nanoporous sol-gel silica glass: a neutron scattering study. *Molecular physics*, **101**(22):3323–3333, 2003.
- [124] R. Bergman and J. Swenson. Dynamics of supercooled water in confined geometry. *Nature*, **403**(6767):283–286, 2000.

- [125] V. Crupi, F. Longo, D. Majolino, and V. Venuti. T dependence of vibrational dynamics of water in ion-exchanged zeolites A: a detailed Fourier transform infrared attenuated total reflection study. *The journal of chemical physics*, **123**(15):154702–154712, 2005.
- [126] G. E. Walrafen, M. S. Hokmabadi, and W.-H. Yang. Raman isosbestic points from liquid water. *The journal of chemical physics*, **85**(12):6964–6969, 1986.
- [127] G. D’Arrigo, G. Maisano, F. Mallamace, P. Migliardo, and F. Wanderlingh. Raman scattering and structure of normal and supercooled water. *The journal of chemical physics*, **75**(9):4264–4270, 1981.
- [128] V. Crupi, A. Fontana, D. Majolino, A. Mele, L. Melone, C. Punta, B. Rossi, F. Rossi, F. Trotta, and V. Venuti. Hydrogen-bond dynamics of water confined in cyclodextrin nanosponges hydrogel. *Journal of inclusion phenomena and macrocyclic chemistry*, **80**(1-2):69–75, 2014.
- [129] F. Castiglione, V. Crupi, D. Majolino, A. Mele, L. Melone, W. Panzeri, C. Punta, B. Rossi, F. Trotta, and V. Venuti. Gel-sol evolution of cyclodextrin-based nanosponges: role of the macrocycle size. *Journal of inclusion phenomena and macrocyclic chemistry*, **80**(1-2):77–83, 2014.
- [130] V. Crupi, D. Majolino, A. Mele, L. Melone, C. Punta, B. Rossi, F. Toraldo, F. Trotta, and V. Venuti. Direct evidence of gel–sol transition in cyclodextrin-based hydrogels as revealed by FTIR-ATR spectroscopy. *Soft matter*, **10**(13):2320–2326, 2014.
- [131] F. Castiglione, V. Crupi, D. Majolino, A. Mele, B. Rossi, F. Trotta, and V. Venuti. Vibrational spectroscopy investigation of swelling phenomena in cyclodextrin nanosponges. *Journal of Raman spectroscopy*, **44**(10):1463–1469, 2013.
- [132] G. Bellavia, L. Paccou, S. Achir, Y. Guinet, J. Siepmann, and A. Hédoux. Analysis of bulk and hydration water during thermal lysozyme denaturation using Raman scattering. *Food biophysics*, **8**(3):170–176, 2013.

- [133] A. Hédoux, Y. Guinet, and L. Paccou. Analysis of the mechanism of lysozyme pressure denaturation from Raman spectroscopy investigations, and comparison with thermal denaturation. *The journal of physical chemistry B*, **115**(20):6740–6748, 2011.
- [134] G. E. Walrafen. Raman spectral studies of the effects of temperature on water structure. *The journal of chemical physics*, **47**(1):114–126, 1967.
- [135] N. Goldman and R. J. Saykally. Elucidating the role of many-body forces in liquid water. I. Simulations of water clusters on the VRT (ASP-W) potential surfaces. *The journal of chemical physics*, **120**(10):4777–4789, 2004.
- [136] P. A. Giguère. The bifurcated hydrogen-bond model of water and amorphous ice. *The journal of chemical physics*, **87**(8):4835–4839, 1987.
- [137] M. Freda, A. Piluso, A. Santucci, and P. Sassi. Transmittance Fourier transform infrared spectra of liquid water in the whole mid-infrared region: temperature dependence and structural analysis. *Applied spectroscopy*, **59**(9):1155–1159, 2005.
- [138] D. A. Schmidt and K. Miki. Structural correlations in liquid water: a new interpretation of IR spectroscopy. *The journal of physical chemistry A*, **111**(40):10119–10122, 2007.